INTERFACIAL HYDRODYNAMICS OF JANUS PARTICLES: TILTING, TUMBLING, AND ORDER

by

HOSSEIN REZVANTALAB

A dissertation submitted to the

Graduate School-New Brunswick

Rutgers, The State University of New Jersey

In partial fulfillment of the requirements

For the degree of

Doctor of Philosophy

Graduate Program in Mechanical and Aerospace Engineering

Written under the direction of

Shahab Shojaei-Zadeh

And approved by

_____

_____

_____

_____

New Brunswick, New Jersey

October, 2015

ABSTRACT OF THE DISSERTATION

Interfacial Hydrodynamics of Janus Particles:

Tilting, Tumbling, and Order

By HOSSEIN REZVANTALAB

Dissertation Director:

Shahab Shojaei-Zadeh

Janus particles are a class of colloids characterized by two regions of distinct surface properties. Those with hydrophilic–hydrophobic regions tend to strongly adsorb to liquid–fluid interfaces and may exhibit unique equilibrium and dynamic behavior not observed in homogeneous colloids. When in bulk phase (*i.e.* suspension), Janus particles are shown to self–assemble into strings and lattices. Interfacial behavior of such particles however is less explored, especially those related to transport and dynamics under the influence of external fields. Such knowledge is crucial not only to predict the response of systems with particles at interfaces (*e.g.* particle–stabilized emulsions and foams) to external fields, but also to design and enable novel materials and applications.

In this thesis, we first provide a quasi–static analysis on the equilibrium orientation of single and capillary–induced interactions between particle pairs. For Janus spheres, we show the existence of dipolar capillary forces, and quantify them in terms of

particle size and amphiphilicity. Moreover, breaking the symmetry in distribution of the two Janus regions can enhance particle surface activity. In Janus ellipsoids, shape anisotropy results in capillary hexapoles, which govern their preferred side–by–side alignment at an interface.

In the second part, we investigate hydrodynamics of Janus particles at fluid interfaces by first exploring their interfacial thermal diffusion. We demonstrate that the diffusivity is not only a function of particle size, but also depends on amphiphilicity: thermal diffusion reduces as amphiphilicity increases. We then explore dynamic response of Janus particles to a symmetric shear at the interface. For isolated particles, depending on shape, amphiphilicity, and the shear rate, two unique rotational dynamics are observed: tilting and tumbling. For a cluster of randomly distributed Janus particles, we show that the interfacial shear is capable of ordering them into chains normal to shear direction. The order parameter and separation between the chains depends on the surface coverage and strength of capillary dipoles. We obtain an optimum range of surface coverage in which ordered structures are obtained. An interesting feature of this method is that the resulting ordered structure is preserved after the field is removed.

Acknowledgements

First and foremost, I would like to thank my advisor, Dr. Shahab Shojaei-Zadeh for allowing me to conduct research under his watchful eye. He put significant effort in improving my attitude towards research and guided me to a path full of novel ideas and exciting problems that I enjoyed exploring over four years of my PhD studies. I would also like to thank my thesis committee members, Dr. Morris, Dr. Cuitino and Dr. Shan for the time they spent reviewing my thesis.

Dr. German Drazer was also of great help through the course of my research particularly on the molecular simulations. He always delivered constructive remarks which made me think more deeply and critically about the physical aspects of different problems. I am also grateful to Dr. Kevin Connington and Dr. Ken Brakke for their help analyzing and commenting on my numerical codes. I also want to thank my lab-mates for their companionship and insightful discussions: Michael Fechtmann, Matt Ambrush, Jeffrey Infante, Stephen Rowe, and Robert Weir. The lab was always lively with their presence and without them, my breadth of knowledge would be considerably less.

My parents supported me by all possible means through my entire PhD career at Rutgers, and I am forever indebted to them for their kindness. Lastly, I would like to express my heartfelt gratitude to my wonderful wife, Hoda, for all her patience and devotion to my success during these difficult years. If it wasn't because of her presence, I would have never been able to take this long journey and accomplish this degree.

Hossein Rezvantalab

Rutgers, The State University of New Jersey

August 5, 2015

Table of Contents

List of Illustrations

Chapter 1

Introduction and Motivation

1.1 Introduction

1.1.1 Anisotropic Particles with Multicompartment Architecture

Nature often serves as a source of inspiration for the technological development of materials of all types. Natural materials are characterized by hierarchical structures at scales ranging from nanometer to millimeters, comprising a variety of properties occurring at such structural levels. As a consequence, a broad range of incentives for designing elegant micro- and nanoparticles with multiple functions can be found [2, 3].

In this context, advanced research has led to a sophisticated set of tools to control the size, shape, polydispersity and surface chemistry of various colloids. Consequently, novel approaches have been developed for tailoring particles for specific tasks. While particles

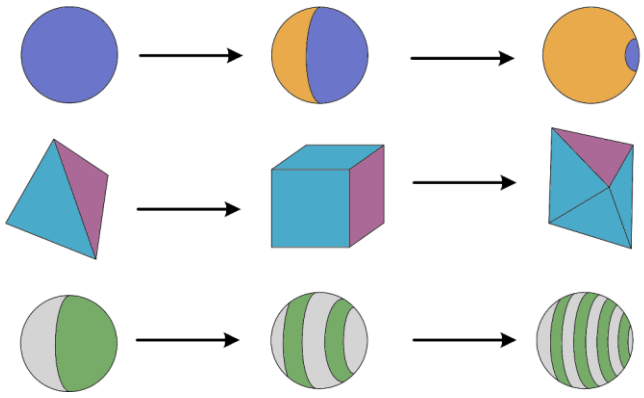

Figure 1.1 Examples of different types of anisotropy dimensions
From top: surface coverage, faceting, and branching [1].

with isotropic volume/surface properties are ideal systems for several scientific/technological applications, a more advanced design is required for some complex processes. Particles with an anisotropic structure are thus even more attractive, since not only their shape, but also their functionality can be controlled. With reference to a number of excellent reviews covering all types of anisotropic particles [4-10], a highly sophisticated classification has been provided [3, 11]. Examples of some anisotropy dimensions are shown in Figure 1.1.

The past few years have witnessed a revolution in materials science, especially in the preparation and design of nano- or micron-sized particles with patterned anisotropy such as multicompartment, patchy, and Janus particles. These are intriguing building blocks of precisely defined size, shape and functionality and offer a versatile platform for the creation of novel materials with specific and predictable properties due to their non-centrosymmetric features.

1.1.2 Janus Particles

The concept of "Janus" particles was first introduced by De Gennes in his 1991 Nobel lecture [12]. He pointed out that these objects possessing two sides of different wettability have the unique advantage of densely self-assembling at liquid-liquid interfaces and allow material transport through the gaps between them. Consequently, they have become a new prevailing class of colloidal structures among micron- or nanosized particles. The terminology is based on the special architectural feature of having two sides or at least two surfaces with different chemistry or polarity.

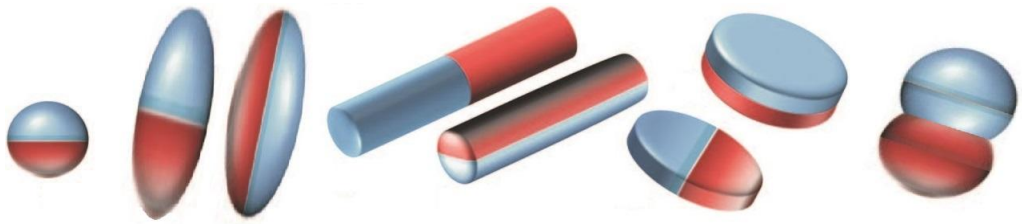

Figure 1.2 Various shapes of Janus particles composed of two sides of functionally-different elements.

The chemical asymmetry in Janus systems has led to the discovery of new properties as well as unusual aggregation behavior into superstructures, making this research area an interdisciplinary field with researchers from different backgrounds contributing together [13]. In the beginning, the synthetic access to Janus particles was limited to extremely small amounts, thus also limiting further studies. However, new approaches have enabled high-throughput fabrication of this family of colloids. Various groups have reported the successful preparation of different types of Janus particles with different composition, chemistry, polarity, and functionality. Recent synthesis methods have enabled fabrication of Janus particles in different shapes including spheres, ellipsoids, cylinders, discs, and dumbbells as shown in Figure 1.2 [8, 13].

1.1.3 Properties and Applications

The two sides of Janus particles may differ in wetting, magnetic, catalytic, optical, or electrical properties. As a consequence, they offer a versatile platform for applications ranging from pharmaceutical to optics and catalysis. Janus particles have already demonstrated the potential to be used as drug carriers, emulsion stabilizers, switchable displays, and optical probes [14-19].

For example, the biocompatibility of Janus particles obtained by co-jetting of two liquid solutions containing immiscible polymers has been tested [14] for their use in biological applications *e.g.* in drug/gene delivery and targeted destruction of cancer cells [15-17]. Another example is a tunable, high-reflectivity optofluidic device fabricated based on self-assembly of Janus tiles on the surface of an oil droplet [18]. Moreover, water repellent nanofibers have been prepared by coating polyethylene terephtalate-based textile fibers with amphiphilic Janus nanoparticles [18]. This type of Janus particles has also been exploited in chemical reactions, *e.g.* in enhancing the phase-selectivity of biofuel refining processes [19].

The first example of controlled self-assembly of Janus particles into highly ordered superstructures was observed by Müller et al. using Janus spheres [20, 21], cylinders [22], as well as discs [23, 24]. Following their lead, the assembly of Janus particles both in bulk fluids and at interfaces have been reported by other authors as well [25-28].

1.1.4 Janus Particles at Liquid Interfaces

The most relevant properties of Janus particles are their surface activity and their capability to self-assemble into complex structures. The stabilization of emulsions and dispersions is very important for several processes *e.g.* in preparation of food and personal care products. In contrast to particles with uniform wettability, the surface of amphiphilic Janus particles has two parts exhibiting different wettability, thus making them suitable candidates to adsorb and assemble at interfaces (Figure 1.3). Significant research has been carried out to evaluate the high adsorption energy of Janus particles at fluid interfaces. Binks and Fletcher's first calculations of interfacial behavior of biphasic

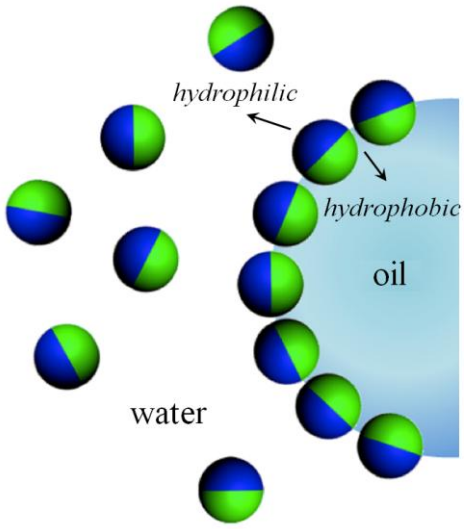

Figure 1.3 Schematic of Janus particles used for stabilization of an oil-water interface.

Janus spheres revealed an up to three-fold stronger adsorption compared to particles of uniform wettability [29]. Since then, several studies have investigated the interfacial activity of Janus particles of different geometry. Theoretical calculations on the influence of disc-shaped Janus beads on the oil/water interfacial tension revealed that their adsorption energy is several orders of magnitude higher than that of common surfactants [30, 31].

Glaser et al. reported the first experiments on the interfacial activity of Janus nanoparticles using gold/iron oxide particles at hexane/water interface [32]. Using pendant drop tensiometry, they showed that bimetallic Janus particles lead to a more significant reduction of the interfacial tension compared to uniform metallic nanoparticles of similar size (iron oxide or gold). Other groups have also reported experiments on the enhanced stabilization of liquid-liquid interfaces by Janus particles [33, 34]. In terms of real prototype applications, an improved performance of Janus particles has been demonstrated with their use for nanostructuring of polymer blends [35] and emulsion

polymerization [36] as compared to their homogeneous counterparts. Additional studies suggest that the size, shape, and surface properties of Janus particles play a significant role on their surface activity, equilibrium orientation, and packing density [37-39].

1.2 Motivation and Significance

As discussed in the previous section, considerable attention has been recently paid to the behavior of amphiphilic Janus particles at liquid interfaces. The anisotropy in wetting properties of such particles can be used to enhance the stability of Pickering systems: emulsions/foams stabilized by particles adsorbed at liquid–fluid interfaces. The difference in wettability of the two surfaces can also result in formation of complex self-assembled structures due to the anisotropy of interactions [40-42].

Most of theoretical work so far has been focused on understanding the stability and the equilibrium orientation of spherical Janus particles at fluid interfaces. On the other hand, their interfacial dynamics and the influence of particle shape on their interactions are still unclear despite their importance for effective use of Janus particles as stabilizers [43]. As the adsorption of such particles to liquid interfaces typically involves hydrodynamic flows, it is also of interest to evaluate the change in equilibrium orientation and consequently the inter-particle interactions in presence of external fields, which can yield a variety of structures for development of novel functional materials.

1.3 Current Research

Here, we explain the outline of this thesis concerning the interfacial dynamics and transport of Janus particles. To get a general idea of how such particles orient and interact

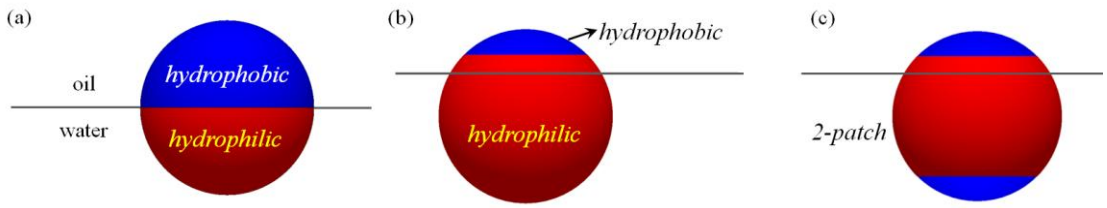

Figure 1.4 Schematic representation of Janus spheres with (a) symmetric surface coverage, (b) asymmetric coverage, (c) double-patch design, at an interface.

at a liquid interface, we start with a quasi-static analysis on the equilibrium orientation and capillary-induced forces between Janus particles of different geometry and surface patterning. For spherical particles, we first look at those with equal coverage of hydrophilic/hydrophobic regions. In case of perfectly smooth Janus boundary, it is known that the equilibrium orientation is where each side is completely in contact with its favored phase [44-46], as shown in Figure 1.4(a). It is possible, however, that not all the particles approach the interface according to this orientation as suggested by experiments [1, 38]. We will numerically calculate the interface shape around Janus spheres with such tilted orientations and evaluate the capillary interactions that arise due to overlapping of distortions caused by neighboring particles. Different interaction regimes between these Janus spheres will be investigated in detail.

Noting that an asymmetric distribution of surface regions may enhance the interfacial activity depending on the wettabilities, we then consider Janus spheres where the two regions possess different surface area (see Figure 1.4(b)). We find the equilibrium orientation for these particles and estimate their surface activity by calculating their detachment energy. In order to see if more intricate patterns and branching surfaces into several parts can be beneficial in further improving the interfacial activity of such particles, we also consider particles containing two symmetric patches on a spherical

base, as in Figure 1.4(c). Such geometry has been used for studying particle self-assembly in bulk media due to anisotropic interactions and in modeling protein molecules in drug delivery and food industry [47-49]. We will find the equilibrium orientation of these particles, evaluate possible capillary-induced interactions, and the conditions at which this design can yield a higher interfacial activity (*i.e.* a higher energy required for detaching the particle from the interface) as compared to the single-patch design.

In addition to the wettability and surface patterning, it has been shown that the shape of Janus particles has a significant influence on their surface activity [32, 50]. We will consider Janus ellipsoids of varying aspect ratio and determine their equilibrium orientation at the interface as a function of geometry and surface chemistry, and also evaluate the inter-particle forces, and preferred alignment and assembly for particle pairs.

In addition to their equilibrium orientation and interactions, Janus particles can exhibit unique dynamics which are not observed in homogeneous colloids. Currently, little is known about the diffusion and rotational dynamics of Janus nanoparticles within the interface plane. In the next step, we would like to explore how thermal motion is correlated with particle surface properties. The overall aim of this part would be to provide a quantitative analysis on the translational and rotational diffusion of Janus nanoparticles bound to interfaces as a function of particle size, amphiphilicity, fluid density, and interfacial tension.

Moreover, particle adsorption at the interface can be influenced by the presence of external flows. The third part of this research will explore the interfacial hydrodynamics and assembly of Janus particles in presence of a linear shear flow. The general goal here is to understand the molecular aspects of the response of Janus nanoparticles adsorbed at

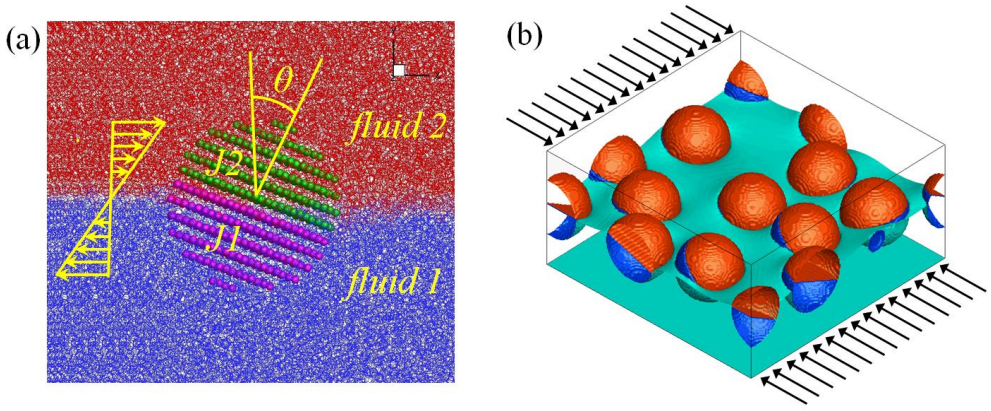

Figure 1.5 Representation of (a) a spherical Janus particle at the interface between two immiscible fluids under shear leading to an orientation angle θ, (b) multiple Janus spheres interacting under shear.

liquid–fluid interfaces to imposed shear flows, as shown in Figure 1.5(a). We will evaluate the orientational stability of Janus particles under shear as compared to their homogeneous counterparts, and the role of amphiphilicity and shear rate on tuning their preferred orientation. We will consider nanoparticles of different shapes (*e.g.* spheres, cylinders, and discs), and evaluate their dynamics, steady-state behavior, and range of attainable orientations. This enables designing nanoparticles which can yield the desired configuration at a liquid interface using the flow field as a directing mechanism. In addition to such molecular considerations, we will apply a mesoscopic analysis using Lattice-Boltzmann method to evaluate the self-assembled structures formed by the interaction of multiple Janus particles at a sheared interface shown in Figure 1.5(b). This would reveal the possibility of directing a randomly-oriented cluster of Janus particles at an interface into an ordered structure upon applying a shear flow of controlled rate, and tuning the orientational assembly of the resulting structure by adjusting the surface properties and flow parameters.

In the following chapters, each of these three parts will be explained in more details. The simulation methods and important results are presented in order to demonstrate the effectiveness of the employed tools in revealing interesting aspects of the interfacial dynamics and interactions of Janus particles.

Chapter 2

Equilibrium Orientation and Pair Interactions of Janus Particles

In general, the equilibrium orientation of Janus particles at a liquid-fluid interface is a function of particle characteristics, such as shape, size, and surface properties. For spherical particles with two sides of differing wettability, the equilibrium orientation is where each side is completely immersed in its favored fluid phase [44-46]. However, if the surface is branched such that regions of differing wettability appear on different parts on the particle, defining the equilibrium orientation becomes more complicated. For particles with anisotropic shape, if the surface is homogeneous, the equilibrium orientation is where the particle makes the largest hole in the interface [51]. For Janus particles though, this may not be the case since the reduction in interface area due to particle adsorption competes with the increase in the interfacial energy due to the exposure of surface regions to their favorable fluids. The balance between these contributions can thus lead to tilted orientations and interesting interfacial behavior.

If the equilibrium orientation of the particle leads to a surface heterogeneity along the contact line, the interface will deform in order to satisfy the contact angle requirement. When interface distortions caused by neighboring particles overlap, long-range capillary forces arise. The nature of such interactions depends on the sign of

overlapping menisci [52]. The pair interaction potential is determined using energy landscapes as the spacing and relative orientation of the particles is varied.

Here, we consider the equilibrium configuration and capillary-induced interactions of three types of anisotropic particles: Janus spheres with two regions of differing wettability, particles with two patches branched symmetrically on a spherical base possessing different surface properties, and Janus ellipsoids incorporating anisotropy in both shape and surface chemistry. For each particle type, we will develop the energetically favorable orientation and evaluate possible interactions towards the preferred self-assembled structure.

2.1 Janus Spheres at Liquid Interfaces

For spherical Janus particles with equal coverage of the two regions where each side is completely immersed in its favored fluid at equilibrium [44-46], the contact line coincides with the Janus boundary and the interface remains flat as shown in Figure 2.1(a). As a result, no interactions due to capillarity can be envisioned. However, in practical cases such as emulsion/foam stabilization using Janus spheres, not all the particles approach the interface according to their equilibrium orientation as mentioned before. In such cases, the contact line will not coincide with the Janus boundary anymore and the interface may deform as in Figure 2.1(b) in order to minimize the surface energy of the system. Consequently, capillary-induced interactions may appear between randomly-oriented Janus spheres at the interface which can be a driving force for their assembly. We aim to obtain the interface shape and the resulting capillary forces between Janus particles of different size, wettability, and orientation.

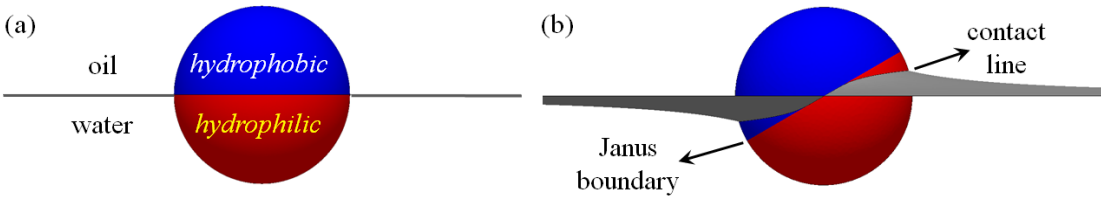

Figure 2.1 The interface deformation around a spherical Janus particle adsorbed at an oil-water interface with (a) upright, (b) tilted orientation.

Fundamental Questions

1) What is the shape of the interface around a randomly-oriented Janus sphere?, 2) What is the nature of capillary interactions that appear between neighboring particles of different orientations?, 3) How are the inter-particle forces influenced by the degree of amphiphilicity of Janus spheres?

In general, attractive or repulsive interactions may appear between particles at fluid interfaces based on how interface distortions, caused by neighboring particles, overlap. When two regions with interface distortions of equal sign superpose, the slope, and hence the area of the interface, decreases if those regions approach, leading to capillary attraction [52]. On the other hand, merging of two menisci with opposite signs leads to capillary repulsion. Same rules are expected to govern the interactions between Janus spheres where the distortion is caused by surface heterogeneity along the contact line. The extent of interface deformation would depend on the difference between the wettability of the two sides as well as the deviation from upright orientation. The relative orientations of neighboring particles and their surface properties will determine the nature of forces and therefore the separation between the particles. Another possible scenario is the in-plane rotation of neighboring particles with respect to each other, leading to a rotational relaxation until reaching the minimum energy state. We will evaluate these

possibilities to quantify the interactions and determine the equilibrium configuration of such particles at liquid interfaces.

2.1.1 Simulation Method and Surface Energy Calculation

The geometry of a spherical Janus particle is shown in Figure 2.2(a). Janus spheres are comprised of hydrophobic (apolar) and hydrophilic (polar) hemispheres of opposite wettability. The line separating the two regions is called the Janus boundary. Therefore, the perfectly smooth assumed Janus boundary corresponds to a circle of radius r_p, which can rotate with respect to particle's center of mass. The orientation angle θ_r is defined as the angle between the Janus boundary at a tilted orientation and that in the upright orientation.

The wettability of apolar and polar hemispheres of a Janus particle is defined by

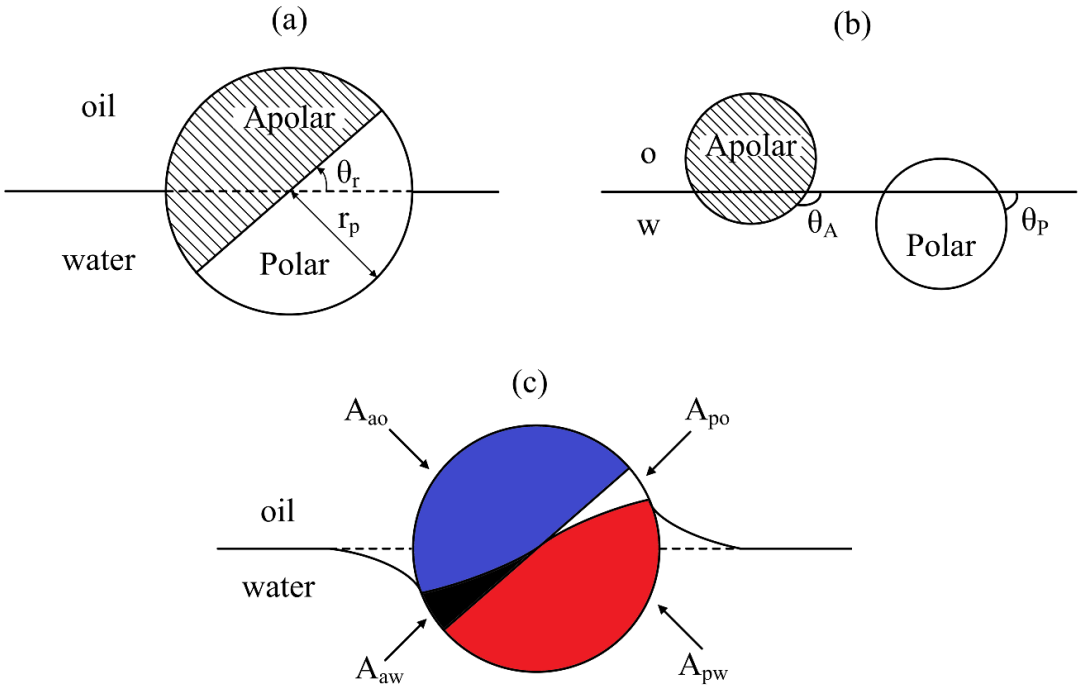

Figure 2.2 (a) Geometry of a spherical Janus particle of tilted orientation at a planar oil-water interface, (b) representation of three-phase contact angles of apolar and polar surfaces, (c) The deformed oil-water interface resulting in four particle-fluid areas.

three-phase contact angles of the two surfaces, θ_A and θ_P, as shown in Figure 2.2(b). We assume that the two regions have opposite wettabilities, represented by $\theta_A = 90^\circ + \beta$ and $\theta_P = 90^\circ - \beta$, where β is a parameter defining the amphiphilicity of the particle. At any non-equilibrium orientation, the surface of a Janus particle is divided into four regions as shown in Figure 2.2(c). The surface energy of a system of Janus particles adsorbed at the oil-water interface is thus given by

$$E_i = \gamma_{ow} A_{ow} + \gamma_{ao} A_{ao} + \gamma_{aw} A_{aw} + \gamma_{po} A_{po} + \gamma_{pw} A_{pw} \tag{2.1}$$

where γ_{ij} is the interfacial tension between i and j phases, and the subscripts, a, p, o and w indicate apolar and polar surfaces of the Janus particle, oil, and water phases, respectively. E_i refers to the surface free energy of the system when the particle is trapped at the interface. Each particle-liquid area in Eq. (2.1) is calculated numerically through a gradient descent optimization algorithm in Surface Evolver [53], such that the total surface free energy E_i is minimized.

In case of capillary interactions between neighboring particles, the surface energies are measured with respect to that of the undisturbed interface, and normalized by γr_p^2. We refer to this normalized surface energy as the "capillary energy".

2.1.2 Capillary Interactions between Janus Spheres

Here, we briefly discuss the interactions between Janus spheres trapped at the interface with tilted orientations. For any such particle, the interface takes a dipolar shape due to the tendency to minimize the surface free energy of the system. As an example, we demonstrate the calculated interface shape around two equal-sized spherical Janus particles with similar surface properties defined by $\beta = 30^\circ$ in Figure 2.3. One of the

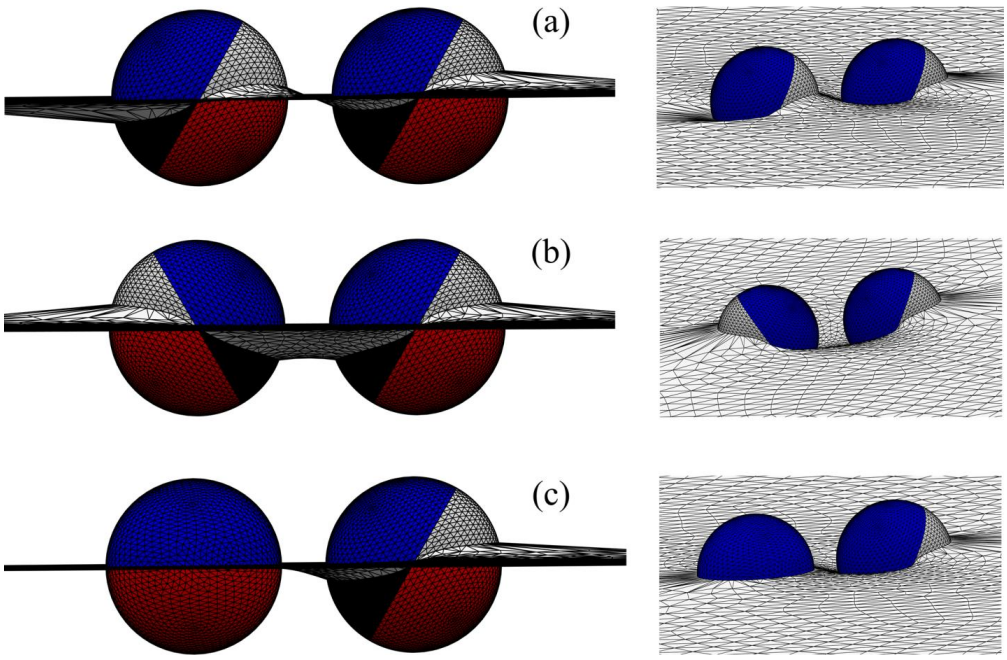

Figure 2.3 Interface deformation between two spherical Janus particles at $d_{cc} / r_p = 2.5$, $\beta = 30^\circ$, $\theta_{r1} = 60^\circ$ and (a) $\theta_{r2} = 60^\circ$, (b) $\theta_{r2} = -60^\circ$, (c) $\theta_{r2} = 0^\circ$.

particles is fixed at an arbitrary orientation angle of 60° and the orientation of the other one is varied as $\theta_{r2} = 60^\circ, 0^\circ, -60^\circ$. We note that when the orientation angles are similar as in case (a), the interface deformations caused by the particles will have opposite signs, such that each Janus sphere limits the desired deformation of the other one. For opposite orientation angles shown in case (b), the deformations possess similar signs and merge to form a "capillary bridge". Such structure has been previously observed around the flat end surfaces between two homogenous cylinders placed horizontally at a liquid-liquid interface [54]. When one particle is at the equilibrium orientation of 0° as in case (c), the interface around this particle resists against the favorable deformation caused by the other one. The overall shape of the interface will depend on the relative strength of the opposing effects induced by neighboring particles.

The capillary energies for the case of $\theta_{r1} = 60^\circ$ and various relative orientations for the other particle are plotted in Figure 2.4(a) as a function of the normalized separation

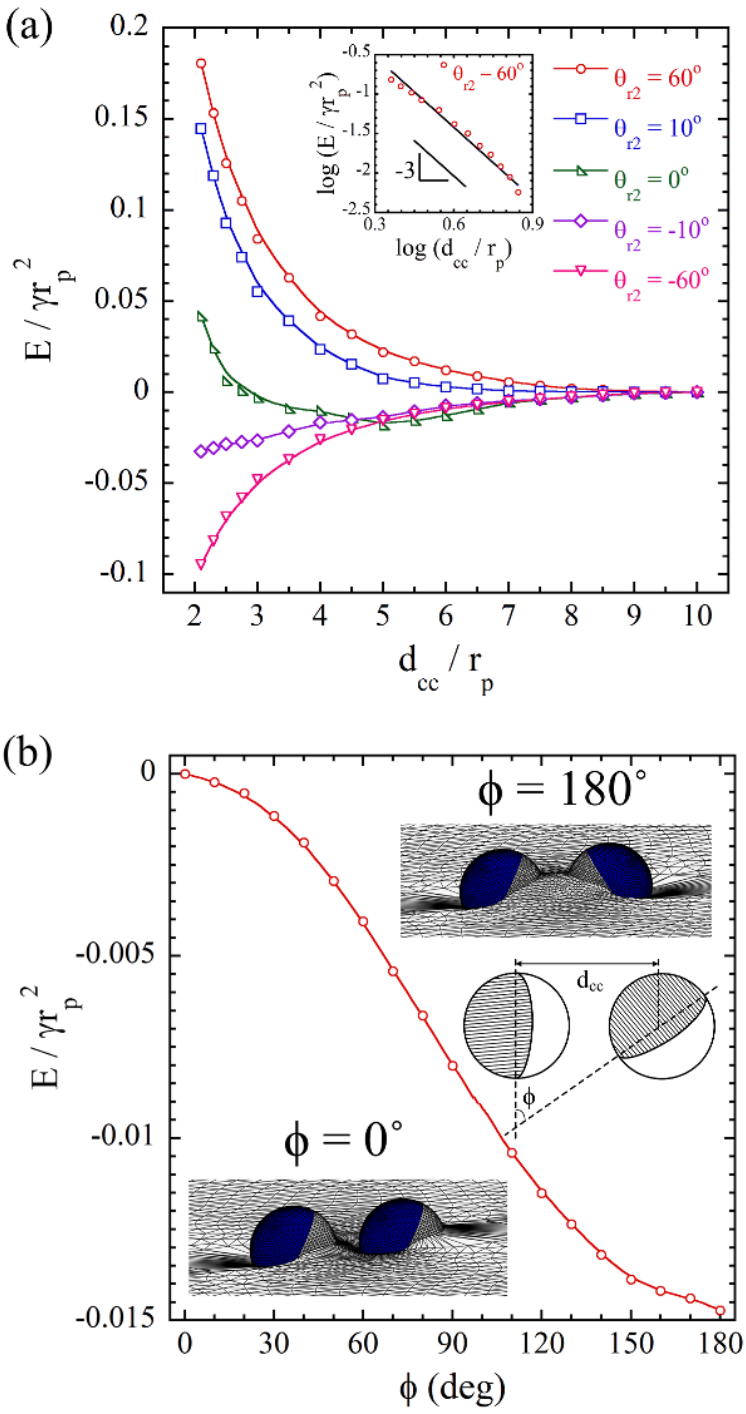

Figure 2.4 (a) Capillary energy as a function of center-to-center distance between two Janus spheres. The orientation of one particle is fixed at $\theta_{r1} = 60^{\circ}$, while the second one assumes several orientations. (b) Capillary energy vs. alignment angle for two particles at $d_{cc} / r_p = 10$, $\beta = 30^{\circ}$, $\theta_{r1} = \theta_{r2} = 60^{\circ}$.

distance. A center-to-center spacing of *10* r_p is selected as the reference value with an

assigned energy of $E = 0$. Three different regimes are observed for the interactions between Janus particles according to their relative orientations:

1- When the particles have similar orientations leading to menisci of opposite signs, the energy increases with reducing the spacing as the tendency of neighboring spheres in deforming the interface in opposite directions intensifies. As a result, the capillary force given by the slope of energy curve $F = \partial E/\partial d_{cc}$ will be negative, indicating the existence of repulsive forces between particles. The strength of repulsion increases as the deviation from equilibrium is increased.

2- In case of opposite orientations leading to overlap of menisci with similar signs, the surface energy decreases with reducing the spacing due to the formation of capillary bridge. Therefore, attractive forces appear between the particles. The strength of attraction increases as the difference between the orientation angles is increased.

3- When one particle induces negligible deformation $(\theta_r \rightarrow 0^\circ)$, an optimum spacing exists at which the surface energy is minimum due to the balance of favorable deformations around the two particles. At large separation distances, the surface area of bare oil-water interface slightly reduces without significantly affecting the particle-fluid interfacial areas of the tilted particle. As the spacing is reduced, the effect of increased energy due to unfavorable particle-fluid surface area becomes dominant compared to reduced interfacial area, resulting in increased capillary energy. Therefore, the variation of capillary energy with the spacing is a combination of attractive/repulsive regimes.

However, the particles can also undergo in-plane rotation with respect to each other in order to achieve the minimum energy state. To quantify this, we fix one of the particles and let the other one rotate around the normal to the interface plane by ϕ, as shown in the

inset of Figure 2.4(b). In case of particles with similar orientations, the plot clearly shows that as the alignment angle ϕ increases, E reduces monotonically, and the minimum occurs at $\phi = 180^{\circ}$ where similar (apolar/polar) surfaces are faced and the dipoles merge to form a capillary bridge. For this optimum alignment, the particles will then induce attractive forces and approach until they come in contact. Therefore, the relative alignment of the particles will be such that interface deformations of equal sign superpose, thus resulting in a reduction in the interface area as the particles approach. We will address the effect of amphiphilicity on the nature and strength of interactions between such Janus spheres in the next section.

From the calculated energy landscape, we determine the power-law dependency of the pair potential for two interacting Janus particles. For all relative orientations, dipolar interactions appear between the particles at small spacings, with a pair potential inversely proportional to the third power of center-to-center spacing, $E \sim d_{cc}^{-3}$. This dependency is shown for the example case of similarly oriented Janus particles by the logarithmic plot in the inset of Figure 2.4(a). As a result, the repulsive capillary forces vary as $F \sim d_{cc}^{-4}$. This indicates that the capillary interactions are induced by the superposition of dipoles, similar to the electrostatic dipole-dipole repulsion which scales as d_{cc}^{-3} [55, 56]. On the other hand, experimental measurements indicate that for particles with an upright orientation where the interface deformations arise due to corrugated Janus boundary resulting in undulated contact lines, the capillary energy varies as $E \sim d_{cc}^{-4}$ [38]. In that case, the interactions are dominated by capillary quadrupoles.

The above results indicate that Janus spheres which adsorb at a liquid-fluid interface with a tilted orientation tend to deform the interface and induce attractive/repulsive forces

based on their relative orientations. It should be emphasized though that for a single Janus particle, a capillary-induced torque is naturally forcing the particle to rotate towards the minimum energy state corresponding to $\theta_r = 0^\circ$. However, in case of two neighboring particles and specially in practical (Pickering) systems where multiple particles interact, the particles may be locked at a tilted orientation due to the reduced capillary energy caused by merging of interface distortions. Under such conditions (as suggested by previous experimental observations [1, 38]), the interface shape is governed by the dipole-dipole interaction. To further clarify this, note that in general, the solution of Young–Laplace equation in polar coordinates gives the interface height relative to the far-field planar level as a combination of multipoles [57]

$$h(\mathrm{r}_c, \varphi) = \sum_{m=0}^{\infty} H_m \cos\left(m(\varphi - \varphi_{m,0})\right) \tag{2.2}$$

where r_c is the contact radius, φ is the polar angle, H_m are the expansion coefficients, and $\varphi_{m,0}$ are the phase angles. A monopole ($m = 0$) indicates a constant rising or depression around the particle, and cannot generally occur due to lack of any external force (like gravity) dragging the particle away from its optimum height. The second term in the expansion series ($m = 1$) is a dipole, representing a symmetric rise and depression on opposite sides of the particle. This term can only occur in presence of an external torque rotating the particle away from the optimum orientation relative to the interface. Since we are assuming that the particles are locked at tilted orientations, the dipole is the lowest allowable multiple order, which is consistent with our simulations showing dipolar deformations.

2.1.3 Effect of Particle Amphiphilicity on Capillary Interactions

As mentioned before, the effectiveness of colloidal particles in stabilizing Pickering systems can be significantly increased through using the amphiphilic nature of Janus particles. Under non-equilibrium conditions, the degree of amphiphilicity plays an important role in governing the interface shape and assembly behavior of Janus particles. In this section, we tune the difference in wettability of apolar/polar regions and evaluate the surface free energy variation for two Janus spheres at an oil-water interface. Figure 2.5(a) shows the capillary energy as a function of normalized center-to-center separation distance for the case of opposite orientation angles of $\theta_{r1} = 60^{\circ}$, $\theta_{r2} = -60^{\circ}$. Note that if the particles possess similar orientations of $\theta_{r1} = \theta_{r2} = 60^{\circ}$, they will undergo rotational relaxation and yield a configuration similar to this case. Increasing the particle amphiphilicity results in the formation of a stronger capillary bridge due to increased interface distortion. As a result, the capillary energy falls more quickly as the particles approach each other, and the attractive forces become stronger. The capillary force between the particles in contact (F_c) can be calculated from the derivative of energy with respect to d_{cc}. For the cases shown in Figure 2.5(a), the dimensionless forces vary in a range of $F_c / (\gamma r_p) \sim 0.032 - 0.104$ for different values of β, with an increasing value for more amphiphilic particles.

For the case where one of the particles is near the equilibrium orientation and the interactions are of a combined attractive/repulsive nature (*e.g.* $\theta_{r1} = 60^{\circ}$ and $\theta_{r2} = 0^{\circ}$), the variation in surface energy with center-to-center separation is plotted in Figure 2.5(b). Increasing the wettability difference between apolar and polar regions amplifies the attractive forces at relatively large spacings ($d_{cc} / r_p > 5$). On the other hand, as the

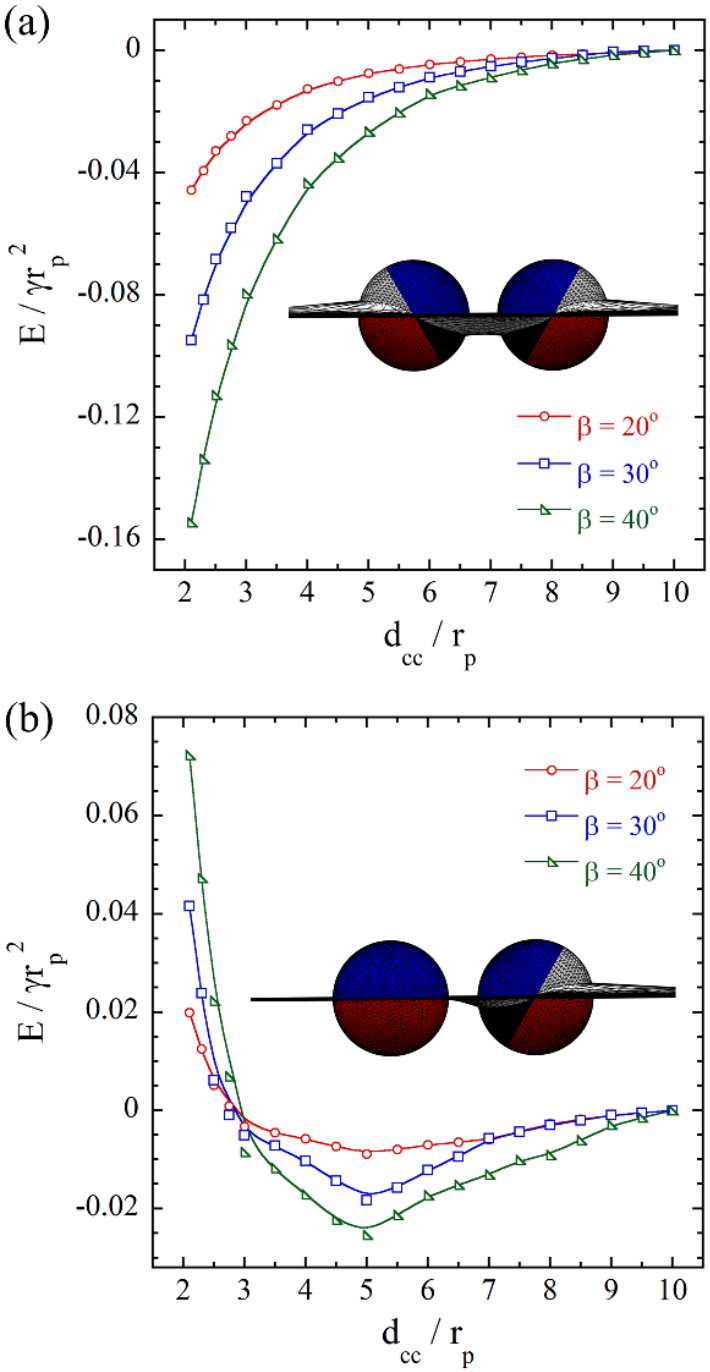

Figure 2.5 Variation of capillary energy with separation distance between two Janus spheres for different amphiphilicities at orientations of (a) $\theta_{r1} = 60^{\circ}$, $\theta_{r2} = -60^{\circ}$, (b) $\theta_{r1} = 60^{\circ}$, $\theta_{r2} = 0^{\circ}$.

spacing is reduced, increasing β induces stronger repulsions as a result of the faster energy increase. The increased variation of surface energy with the spacing is again

attributed to larger extent of interface distortion for more amphiphilic particles as a result of their tendency to reduce unfavorable particle-fluid surface area.

2.2 Interfacial Activity of Single– and Double–Patch Spheres

A Janus sphere is defined as a particle comprised of two hemispheres with different wettability. Breaking the symmetry in surface coverage of these two regions or patterning the surface into several regions of differing wettability results in a more general family of colloids, known as "Patchy particles". Therefore, patchy particles can be considered as colloids in which anisotropic surface functionality is not restricted to the symmetric case. They possess at least one well-defined patch and can experience strongly anisotropic, highly directional interactions with other particles or surfaces. Under this definition some biological entities such as globular proteins can be categorized as patchy particles. It has been shown that the rational design of the patch shape and symmetry can drive crystallization of patchy colloids into a selected morphology [58-61]. On the other hand, patterning well-defied patches may result in particles with stronger interfacial activity in comparison with the symmetric case of Janus spheres. Evaluating the positioning and interactions of such particles at a liquid interface can also give insight into the structure of natural systems such as protein molecules interacting at biological interfaces. The

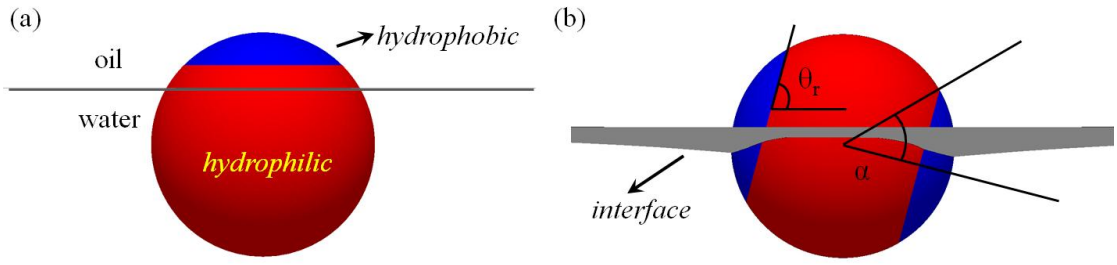

Figure 2.6 Patchy particles with (a) one, (b) two patches of well-defined size and wettability adsorbed at an oil-water interface. The orientation angle of the double-patch particle is characterized by θ_r.

literature however, is very limited on quantifying the interfacial behavior of amphiphilic particles with regions of unequal surface area despite considerable progress in their manufacturing methods [29, 39, 46].

Several varieties of patchy particles with different patch pattern, size, location, and number can be envisioned. Here, we consider the adsorption of spherical particles with one and two well-defined patches to flat liquid–fluid interfaces, as demonstrated in Figure 2.6.

Fundamental Questions

1) Given two surfaces with prescribed wettability, what is their best distribution on a sphere resulting in maximum surface activity?, 2) If we branch one of the surfaces into two symmetric patches on a spherical base, what is the equilibrium orientation of such double–patch particle as a function of patch size and surface properties?, 3) Under what conditions do these particles cause interface distortion and thus capillary interactions?, 4) Which of the single– and double–patch designs provide higher surface activity?

The single–patch design is basically a Janus sphere with asymmetric distribution of surface regions; therefore, it does not deform the interface as the contact line will always be homogeneous [46]. For the single–patch particle with any two given wettability, we will determine the optimum distribution of surface areas which will maximize the surface activity of the particle. For the more intricate double–patch pattern, we tune the patch size and its wettability with respect to the base particle, and characterize the equilibrium orientation and surface activity. We will evaluate whether they can deform the interface

leading to capillary-induced interactions between neighboring particles, and also compare their interfacial activity with the single–patch design.

2.2.1 Optimized Surface Activity of a Single–Patch Particle

The contact angle of polar and apolar regions are characterized by θ_a and θ_p, respectively. The size of the patch regions is parametrized by the central angle α shown in Figure 2.6(b). The amphiphilicity can thus be tuned through variation of both the angle α as well as the difference between the two contact angles θ_a and θ_p. For these single–patch particles, the equilibrium orientation is clearly such that each region wets its favorite fluid to the maximum possible extent. As a result, the interface remains flat as shown in Figure 2.6(a). Depending on the relative size of the two surface regions and the contact angles, the contact line may lie below, above, or coincide with the hydrophilic/hydrophobic boundary [62]. Irrespective of that, no capillary-induced interactions is envisioned due to the flat nature of the interface as there would be no heterogeneity along the contact line.

To quantify the surface activity of the amphiphilic particle, the minimum among detachment energy from oil and water phases (ΔE_o and ΔE_w) should be determined based on geometrical parameters and surface properties. For an amphiphilic particle with $\theta_a > 90^\circ$ and $\theta_p < 90^\circ$, equating ΔE_o and ΔE_w leads to the critical size of the apolar region, characterized by α_{cr}, at which the energy reduction upon particle adsorption from both fluid phases to the interface are equal. Through analytical calculations, we found [62]

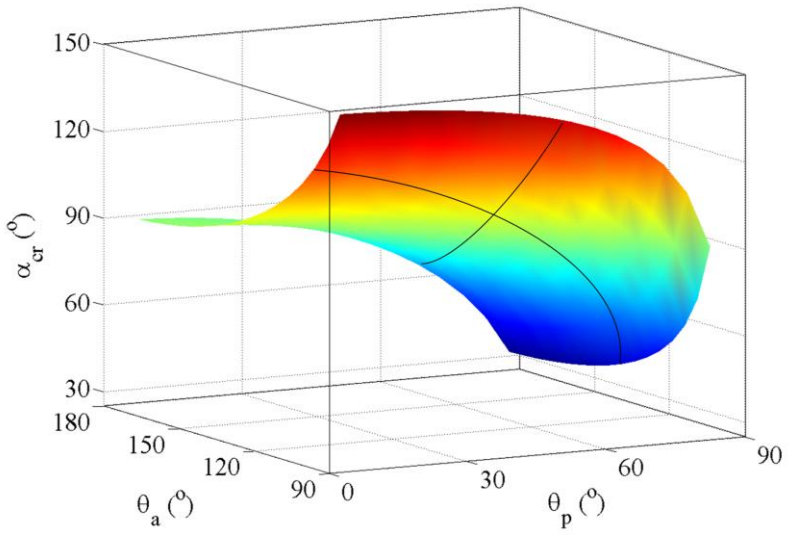

Figure 2.7 A 3D contour plot of the critical size distribution α_{cr} as a function of the wettabilities θ_a and θ_p for two regions of an amphiphilic particle.

$$\alpha_{cr} = \cos^{-1}\left(\frac{\cos\theta_a + \cos\theta_p}{\cos\theta_a - \cos\theta_p}\right) \tag{2.3}$$

A three-dimensional contour plot of the critical size distribution is shown in Figure 2.7 as a function of the wettabilities θ_a and θ_p. If the regions are divided according to $\alpha < \alpha_{cr}$, the detachment energy into the aqueous phase is reduced, while for $\alpha > \alpha_{cr}$, the particle requires less energy for detaching into the oil phase. Therefore, the minimum detachment energy has its largest possible value at $\alpha = \alpha_{cr}$. In other words, given the wettabilities θ_a and θ_p, the most surface active particle is the one in which the surface areas are distributed according to $\alpha = \alpha_{cr}$, where α_{cr} is given by Eq. (2.3). For an example case of a particle with $\theta_p = 30^\circ$ and $\theta_a = 120^\circ$, the critical size distribution is found as $\alpha_{cr} = 105^\circ$. This indicates that for such particle, the apolar region should cover a slightly larger surface area than the polar region.

2.2.2 Interfacial Configuration of Double–Patch Particles

Having quantified the surface activity of single–patch particles, we would like to evaluate whether branching the hydrophobic patch into two regions on opposite sides of the particle can enhance the detachment energy. For such design, it is impossible for both patch groups to be immersed in their favorable fluid simultaneously. As a result, either each patch will be completely surrounded by a different fluid phase as in Figure 2.8(a), or both patches will cross the interface plane as in Figure 2.8(b). In the latter case, there is a heterogeneity along the contact line, leading to a deformed meniscus. Our simulations suggest that the interface takes a quadrupolar shape, with two rises on the polar region and two depressions on symmetric patches. The meniscus height is controlled by the patch size and the difference in wettability of the apolar and polar regions. This prediction is consistent with the theoretical analysis of interface shape around colloidal particles discussed in section 2.1.2. According to Eq. (2.2), the quadrupole ($m = 2$) is the lowest allowable multipole term in the absence of external force and toque. Quadrupolar deformations also arise in case of homogeneous particles with anisotropic shapes, *e.g.* rods or ellipsoids [63]. In that case, the maximal difference in meniscus elevation around the particle depends on its aspect ratio and three-phase contact angle.

If the patches cross the interface plane, the surface areas have to be calculated numerically, similar to the case of Janus spheres with tilted orientations. The interfacial areas depend on the orientation of the patch boundaries relative to the interface plane, designated by θ_r in Figure 2.6(b). We calculate the total surface free energy of the system at each orientation angle. The equilibrium orientation is then identified as the case where the total surface energy is minimized.

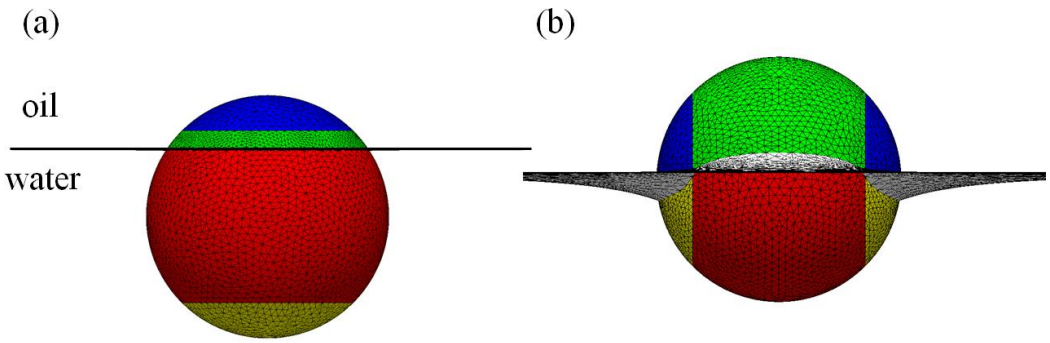

Figure 2.8 Interface shape around a spherical patchy particle with a base wettability of θ_p = 60˚, and two symmetric patches with θ_a = 120˚ and a size of α = 45˚, when the patches are (a) parallel and (b) normal to the interface.

As an example, Figure 2.9(a) shows the variation in surface energy as a function of the orientation angle for the case of $\theta_p = 60^\circ$ and $\alpha = 45^\circ$, and three different wettabilities of the (apolar) patch regions. The surface energy at $\theta_r = 0^\circ$ is assigned a value of $E_i = 0$, and that of the other orientations are measured with respect to this reference value. As expected, the surface energy variation is symmetric about $\theta_r = 90^\circ$ due to symmetric positioning of the patch groups on the particle. Irrespective of the patch wettability θ_a, the minimum surface energy occurs at $\theta_r = 0^\circ$, which corresponds to the parallel-patch orientation. The surface energy remains constant as the particle is rotating up to a point where the upper patch begins to enter the water. Since the patch is apolar and repels the aqueous phase, the surface energy increases. The interface distortion resulted from the heterogeneity along the contact line also contributes to the increased energy.

Further rotating the particle results in the exposure of the opposite patch to the oil phase, which is energetically favorable. As a result, the surface free energy drops until $\theta_r = 90^\circ$, after which the trend is reversed. The energy landscapes thus reveal the existence of a local energy minima at $\theta_r = 90^\circ$, *i.e.* the normal patch orientation. This indicates that the particles can be kinetically trapped in a metastable orientation, under appropriate

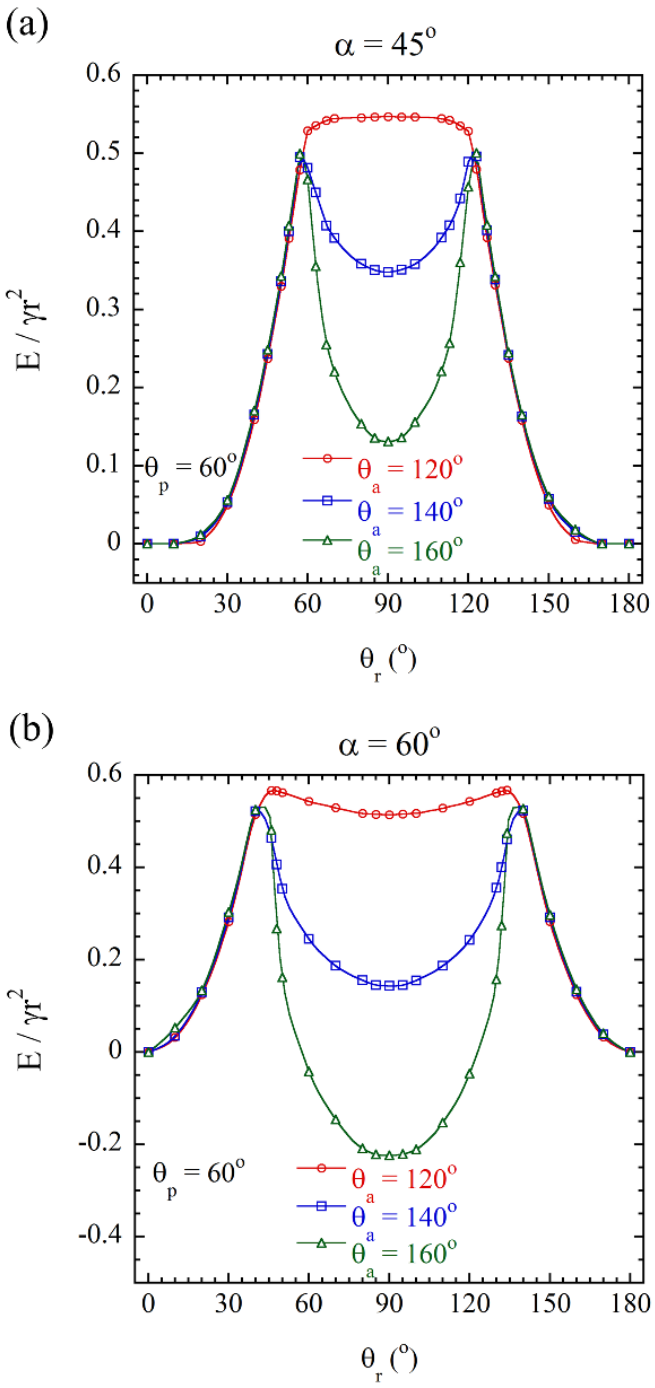

Figure 2.9 Surface energy vs. orientation angle for a patchy particle with a base wettability of $\theta_p = 60^\circ$, and two apolar patches with θ_a and a size of (a) $\alpha = 45^\circ$, (b) $\alpha = 60^\circ$: the equilibrium orientation characterized by minimum energy state shifts based on patch size and amphiphilicity.

conditions. We note that for the case of $\theta_a = 120^\circ$, the increased oil-water surface area

caused by interface distortion dominates the reduction in surface energy due to increased apolar-in-oil surface area. This results in the absence of the metastable state for a particle of such geometry and surface properties.

Figure 2.9(b) represents the variation in surface energy as the patch size is increased to $\alpha = 60^\circ$. Compared with case (a), we observe that at each corresponding value of θ_a, increasing the patch size results in a larger decrease in surface energy as $\theta_r \rightarrow 90^\circ$. This is due to the larger surface area of the apolar regions, which significantly favors the entrance of the lower patch to the oil phase. More importantly, the surface energy drop for $\theta_a = 160^\circ$ case is remarkable as it shifts the location of the global energy minima to $\theta_r = 90^\circ$. Consequently, the equilibrium orientation of such particles corresponds to a condition where the interface crosses both apolar and polar regions and the patch boundaries are normal to the interface. Our simulations indicate that further increasing the patch size shifts the global energy minimum and thus the equilibrium orientation to $\theta_r = 90^\circ$ even for less hydrophobic patches.

For any two given wettabilities, we found that there is a transition patch size characterized by α_{tr} above which the patches are preferably oriented normal to the interface. Such criterion is determined by comparing the surface free energies at $\theta_r = 0^\circ, 90^\circ$ orientations as α is varied. Figure 2.10 shows a three-dimensional contour plot of α_{tr} as a function of the contact angles θ_a and θ_p. Particles for which the patch size α lies below this surface take a parallel-patch orientation at equilibrium, while those located above the surface orient with their patches normal to the interface. We note that at a constant base wettability θ_p, patches with lower hydrophobicities require an increased patch size α to induce transition to normal patch alignment. Reducing patch

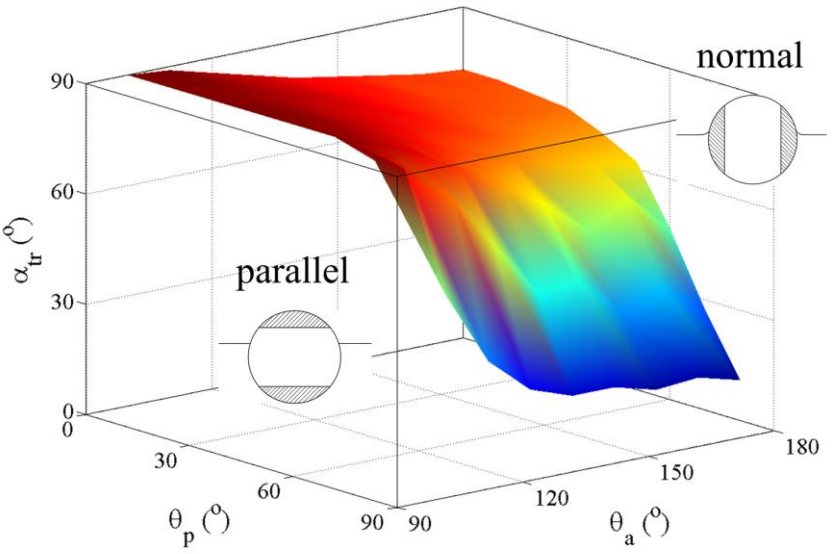

Figure 2.10 A 3D contour plot of the transition patch size α_{tr} for a spherical double-patch particle as a function of the polar and apolar wettabilities, θ_p and θ_a.

hydrophobicity lowers their affinity to the oil phase. Consequently, a larger surface area of the patches has to be immersed in water to satisfy the contact angle requirement, leading to an increase in the total surface energy of the system for normal-patch orientation. On the other hand, the transition patch size generally reduces as θ_p is increased towards 90°. This is due to the reduction in interface deformation in the central (hydrophilic) region which results in a decrease in total surface energy at a specific patch size. As a result, the normal-patch orientation would be preferable for particles with smaller area of apolar regions. The plot in Figure 2.10 enables calculation of transition patch size over a wide range of surface properties. It can provide guidelines for synthesizing patchy particles to achieve desired orientation at liquid-fluid interfaces.

2.2.3 Capillary Interactions between Neighboring Double–Patch Particles

If the two patches cross the interface at equilibrium, a quadrupolar interface deformation arises around the particle. In that case, overlapping of distortions caused by two neighboring spheres can give rise to energetic capillary interactions. These interactions can be both attractive and repulsive, depending on the sign of the meniscus slopes in overlapping region [64, 65]. When two similar particles with menisci of the same sign approach one another as in Figure 2.11(a), the surface area is lowered, and the free energy of the system decreases correspondingly. This leads to an attractive capillary force between the particles. On the other hand, when the particles possess patches of opposite wettabilities, two menisci are in different directions as in Figure 2.11(b). In that case, the particles may rotate azimuthally to induce merging of menisci with similar signs and appearance of attractive forces.

To evaluate the nature of interactions, we obtain the pair potential between two neighboring patchy particles as a function of the inter-particle spacing. For each configuration, the optimized interface shape leading to minimum surface energy is numerically calculated. We assign a value of $E_i = 0$ for surface energy at large spacings, and that of closer distances are measured with respect to this reference value. Therefore, this will result in a negative pair potential U_{cap} in case of capillary attraction and a

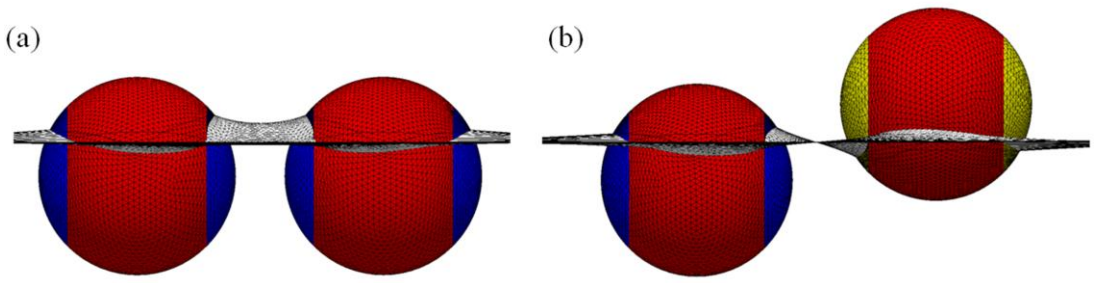

Figure 2.11 Interface deformation between two spherical patchy particles with (a) hydrophilic patches, (b) hydrophilic/hydrophobic patches, leading to similar and opposite direction of interacting menisci.

positive potential for repulsion. Figure 2.12 shows the pair potential for two neighboring particles composed of various patches as a function of center-to-center separation. The particles possess similar base wettability of $\theta_p = 90^\circ$, a patch size of $\alpha = 45^\circ$, and are positioned according to their equilibrium orientation angle of 90° with respect to the interface. The wettability of patch groups on one particle is fixed at $\theta_{a1} = 30^\circ$, while that of the second particle is varied over a wide range. Three main regimes are observed for the interactions between particles (analogous to the case of Janus spheres):

(1) When both particles possess hydrophilic (or hydrophobic) patches, the two neighboring menisci have similar signs. Consequently, the surface area is lowered upon reducing the inter-particle distance, leading to a negative pair potential ($U_{cap} < 0$). The

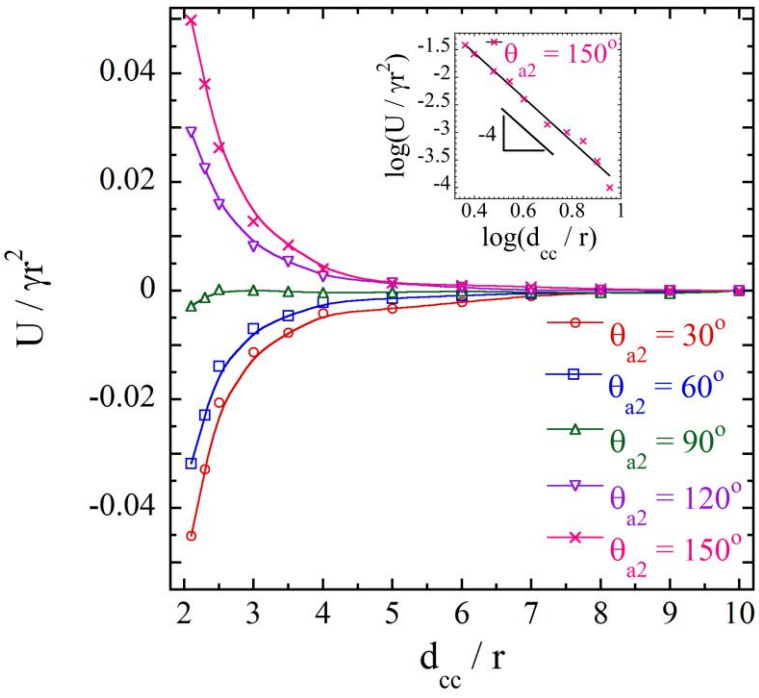

Figure 2.12 Capillary pair potential as a function of the center-to-center distance between two patchy particles with base contact angle of $\theta_p = 90^\circ$, normally-oriented patches of size $\alpha = 45^\circ$ and wettability of $\theta_{a1} = 30^\circ$ and several θ_{a2} (a logarithmic plot for the case of $\theta_{a2} = 150^\circ$ is shown in the inset).

capillary force given by the slope of the curve $F_{cap} = \partial U_{cap} / \partial d_{cc}$ will thus be positive, indicating the existence of attractive forces between the particles.

(2) In case of two particles having patch groups with opposite wettabilities, the neighboring menisci have reverse signs, and the interfacial energy increases by reducing the spacing. As a result, the pair potential is positive ($U_{cap} > 0$) and the capillary force has a repulsive nature. However, it is energetically favorable for the particles to undergo a rotational relaxation, leading to overlap of menisci with similar signs and thus inducing attractive forces (as seen in the case of Janus spheres [66]). Therefore, the particles shown in Figure 2.11(b) will rotate such that the patch of one interacts with the base region of the other particle thus leading to attraction.

(3) When one particle induces no interface distortion as it becomes homogeneous ($\theta_{a2} = \theta_{p2} = 90^\circ$), the pair potential due to capillarity becomes negligible. At very close spacings, the homogeneous particle can have a slight influence on the interface shape around the neighboring particle, but the surface energy does not considerably change. In such case, other interacting mechanisms such as electrostatic forces or gravity-induced deformation may have the dominant effect.

The power-law dependency of the pair potential for two interacting double-patch particles can be verified using the energy landscape. For all cases of neighboring menisci with similar and opposite signs, quadrupolar interactions are found between the particles, with a pair potential inversely proportional to the fourth power of center-to-center spacing, $U_{cap} \sim \mathrm{d}_{cc}^{-4}$. This dependency is shown for the example case of particles with opposite patch wettabilities ($\theta_{a1} = 30^\circ$, $\theta_{a2} = 150^\circ$) by the logarithmic plot in the inset of Figure 2.12. A linear fit with a slope of *-4* accurately matches the numerical data. As a

result, the capillary force varies as $F_{cap} \sim d_{cc}^{-5}$. This confirms that the interactions are induced by the superposition of quadrupoles, similar to those reported in the literature for homogeneous ellipsoids [51, 63].

2.2.4 Comparison between Surface Activity of Single– and Double–Patch Particles

Finally, it would be crucial to determine the effectiveness of patterning symmetrical patches on spherical particles in improving their surface activity. If the patches are oriented parallel to the interface under equilibrium conditions and $\Delta E_w < \Delta E_o$, the minimum detachment energy will be equivalent to that of a single-patch particle where an equal-sized apolar patch lies in the oil phase. On the other hand, if the particle takes a normal-patch orientation, the detachment energy may increase or decrease through incorporation of the second patch group. The interfacial energy of the bare oil-water interface ($\gamma_{ow}A_{ow}$) rises as a result of the interface deformation around the heterogeneous contact line. However, the surface energy of the particle-fluid regions is reduced when lager surface areas of the apolar patches are immersed in their favorable fluid. The superposition of these two effects determines the variation in total surface energy of the particle, and its detachment energy from the interface.

We considered single- and double-patch particles with equal patch size and wettability for two different sizes of $\alpha = 45^\circ, 60^\circ$. The spherical base is assumed to be polar, with a contact angle of $\theta_p = 80^\circ$. Figure 2.13 shows the minimum detachment energy for the two considered patchy particle designs. We note that at $\alpha = 45^\circ$, incorporation of the second patch increases the minimum detachment energy (and thus the surface activity) of the particle up to $\theta_p \approx 150^\circ$, while it has a negative effect for larger

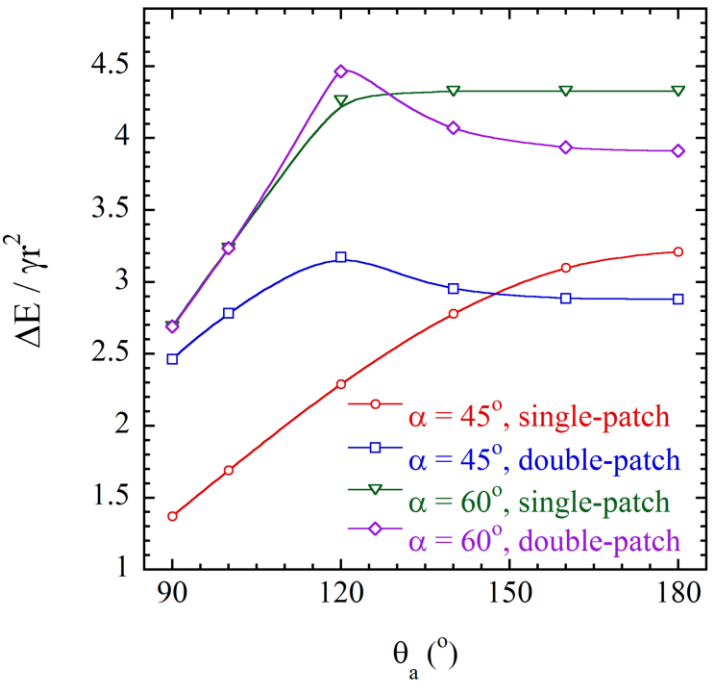

Figure 2.13 Minimum detachment energy for spherical particles with $\theta_p = 80^\circ$ and one/two patterned patches of different sizes as a function of the patch wettability θ_a.

hydrophobicities. This can be attributed to the larger extent of interface deformation and thus an increase in total surface energy E_i upon increasing θ_a. Enlarging the patch size to $\alpha = 60^\circ$ enhances the interface distortion, such that the increase in detachment energy becomes less significant. On the other hand, for patches of an intermediate size, the normal-patch orientation is only accessible to particles with a relatively large θ_p. Therefore, we conclude that grafting a symmetric patch group onto a spherical particle can be helpful for relatively small patches when θ_a , θ_p are close to 90°, while it reduces the surface activity for highly amphiphilic particles. This analysis can thus provide useful criteria for designing patterned particles with maximum surface activity for applications involving liquid-fluid interfaces.

2.3 Interfacial Configuration of Non-Spherical Janus Particles

An additional degree of freedom in tuning the interfacial behavior of Janus particles can be achieved by using anisotropic geometries. Janus particles can currently be fabricated in a variety of shapes including discs, cylinders, ellipsoids, and dumbbells [67-69]. Theoretical considerations demonstrate that the geometry as well as the wettability of such non-spherical Janus particles have a significant influence on their surface activity [32, 50]. The aspect ratio of such particles (*e.g.* Janus ellipsoids) can be readily tuned using a mechanical stretching method [70, 71]. Moreover, surface modification of each side of the particle enables tailoring its orientation at the interface, which can lead to a variety of self-assembled structures [72, 73]. As a result, identifying the effect of geometry and surface properties is critical in effectively utilizing these particles as building blocks and surface active agents in multiphasic systems. We employ ellipsoidal particles with varying aspect ratio and amphiphilicity, and evaluate their orientation and interactions at a planar liquid interface.

Fundamental Questions

1) What is the interface shape around ellipsoidal Janus particles?, 2) For two neighboring ellipsoids, what is the dependency of pair interaction potential on their size, aspect ratio, and surface properties?, 3) How do Janus ellipsoids align with respect to each other at equilibrium, and which parameters influence their preferred configuration?

Particles with anisotropic shape generally distort the interface as the flat interface cannot satisfy the contact angle requirement. For instance, experimental observations indicate a quadrupolar interface deformation around homogeneous ellipsoids, leading to long-ranged quadrupolar attraction bringing the particle tips in contact [74]. However, the

presence of chemical heterogeneity in Janus particles substantially changes the meniscus shape around the particles. This can result in a deviation of the pair interaction potential from the quadrupolar form of homogeneous ellipsoids. The difference between the wettability of the two regions is an important parameter in defining the magnitude of capillary forces and the resulting assembly of these particles. We will evaluate the equilibrium configuration and capillary-induced interactions between such particles. In this case, the interface deformation is induced by a combination of shape anisotropy and surface heterogeneity.

2.3.1 Equilibrium Orientation of Isolated Ellipsoids

The geometry of Janus particles under consideration is shown in Figure 2.14(a). The aspect ratio, *AR*, is characterized as the ratio of axis lengths: $AR = c / a$. The surface area of all ellipsoidal particles is set to $A = 4\pi r_s^2$, where r_s represents the radius of a corresponding spherical particle ($AR = 1$). The orientation angle θ_r is defined as the angle between the particle's long-axis in the upright orientation (*i.e.*, the long axis of ellipsoid perpendicular to the interface) and that in a rotated orientation. Similar to Janus spheres, we assume that the two regions have opposite wettabilities, represented by $\theta_a = 90^\circ + \beta$ and $\theta_p = 90^\circ - \beta$.

The surface energy is calculated based on Eq. (2.1) as a function of the orientation angle θ_r for different particles and the equilibrium orientation corresponding to minimized surface energy is determined. Figure 2.14(b) shows the equilibrium orientation of isolated Janus ellipsoids as a function of their aspect ratio. As the aspect ratio is increased, the equilibrium orientation of Janus ellipsoids is dominated by the

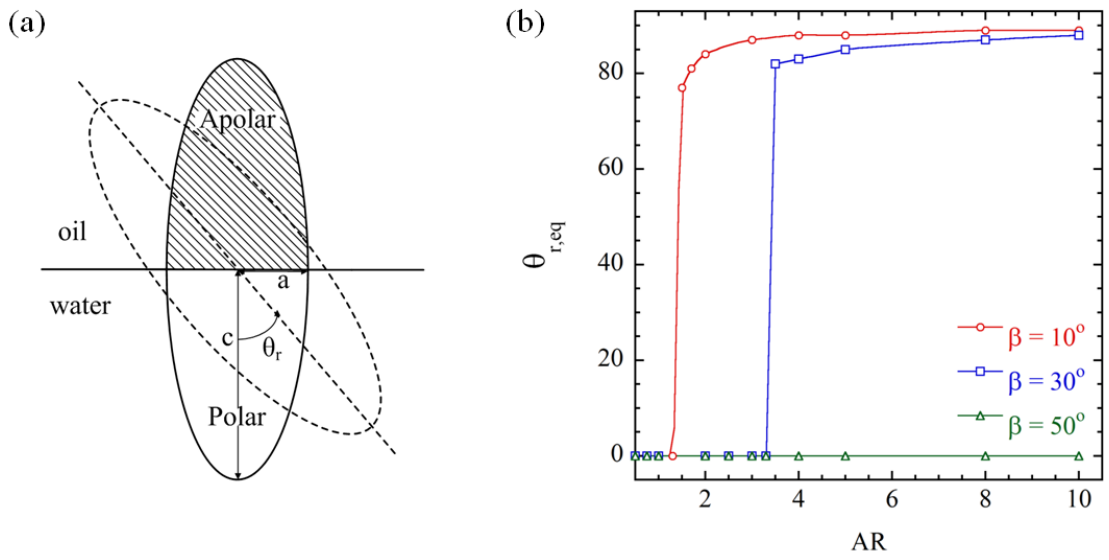

Figure 2.14 (a) Geometry of an ellipsoidal Janus particle at a planar oil-water interface, (b) Equilibrium orientation of isolated Janus ellipsoids at a liquid interface as a function of the aspect ratio (AR) and amphiphilicity (β).

tendency to reduce the bare oil-water interfacial area, and in turn, the interfacial energy. Consequently, a tilted orientation is preferred at equilibrium. On the other hand, increasing the amphiphilicity enhances the affinity of apolar and polar regions to oil and water phases, respectively. As a result, the particle's tendency to reduce the attachment energy by increasing the interfacial area between each region and its preferred fluid phase has a dominant effect on inducing the upright orientation. We conclude that in contrast to Janus spheres (*AR = 1*), prolate ellipsoids with large aspect ratio or small amphiphilicity tend to take a tilted orientation at equilibrium, which can lead to interface distortion and inter-particle forces.

The interface shape around ellipsoidal particles of various shape and surface chemistry is numerically calculated. As an example, Figure 2.15(a) shows the interface formed around a homogeneous ellipsoid with three-phase contact angle of $\theta = 60^{\circ}$ and an aspect ratio of *AR = 3*, placed according to its equilibrium orientation at the interface. We

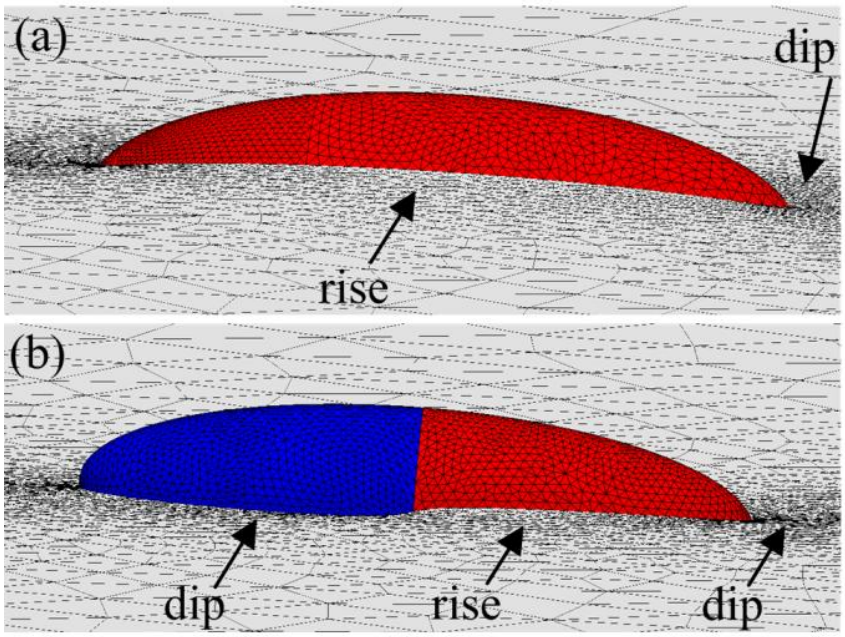

Figure 2.15 Interface shape around isolated ellipsoidal particles of AR = 3 at their equilibrium orientations for (a) a homogeneous particle with $\theta = 60^{\circ}$, (b) a Janus particle with $\beta = 10^{\circ}$.

observe that the interface is *quadrupolar*, with rises along the sides and depressions on the tips. This is in agreement with the analytical solution to Young-Laplace equation based on multipole expansion of the interface shape discussed in section 2.1.2 [75]. However, the interface shape can be significantly affected in presence of a surface heterogeneity. Figure 2.15(b) shows the interface shape for a Janus ellipsoid of similar geometry and an amphiphilicity of $\beta = 10^{\circ}$. We note that in this case, the interface takes a *hexapolar* shape, with three rises and three dips distributed around the particle. The sign of meniscus height with respect to far-field elevation is changed as it passes through the Janus boundary, due to opposite affinity of the two regions to fluid phases. This results in two additional poles around the particle compared to the homogeneous case. The extent and positioning of the rises and dips can be tuned through modification of particle

amphiphilicity and aspect ratio, suggesting a complex variation of meniscus shape around Janus ellipsoids.

2.3.2 Interaction and Alignment of Janus Ellipsoids

After evaluating how isolated Janus ellipsoids of various geometry and amphiphilicity orient at the interface, we can quantify the interactions between neighboring particles. For ellipsoids with large aspect ratio or small amphiphilicity range, the equilibrium orientation will be tilted leading to interface deformation. As a consequence, neighboring particles will interact through capillary interactions induced by the overlap of deformed menisci. The interface shape and consequently, the extent of inter-particle forces are generally different from the case of particles possessing homogeneous surface properties. We would like to understand how various parameters (*e.g.* particle shape, amphiphilicity, relative size, and in-plane alignment) will govern the nature and magnitude of interactions. Energy landscapes enable the calculation of power law dependency of pair potential on the inter-particle distance for pairs of Janus ellipsoids.

Our simulations indicate that similar to Janus spheres, pairs of ellipsoids also orient such that regions of similar wettability are faced [76]. As a consequence, a capillary bridge is formed and the particles approach until contact. While the particle orientation normal to the interface plane is fixed by $\theta_{r,eq}$ given in Figure 2.14(b), the particles can rotate about each other within the interface plane, giving rise to a preferred alignment. Figure 2.16(a) depicts the orientation of two neighboring Janus ellipsoids looking downward at the interface. The angle between long axes of the particles is designated as

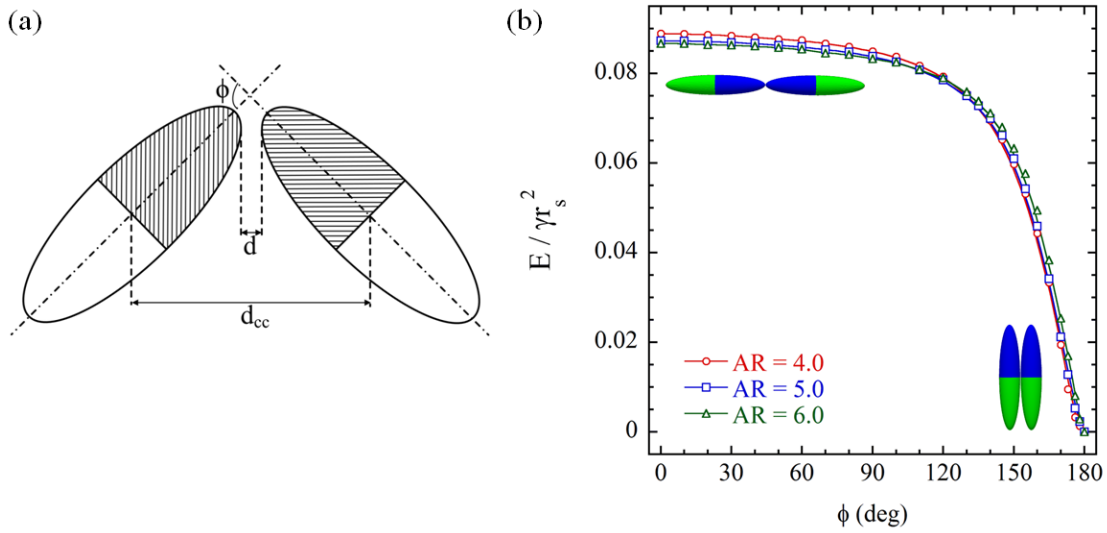

Figure 2.16 (a) Parameters defining the interfacial configuration of two neighboring Janus ellipsoids within the interface plane (top view), (b) Capillary energy in contact for ellipsoids of similar geometry and β = 30˚ as a function of the bond angle ϕ.

the bond angle ϕ. The equilibrium configuration adopted by particle pair corresponds to the angle ϕ resulting in minimum surface energy.

In order to find the equilibrium alignment, the capillary energies for ellipsoids in contact are calculated by carrying out simulations for $0^\circ \leq \phi \leq 180^\circ$. The dependence of capillary energy on bond angle for pairs of similar ellipsoids in contact is shown in Figure 2.16(b). We demonstrate the variation for particles having aspect ratios of $AR = 4$, 5, and 6, assuming a zero value for capillary energy in side-by-side alignment ($\phi = 180^\circ$). The particle pairs possess similar amphiphilicity characterized by $\beta = 30^\circ$, and are considered at their equilibrium orientation angles with respect to the interface (*e.g.* $\theta_r = \pm 85^\circ$ for $AR = 5$). The energy landscape reveals that for all geometries, capillary energy decreases monotonically with the bond angle ϕ, and the minimum occurs at side-by-side alignment ($\phi = 180^\circ$). Therefore, a side-by-side configuration is preferred for Janus ellipsoids in contact. A similar behavior has been found for homogeneous ellipsoids

through experimental and numerical investigations [69, 74]. However, we found that the capillary force at contact for side-by-side ellipsoids is *~10* times larger than that of the tip-to-tip configuration. Consequently, pairs of side-by-side Janus ellipsoids are less susceptible to break-up under the action of external forces. This is in contrast to the case of homogeneous ellipsoids where the capillary forces for both tip-to-tip and side-by-side alignments are of comparable magnitude.

Further insights into transition of particle pairs towards the optimum alignment can be inferred from the capillary torque, calculated as $T = -\partial E/\partial \phi$ and evaluated as a function of the bond angle ϕ. The torque is defined so that $T > 0$ corresponds to a capillary torque resisting rotation from the equilibrium configuration. As shown in Figure 2.17, the torque is positive for all bond angles, indicating that the particles cannot take an intermediate alignment between $0^\circ < \phi < 180^\circ$ and the capillary torque will force them to roll on each other within the interface plane towards tip-to-tip ($\phi = 0^\circ$) or side-by-side ($\phi = 180^\circ$) alignments. As a result, Janus ellipsoids do not show any metastable configuration at the interface. The capillary torque increases sharply in the neighborhood of the stable side-by-side configuration, and then slowly drops by approaching the tip-to-tip alignment. The maximum capillary torque translates into $\sim 9\times 10^5\ k_BT$ for a particle with $a = 2.5\ \mu m$ and $AR = 5$ at an oil-water interface with $\gamma = 50\ mN/m$.

Moreover, a linear relationship between T and ϕ is a good approximation for angular deviations of up to 10˚-15˚ from the equilibrium side-by-side configuration ($\phi = 180^\circ$), thus indicating a linearly elastic mechanical response to bond bending of side-by-side ellipsoids. We note that the capillary energy and torque are almost independent of the aspect ratio for Janus ellipsoids of similar surface area and amphiphilicity. It should be

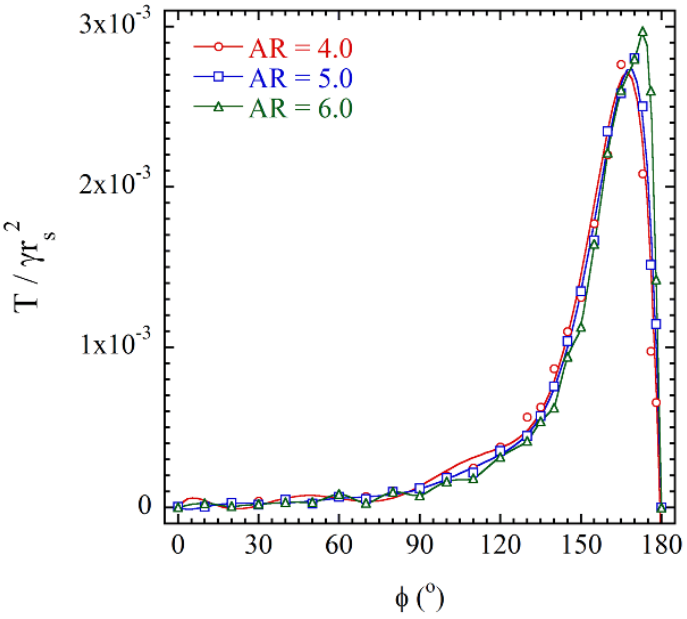

Figure 2.17 Capillary torque for a pair of ellipsoids of similar geometry and β = 30˚ in contact as a function of the bond angle ϕ.

emphasized that for Janus spheres and those ellipsoids that take the upright orientation of $\theta_r = 0^\circ$ at equilibrium according to Figure 2.14(b), the interface remains flat and the capillary force and torque go to zero.

2.3.3 Influence of Amphiphilicity and Polydispersity on the Interactions

The interfacial assembly and effectiveness of colloidal particles as stabilizing agents can be tuned through modification of particle amphiphilicity. Similar to Janus spheres, increasing the amphiphilicity results in an enhancement in capillary forces due to the increased meniscus depth as the wettability of each surface region deviates from 90°, leading to a larger reduction in the interfacial area upon overlapping of neighboring menisci. This is shown in Figure 2.18(a) by the capillary force measured as a function of normalized separation between side-by-side ellipsoids for three different values of β.

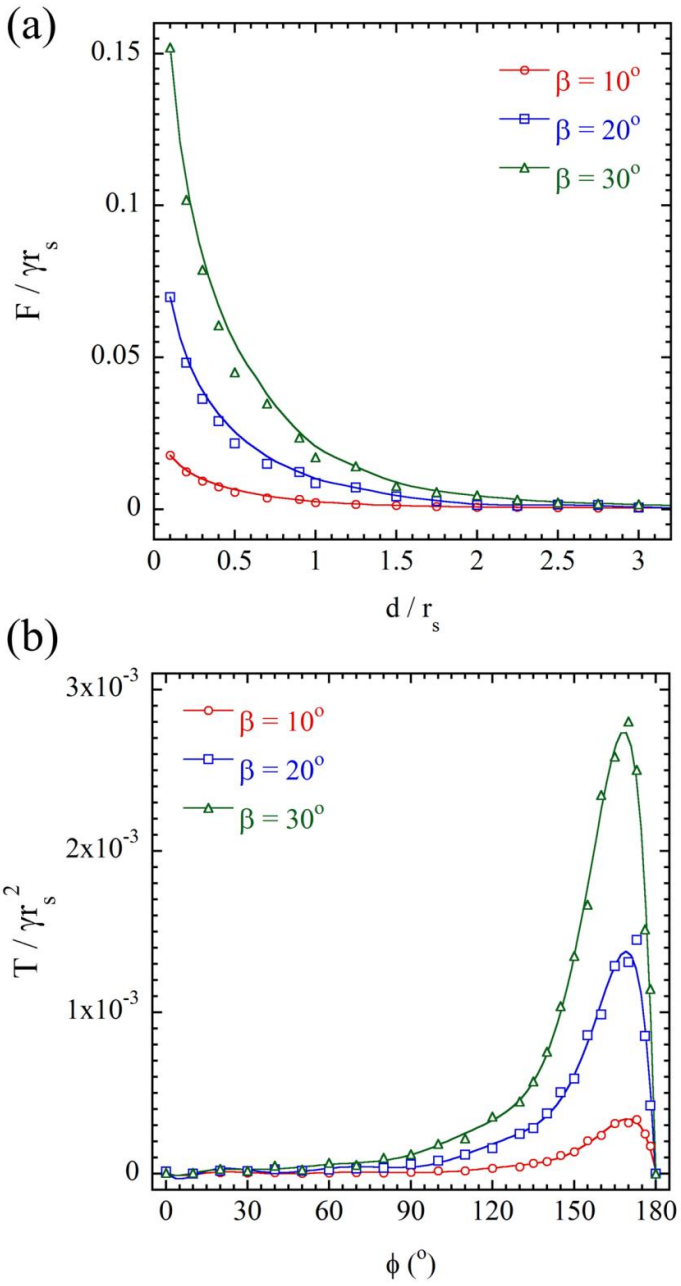

Figure 2.18 (a) Capillary force between two ellipsoidal Janus particles of AR = 5.0 , $\theta_r = 85^\circ$ in side-by-side alignment as a function of the separation distance for several amphiphilicities, (b) Capillary torque as a function of the bond angle.

Note that at the limiting case of $\beta = 0^\circ$, the particle becomes homogeneous with a contact angle of 90°, leading to a flat interface and thus no capillary-induced interactions.

Moreover, the amphiphilicity also influences the capillary torque that rotates the particles towards the equilibrium alignment. We found that the side-by-side configuration is preferable for Janus ellipsoids over a wide range of β. However, the magnitude of the capillary torque strongly depends on the amphiphilicity. Figure 2.18(b) shows the torque in contact as a function of the bond angle for pairs of ellipsoids with $AR = 5$ at equilibrium orientation. As the difference between the wettability of the two regions is increased, the capillary torque on the particles increases, thus providing a stronger barrier against rotation out of the equilibrium alignment. The maximum capillary torque increases nearly by an order of magnitude as the amphiphilicity is increased from $\beta = 10^\circ$ to 30°. In addition, all the curves show a linear variation in T for small deviations of ϕ from equilibrium, with an increased slope for larger β values. This indicates that the linearly elastic mechanical response to bond bending of ellipsoids from side-by-side alignment increases upon increasing the amphiphilicity.

On the other hand, the pair interaction potential between two Janus particles generally depends on their aspect ratio. In practical cases such as in stabilization of Pickering systems, particles with a non-uniform size distribution may be present, and we would like to understand the nature of energetic interactions when particles of dissimilar geometry interact at the interface. Let's consider a typical Janus ellipsoid with $AR_1 = 5$ approaching a particle with a different aspect ratio AR_2. The particles will undergo a rotational relaxation within the interface plane in order to minimize the total surface free energy of the system. By evaluating the capillary energy as a function of the bond angle ϕ, we found a preferred side-by-side alignment for all pairs of ellipsoids irrespective of the

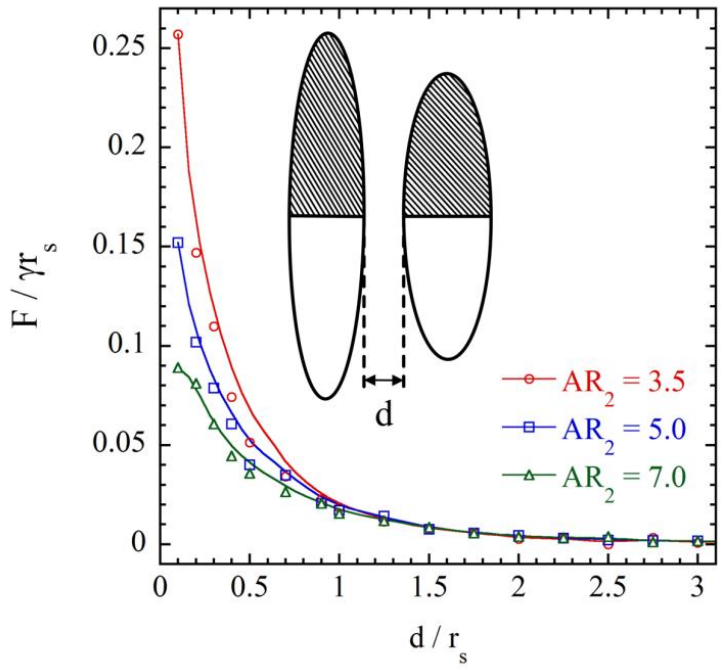

Figure 2.19 Capillary force between two dissimilar Janus ellipsoids as a function of the separation distance for $\beta = 30^{\circ}$, $AR_1 = 5$, and three different aspect ratios AR_2.

difference in aspect ratios. Additionally, the magnitude of the capillary torque inducing this optimum configuration is very close for all cases.

To compare the strength of interactions, we calculate the capillary force between particles in the preferred side-by-side alignment. Figure 2.19 depicts the variation of capillary force with surface-to-surface separation for pairs of dissimilar ellipsoids. All particles have equal surface area and amphiphilicity ($\beta = 30^{\circ}$), the first particle in each pair is characterized by $AR_1 = 5$, while the second particle adopts aspect ratios ranging from $AR_2 = 3.5$ to 7. This range is selected since Janus ellipsoids with an amphiphilicity characterized by $\beta = 30^{\circ}$ tend to deform the interface and induce capillary interactions for $AR > 3.3$, as shown in Figure 2.14(b). We note that the capillary force at close spacings reduces as the aspect ratio is increased. For more elongated ellipsoids, the overlapping menisci is stretched over a longer axis length, such that the change in surface area of the

interface is less sensitive to the variation of inter-particle separation. Consequently, the slope of energy curve and thus the capillary force is reduced as AR_2 increases. This indicates that for ellipsoidal particles with a constant surface area, one can tune the strength of capillary force in contact by modifying the particle's aspect ratio using *e.g.* the mechanical stretching method [77, 78].

In addition to shape, the size of the neighboring particles also influences the pair interaction. Basically, the magnitude and range of inter-particle forces can be enhanced upon increasing the size of particles with similar aspect ratio [66]. The reason is that increased particle size distorts the interface to a larger extent which thus enhances the tendency of two neighboring menisci to overlap.

2.3.4 Micromechanics of Janus Particle Chains

We showed in previous sections that prolate Janus ellipsoids induce hexapolar interface deformations that lead to capillary attractions between neighboring particles. A pair of ellipsoids tend to align in a side-by-side configuration in order to minimize the total surface energy. If several particles are trapped at the interface, the overlapping of menisci of similar sign in the side-by-side configuration results in the maximum possible reduction in interfacial energy, thus leading to the formation of particle chains. We can deduce the mechanical response of particle chains formed at liquid interfaces to external forces based on calculated pair interactions. The rigidity and rearrangement of colloidal monolayers under tensile forces and their mechanical response to bending moments are employed in calculating their rheological properties, such as the viscosity, yield stress and elastic modulus [79, 80].

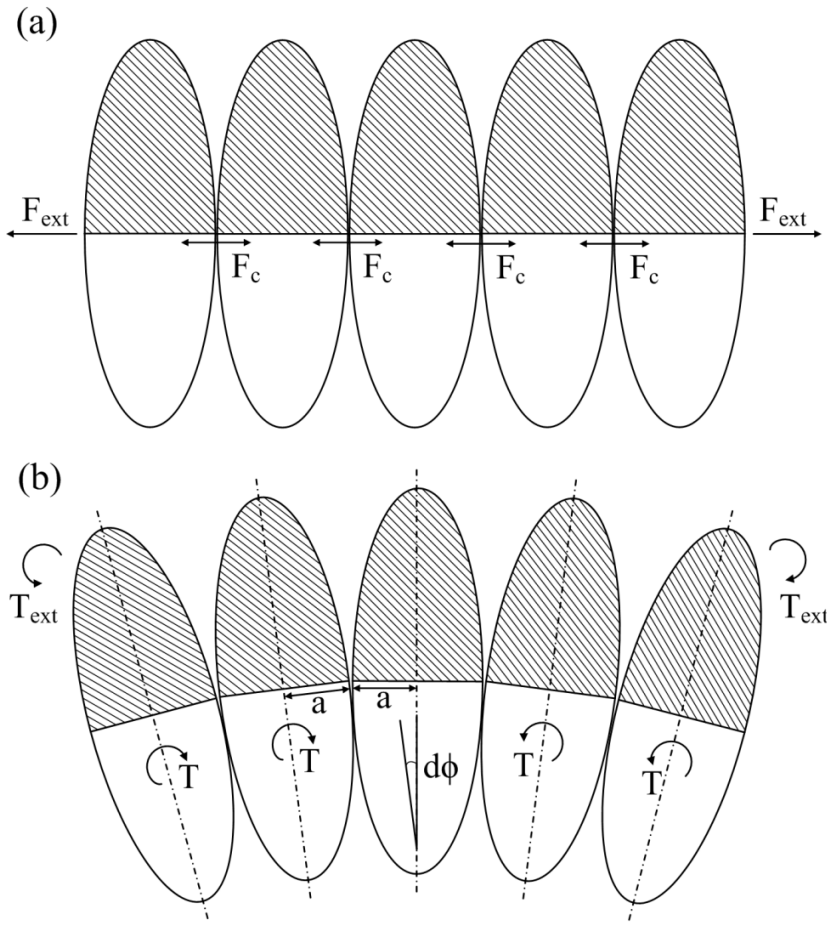

Figure 2.20 (a) A chain of side-by-side Janus ellipsoids under the application of a stretching force, (b) bending of the particle chain out of the equilibrium alignment due to an external torque.

Consider an initially straight chain of Janus ellipsoids pulled along its axis by an external force F_{ext}, as shown in Figure 2.20(a). The capillary force in contact can be calculated from the slope of energy curves as $F_c = (\partial E / \partial d)|_{d=0}$. The chain will support the external force without stretching if F_{ext} is less than the capillary force in contact. If $F_{ext} > F_c$, the particle chain will break apart since the inter-particle forces can not oppose the external field anymore. However, the position along the chain where breakage occurs cannot be predicted since the bonds between identical particles oppose the same capillary resistance and are subject to the same tensile force.

Particle chains can also be subject to bond-bending deformations, as shown in Figure 2.20(b). Chains of Janus ellipsoids are expected to behave as elastic elements in response to bending since the capillary interaction between pairs of ellipsoids is elastic for sufficiently small values of $d\phi$. The curvature ρ of a particle chain is defined as the ratio of the infinitesimal change in angle $d\phi$ to the corresponding length scale. The curvature in correspondence to each bond is therefore $\rho = d\phi/(2a)$, where $2a$ is the distance between the bonds for side-by-side ellipsoids in contact. The flexural rigidity κ of the chain is simply the proportionality constant between T and ρ, *i.e.* $T = \kappa \rho$. Since the dimensionless capillary torque $T/(\gamma r_s^2)$ varies linearly with $d\phi$ for small deviations, the flexural rigidity can be expressed as $\kappa = 2a\, \gamma r_s^2 D$, where D is the slope of the capillary torque curves near $\phi = 180^\circ$ as in Figure 2.18(b). For a micron-sized ellipsoidal particle with $a = 2.5\ \mu m$, $AR = 5$, and $\beta = 30^\circ$ at an oil-water interface with $\gamma = 50\ mN/m$, the flexural rigidity is calculated as $\kappa \sim 4.3\times10^5\ k_BT.\ \mu m$, which is converted to an elastic energy of $4.3\times10^3\ k_BT$ for chain of ellipsoids with a curvature of $(100\ \mu m)^{-1}$. Therefore, thermal fluctuations are unable to bend chains formed by Janus micro-ellipsoids. However, for less amphiphilic and smaller particles, the elastic energy is comparable with the thermal energy, and can bend the particle chains.

2.4 Summary: Equilibrium Configuration and Capillary Interactions

In this chapter, we performed quasi-static analysis to determine the equilibrium orientation and capillary-induced interactions between Janus particles adsorbed at planar liquid interfaces. Three main particle types were considered: Janus spheres, asymmetrically-Janus (patchy) spheres, and Janus ellipsoids. We numerically calculated

the interface shape around such particles and evaluated the capillary interactions that arise due to overlapping of distortions caused by neighboring particles. It was shown that Janus spheres with tilted orientations give rise to dipolar capillary interactions which can be of attractive or repulsive nature. Particles of opposite orientations are attracted by each other, and those oriented similarly undergo an in-plane rotation to create a capillary bridge resulting in similar attractive forces. On the other hand, if one of the particles is at the upright orientation, they will repel below an optimum separation distance which corresponds to minimum surface energy.

For spherical particles with asymmetric distribution of the two regions (single–patch design), it was shown that each region is mostly exposed to its favorite fluid phase at equilibrium, leading to a homogeneous contact line and a flat interface. For double–patch particles in which two spherical caps are patterned symmetrically on the particle, it was shown that the preferred orientation strongly depends on the wettability of two surface regions, as well as the size of the patch regions relative to the whole particle. Energy landscapes revealed the existence of two local minima, implying that the particles can be kinetically trapped in a metastable orientation under appropriate conditions. For any two given wettabilities, there is a transition patch size above which the particles flip from a parallel-patch orientation to normal-patch configuration, leading to quadrupolar capillary interactions between neighboring particles. We also demonstrated that incorporating the second patch on the opposite side of a spherical particle can improve the surface activity compared to a single-patch particle if the patch groups are relatively small and the contact angle of both materials are close to 90º.

The role of shape anisotropy on interface deformation and capillary-induced interactions was also investigated by considering Janus ellipsoids at a liquid interface. Janus ellipsoids induce a hexapolar interface shape, and the overlapping of such distortions for neighboring particles leads to long-ranged capillary interactions. They undergo a rotational relaxation within the interface plane to induce overlapping of menisci with similar signs, and align side-by-side to minimize the overall surface energy. The capillary force and the torque inducing the side-by-side configuration are enhanced upon increasing the particle amphiphilicity. Therefore, Janus ellipsoids exhibit stronger interactions compared to their homogeneous counterparts. These results can be used to predict the migration and oriented assembly of Janus particles of various geometrical and surface properties at liquid−fluid interfaces.

Chapter 3

Interfacial Thermal Motion of Janus Nanoparticles

The adsorption of nanometer-sized objects, including nanoparticles, dendrimers and proteins, at soft interfaces has recently attracted much scientific interest and is central to a number of emerging technologies. Self-assembly of nanoparticles at fluid interfaces has enabled the preparation of high quality two-dimensional crystals that can be employed for the fabrication of capsules, ultra-thin cross-linked membranes, and free-standing metal films [81-83]. While adsorption of nanoparticles with homogeneous surface properties to liquid interfaces is important in several processes, the advent of particles with anisotropic surface characteristics has opened up a variety of emerging applications. One example is the use of amphiphilic nanoparticles as building blocks for formation of various supracolloidal structures [3].

After investigating the equilibrium orientation and interaction of heterogeneous colloids of various geometry and surface chemistry, we turn our attention to their dynamic behavior at the nano-scale. Although molecular simulations to date have revealed many important aspects of the physical behavior of nanoparticles both in bulk fluids and at an interface, some aspects are still unclear. For Janus nanoparticles, their stability and desorption energy at a liquid interface have been recently investigated [84-87]. Contact angle measurements were also performed on silica nanoparticles with

uniform and asymmetric (Janus) distribution of functional groups [87]. However, their dynamics within the interface plane and their diffusion properties are still unclear. In this chapter, we aim to evaluate whether in addition to nanoparticle size, the surface chemistry also affects the translational/rotational diffusion of Janus particles at interfaces.

3.1 Problem Statement and Proposed Approach

We aim to extend our quasi-static analysis in the previous chapter on the equilibrium orientation and interaction forces between Janus particles to the dynamics of these particles adsorbed at the interface. We focus on nanoparticles where the Brownian motion mainly drives the particle and plan to evaluate the difference in interfacial dynamics of Janus particles with their homogeneous counterparts. In particular, we would like to consider the translational and rotational diffusion of Janus nanoparticles at a flat liquid interface using molecular simulations. The advantage of Molecular Dynamics (MD) over continuum approaches is that it can provide invaluable information by revealing details of flow structure around the particle at the interface and the specific interactions between the particle and each fluid species.

Fundamental Questions

We aim to answer the following questions concerning the interfacial thermal motion of Janus nanoparticles: 1) How is the particle diffusivity affected as compared to diffusion in a bulk fluid?, 2) In addition to particle size, does the surface chemistry also influence its in-plane translational diffusivity?, 3) How is the rotational diffusion influenced by particle amphiphilicity?, 4) What is the role of particle size and fluid properties on the interfacial thermal motion of nanoparticles?

In order to address these questions, we apply the following methodology. We create spherical clusters comprised of solid atoms and control the amphiphilicity by tuning the affinity of the atoms on each side of the particle with the two fluids. The thermal motion of the particle at the interface is monitored over sufficient realizations and simulation time. We will compare the fluid structure, the net force and torque acting on the particle, and the in-plane and out-of-plane displacement and rotation of the particle in order to reveal the role of amphiphilicity in tuning the interfacial dynamics. Since the effect of interfacial region on diffusive properties is expected to diminish upon increasing nanoparticle size, we aim to compare the bulk and interfacial diffusivity of nanoparticles with different sizes. The effect of fluid density and surface tension on the translational and rotational diffusivity will also be investigated.

3.2 Interfacial Diffusion of Janus Particles

A schematic representation of the geometry under consideration is shown in Figure 3.1. Each individual fluid phase is modeled as a monotonic Lennard-Jones fluid characterized with a well-defined phase diagram. The particle contains atoms of two different species, denoted as *J1* and *J2* and moves as a rigid body. The rotational evolution of the particle is monitored by tracking the angle between Janus boundary and the interface plane. The particle is initially placed at the interface with a specific orientation, while it can freely rotate or transfer to a bulk fluid due to thermal fluctuations. We monitor the particle position and orientation as well as its linear and angular velocity over time through measuring the applied forces and torques.

Molecular Dynamics simulations are carried out using the shifted-force Lennard-Jones (LJ) potential given as

$$U(r_{ij}) = \begin{cases} 4\varepsilon\left[\left(\frac{\sigma}{r_{ij}}\right)^{12} - A\left(\frac{\sigma}{r_{ij}}\right)^{6}\right] - U(r_c) - \left.\frac{dU}{dr}\right|_{r_c}(r - r_c) & r \le r_c \\ 0 & r > r_c \end{cases} \tag{3.1}$$

in which r_{ij} is the separation distance between atoms i and j, σ is roughly the size of the repulsive core, ε is the depth of the potential well, and the potential cutoff is defined as $r_c = 2.5\sigma$. The coefficient A controls the attraction between atoms of different atomic species in the system, which in turn defines the wetting properties. The interaction coefficient for atoms in the same fluid and with the wall are set to $A_{ii} = 1$, while atoms of the two different fluids interact with $A_{ij} = 0.5$ in order to ascertain the immiscibility of the fluids. For the particle-fluid interaction, this parameter can be correlated to the contact angle θ at any solid–liquid interface approximately by $cos\theta = -1 + 2A$ [88].

Similar to the case of Janus spheres in chapter 2, we consider particles with two

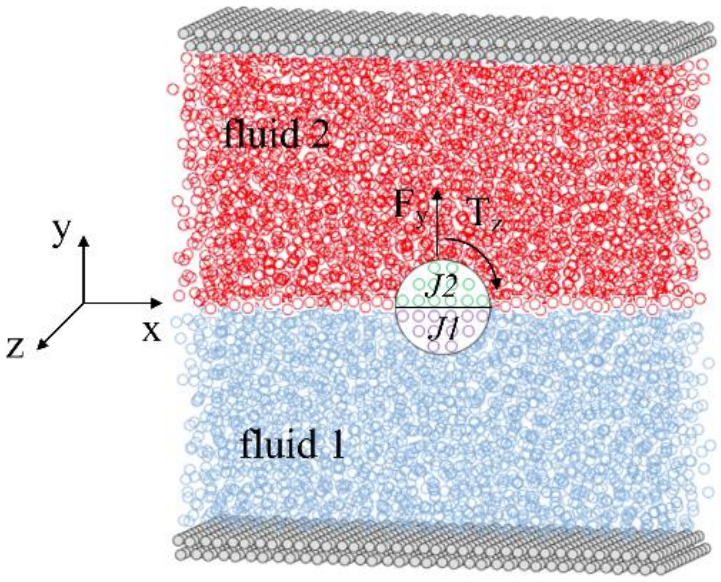

Figure 3.1 Schematic representation of the MD simulation box containing a Janus nanoparticle at the interface between two immiscible fluids.

regions of opposite wettability (*i.e.*, apolar and polar), represented by $\theta_a = 90^\circ + \beta/2$ and $\theta_p = 90^\circ - \beta/2$, with the parameter β characterizing the degree of amphiphilicity. The size of the simulation box is set to $L_x \times L_y \times L_z = 32\sigma \times 45\sigma \times 32\sigma$, and a size-independency test has been performed to ensure that the fluid properties are not affected by layering effects near the walls. Periodic boundary conditions are imposed in the directions parallel to the interface plane in order to simulate a large system and avoid wall effects [89]. The particle radius is set in the range of $R/\sigma = 3–6$ by cropping regions of different size from the initial cubic lattice.

The simulation starts with an equilibration process from the initial solid-like FCC lattice, followed by a post-equilibration stage for data collection. The positioning of different atomic species, inter-atomic forces, and kinetic and potential energies are measured over a sufficiently long period. The calculations are done in the canonical (NVT) ensemble, where the temperature is fixed using the Nosé-Hoover thermostat [90]. The net force and torque on the particle are computed by adding up the individual interactions between its atoms and the neighboring fluid atoms, and the motion is governed by Newton's and Euler's equations. We use quaternion parameters to describe the particle orientation, in order to avoid the problem of divergence in the rotational equations of motion [89]. A Verlet list is built at frequent time-steps in order to minimize the calculation of interactions beyond the cutoff radius. Integrating equations of motion is done via a five-value predictor-corrector algorithm. The calculations are performed in dimensionless variables with the scaling parameters being σ (length scale), ε (energy scale), and m (mass of the fluid atoms), with the relevant time scale of $\tau = \sqrt{m\sigma^2/\varepsilon}$.

Typical numerical values are $\sigma = 0.3\,nm$, $\tau = 2\,ps$, and $\varepsilon = 120k_B$, where k_B is Boltzmann constant [91].

The translational diffusivity can be characterized using the mean-squared displacement

$$D_t = \frac{1}{6}\frac{d}{dt}\langle \Delta \boldsymbol{r}_p(t)^2 \rangle = \frac{1}{6}\frac{d}{dt}\langle \left(\boldsymbol{r}_p(t) - \boldsymbol{r}_p(0)\right)^2 \rangle \tag{3.2}$$

where $\boldsymbol{r}_p(t)$ is the center of mass position of the particle at time t and the angle brackets denote averaging over realizations with different initial fluid velocity profiles. On the other hand, the rotational motion can be quantified in terms of the angular velocity correlation function

$$C_\omega(t) = \langle \boldsymbol{\omega}(t).\boldsymbol{\omega}(0) \rangle \tag{3.3}$$

where $\boldsymbol{\omega}(t)$ is the angular velocity vector at time t and the ensemble averaging is performed over different realizations. The rotational diffusion coefficient can be calculated by integrating the correlation function

$$D_r = \frac{k_B T}{I}\int_0^\infty \frac{C_\omega(t)}{C_\omega(t=0)}\,dt \tag{3.4}$$

where I is the mass moment of inertia of the particle which is determined by incorporating the moment of each atom within the cluster about the center of mass. At a liquid interface, however, the nanoparticle diffusion becomes anisotropic as it is strongly bound to the interface plane. It is thus useful to evaluate the motion of the nanoparticle

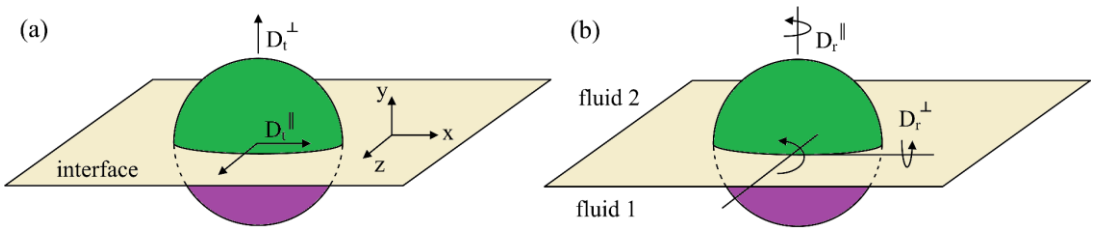

Figure 3.2 Schematic view of the in-plane and out-of-plane decomposition of (a) translational and, (b) rotational diffusion of a Janus particle at a liquid interface.

parallel and normal to the interface, as shown schematically in Figure 3.2(a). The diffusivity parallel to the interface and that in normal direction (y) can be determined as

$$D_t^{\parallel}=\frac{1}{4dt}\langle\Delta \boldsymbol{r}_p^{\parallel}(t)^2\rangle=\frac{1}{4dt}\langle(x(t)-x(0))^2+(z(t)-z(0))^2\rangle$$
$$D_t^{\perp}=\frac{1}{2dt}\langle\Delta \boldsymbol{r}_p^{\perp}(t)^2\rangle=\frac{1}{2dt}\langle(y(t)-y(0))^2\rangle \quad (3.5)$$

We will thus compare the in-plane translational diffusion of nanoparticles with different surface properties since the out-of-plane motion will not be diffusive with very limited fluctuations as a result of the strong particle attachment to the interface.

For the rotation, homogeneous nanoparticles diffuse isotropically around the three coordinate axes, while Janus ones can only rotate around normal to the interface as the contact line becomes locked at the Janus boundary. The nanoparticle rotation can be decomposed into in-plane (around y axis) and out-of-plane (around x,z axes) as

$$D_r^{\parallel}=\frac{k_BT}{I}\int_0^{\infty}\frac{C_{\omega}^{n}(t)}{C_{\omega}^{n}(t=0)}=\frac{k_BT}{I}\int_0^{\infty}\frac{\langle\omega_y(t).\omega_y(0)\rangle}{\langle\omega_y(0).\omega_y(0)\rangle}$$
$$D_r^{\perp}=\frac{k_BT}{I}\int_0^{\infty}\frac{C_{\omega}^{p}(t)}{C_{\omega}^{p}(t=0)}=\frac{k_BT}{I}\int_0^{\infty}\frac{\langle\omega_x(t).\omega_x(0)+\omega_z(t).\omega_z(0)\rangle}{\langle\omega_x(0).\omega_x(0)+\omega_z(0).\omega_z(0)\rangle} \quad (3.6)$$

This is demonstrated schematically in Figure 3.2(b). We will thus compare the in-plane component of the rotational diffusion of nanoparticles with different surface properties since $D_r^{\perp}$ does not demonstrate a diffusive behavior for Janus particles due to stronger binding of each hemisphere to its favorite fluid.

3.3 Simulation Results

In the first step, we evaluate the average fluid properties in the absence of nanoparticles. The fluid density, diffusivity, and the interfacial tension between the two phases, are calculated and compared with the available simulation results and

correlations. Then, the particle diffusivity calculations are validated by modeling the diffusion of homogeneous nanoparticles in bulk fluid over a range of particle size, and comparing the calculated translational and rotational diffusivities with theoretical values based on Stokes-Einstein(-Debye) theory [92]. Finally, we examine the diffusion of Janus particles at a liquid interface and explain the change in diffusivity based on the fluid layering. The effects of particle size, fluid density, and surface tension on translational and rotational diffusivity are also investigated.

3.3.1 Fluid Properties Calculation

The average fluid properties are evaluated in a simulation box containing only two fluid species. The fluid density is measured by decomposing the domain into several layers parallel to the interface plane and averaging the number of fluid atoms per unit volume over 10^4 time steps after equilibration. Figure 3.3 shows the density profile for each fluid and the total density as a function of the position relative to the interface. The immiscibility of the two fluids is easily confirmed by noting that the number density of each fluid species rapidly approaches zero in the opposite half of the box. Near the interface, there is a total density gap caused by the immiscibility of the two fluids. Such density gap has also been observed in other molecular simulations of fluid interfaces [93], and is usually not captured in continuum models [94]. Away from the interface, the total density approaches the prescribed value of $\rho = 0.8/\sigma^3$. The calculated average density is within 1.5% of this assigned value. The interfacial width can be estimated from the density profiles of individual components as the distance between the points at which the density of each fluid drops from 90% to 10% of its bulk value [95]. This yields an

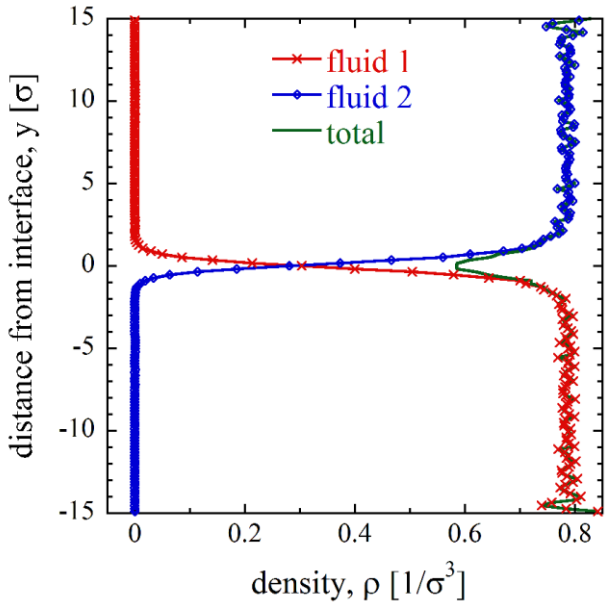

Figure 3.3 Density profiles of the two fluids as a function of normal distance from the interface plane.

average width of $w \approx 2.5\sigma$, which translates into *7.5 Å* in metric units and is typical for simple fluid interfaces.

The diffusivity of the fluid atoms is determined by calculating the mean-squared displacement, similar to Eq. (3.2) for a particle. The averaging is performed over all fluid atoms sufficiently far from the walls. Using the slope of the mean-squared displacement curve versus time, the diffusion coefficient was calculated as $D = 0.069\,\sigma^2/\tau$ for the above type of fluid, which is within 1.5% of the value predicted by the available correlations [96].

To quantify the degree of immiscibility between the two fluids, the interfacial tension calculations are carried out. This quantity is related to the difference between the normal and transverse components of the stress tensor integrated over the longitudinal (y) direction

$$\gamma = \int_{-L_y/2}^{L_y/2} [P_N(y) - P_T(y)]\, dy. \tag{3.7}$$

We perform the interfacial tension calculation in a system with similar size but replacing the limiting walls with periodic boundary conditions in y direction. Therefore, two interfaces will exist in the simulated system and the interfacial tension is translated into

$$\gamma = \frac{1}{2}\int_{-L_y/2}^{L_y/2}\left[P_{yy} - 1/2(P_{xx} + P_{zz})\right] dy. \tag{3.8}$$

In the absence of any external constraint, the pressure tensor is expected to be diagonal. Due to the symmetry in our simulation box, two of the components are equal: $P_{xx} = P_{zz}$. Hydrostatic equilibrium imposes the condition that the normal pressure P_{yy} is constant everywhere, while the transverse pressure will differ in the interface region. Using the Kirkwood-Buff formulation of the tangential and normal components of the pressure tensor, the interfacial tension can be written as [93]

$$\gamma = \frac{1}{4A}\langle\sum_{i<j}\left(1 - \frac{3y_{ij}^2}{r_{ij}^2}\right) r_{ij}u'(r_{ij})\rangle, \tag{3.9}$$

where A is the interfacial area ($L_x \times L_z$), r_{ij} is the distance between two atoms i,j, y_{ij} is their distance in y direction, and $u'(r_{ij})$ is the spatial derivative of the potential function: $\partial u(r_{ij})/\partial r_{ij}$. To calculate the interfacial tension, we sum over all interacting pairs after an initial equilibration period and calculate γ by averaging over time and different realizations in Eq. (3.9) assuming ergodicity [89]. We obtained $\gamma = 1.47\ \varepsilon/\sigma^2$, which is within 2% of the values reported in similar MD studies [93].

3.3.2 Particle Diffusion in Bulk Fluid

In order to validate the molecular simulations with Stokes-Einstein theory, we simulate the diffusion of nanoparticles in bulk by assigning attraction coefficients $A_{12} = A_{21} = 1.0$ between the two fluid species. Homogeneous solid particles with sizes in the

range of $3 \leq R/\sigma \leq 6$ are initially placed at the center of the simulation box, and the position, orientation, as well as linear and angular velocities are tracked in multiple realizations. According to Stokes-Einstein theory, the translational diffusion coefficient

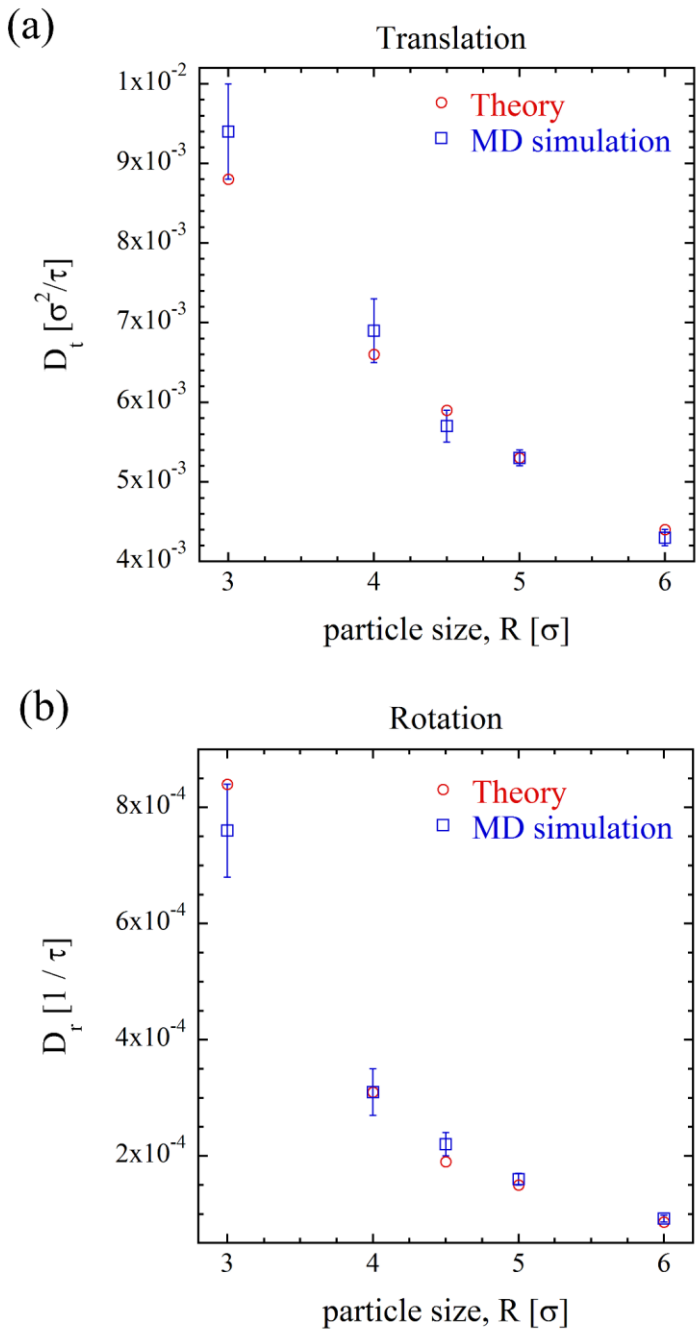

Figure 3.4 (a) Translational and, (b) rotational diffusion coefficients for homogeneous nanoparticles of different sizes in a bulk Lennard-Jones fluid and the theoretical values found from Stokes-Einstein(-Debye) relations.

of a particle with radius R in a bulk fluid of viscosity η and no-slip boundary conditions is given by

$$D_t = \frac{k_B T}{6\pi R\eta}. \tag{3.10}$$

Similarly, the rotational diffusion coefficient of the particle is given by the Stokes-Einstein-Debye relation

$$D_r = \frac{k_B T}{8\pi R^3 \eta}. \tag{3.11}$$

For Lennard-Jones fluids with the assigned temperature and density, the viscosity is determined from the available tables as $\eta \approx 2.0\, m\sigma^{-1}\tau^{-1}$ and used in Eqs. (3.10, 3.11) [97]. The translational and rotational diffusion coefficients for nanoparticles of different sizes are plotted in Figure 3.4 along with their theoretical values. We observe that the simulated values are in good agreement with the theory, showing typically <6% deviation. The theoretical values lie within the statistical uncertainty of simulated results, thus validating the molecular simulations. The deviation can be due to the inaccuracy in the estimated viscosity which was obtained by linear interpolation of tabulated values, as well as the round-off error in integrating velocity correlation functions. In addition, the simulated particles are not smooth spheres and there is some ambiguity in the definition of particle radius, as reported in similar molecular simulations [91, 98, 99].

3.3.3 Diffusion of Janus Particles at Liquid Interfaces

When the particle is adsorbed at a liquid–liquid interface, the diffusion becomes anisotropic. The detachment energy required to remove the particle from an interface [100] is found to be much larger than the thermal energy k_BT for the investigated size range, such that the motion normal to the interface is expected to be significantly smaller

than the in-plane diffusion. Furthermore, the contact line coincides with the Janus boundary, thus allowing particle rotation only within the interface plane. Figure 3.5(a) shows the mean-squared displacements for a Janus nanoparticle with $R = 3.0\ \sigma$ and an amphiphilicity characterized by $\beta = 120^{\circ}$ over the period $0 \leq t/\tau \leq 200$. We clearly note that the in-plane motion shows a linear diffusive trend, while the long time motion normal to the interface is non-diffusive. Our simulations indicate that the attachment

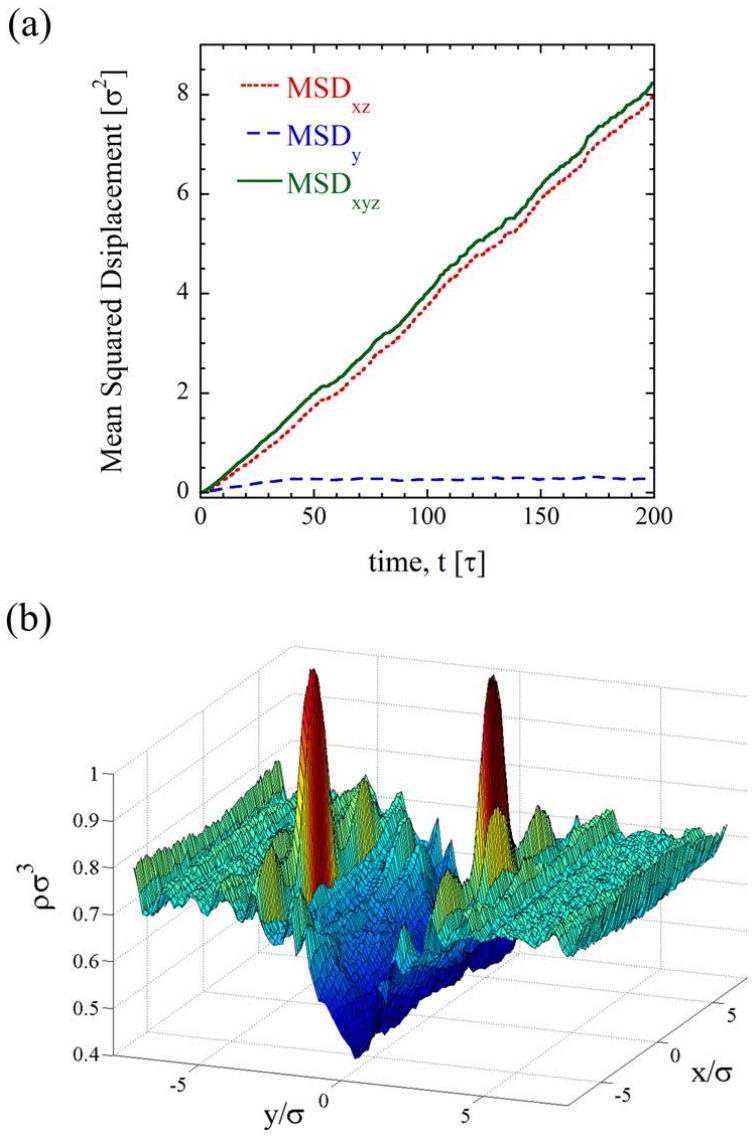

Figure 3.5 (a) Mean-Squared Displacements for a Janus nanoparticle with size R = 3.0σ and amphiphilicity of β = 120˚ adsorbed at a liquid interface, (b) surface plot of fluid density around the particle.

becomes stronger as the particle amphiphilicity increases, due to the increased affinity between each hemisphere and its surrounding fluid.

Moreover, the fluid structure around the nanoparticle becomes anisotropic upon adsorption to the interface. An isometric view of the surface plot of fluid density variation in *x*-*y* plane is depicted in Figure 3.5(b). Firstly, a depletion region is clearly detected between the two fluid components near $y = 0$ (in accordance with Figure 3.3). Note that the size of the nanoparticles investigated here is comparable to the width of the depletion region at the interface. More importantly, we observe a structured fluid with distinct peaks and dips close to the particle surface. The highest peaks occur at $y \approx \pm 3.5\ \sigma$, while the peak strength gradually declines when moving away from the center of the box in *x*,*y* directions as the distance from the nanoparticle surface increases. The nanoparticle thus perturbs the fluid as reflected in the high-density layers near the surface. Such layering is basically similar to the case of homogeneous nanoparticles at a liquid interface [101].

In order to evaluate the effect of surface wettability on the diffusivity of nanoparticles, molecular simulations are performed on particles with different amphiphilicity as characterized by $\beta = 0\text{-}180^{\circ}$. Figure 3.6(a) shows the in-plane translational diffusivity $D_t^{\parallel}$ for nanoparticles of three different sizes as the amphiphilicity is varied. The fluids have equal density of $\rho = 0.8\ \sigma^{-3}$, a viscosity of $\eta = 2.0\ m.\sigma^{-1}.\tau^{-1}$, and an interfacial tension of $\gamma = 1.47\ \varepsilon.\sigma^{-2}$. For all investigated particle sizes, we observe a reduction in diffusion coefficients upon increasing the amphiphilicity. The difference is more apparent for larger particles as the relative uncertainty becomes smaller. This suggests that Janus nanoparticles diffuse more slowly at a liquid interface compared to

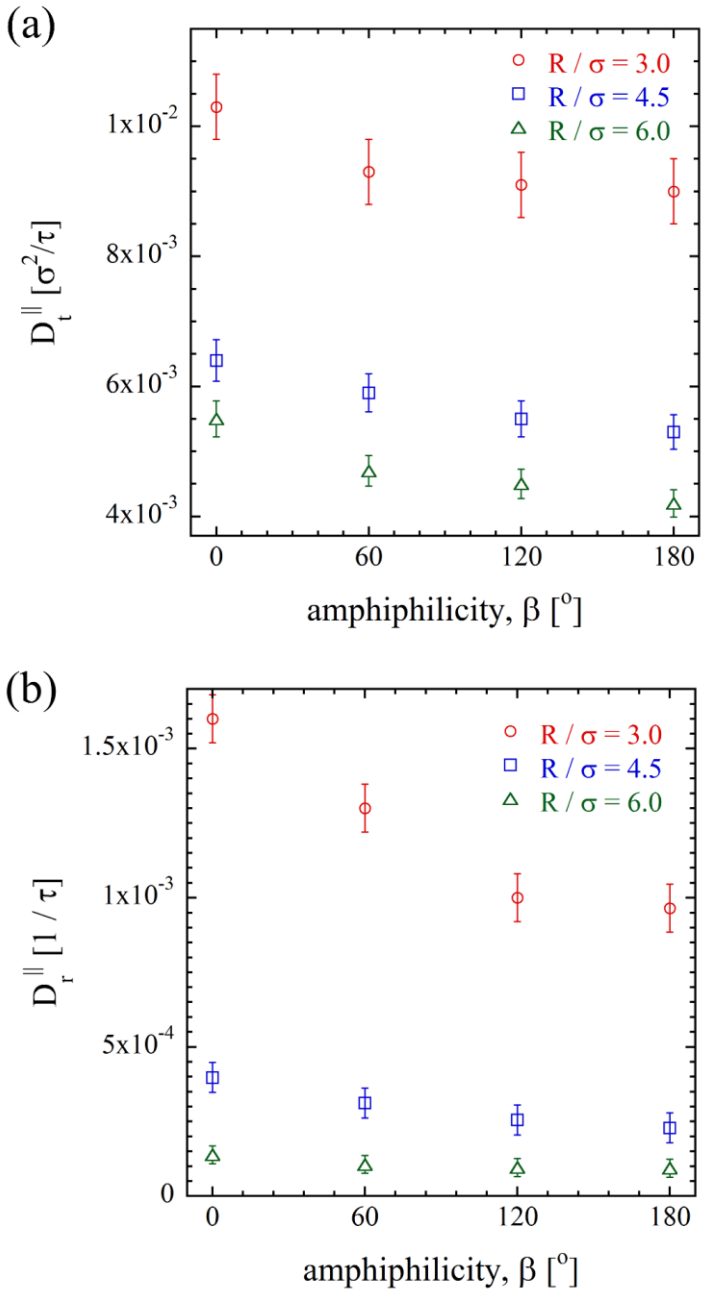

Figure 3.6 (a) Translational and, (b) rotational diffusion coefficients for Janus nanoparticles of different size and amphiphilicity at the interface between two immiscible fluids.

homogeneous particles of similar size. Moreover, we observe that the diffusion reduces by increasing the nanoparticle size at each β, but the rate of decay is found to be faster than the R^{-1} proportionality in Stokes-Einstein theory for particle diffusion in a bulk fluid [102]. A similar trend is observed in case of the in-plane rotational diffusion $D_r^{\parallel}$ as shown

in Figure 3.6(b), with the reduction rate being generally faster than R^{-3} at each amphiphilicity.

The above results suggest that in addition to particle size, the surface chemistry also influences the interfacial diffusivity of nanoparticles. In order to reveal the source of deviation in diffusivity of particles of different surface properties, we look at the molecular structure of the fluid surrounding these nanoparticles. The radial distribution function *g(r)* for Janus nanoparticles of different amphiphilicity is shown in Figure 3.7. We observe that in all cases, the fluid is highly structured around the particle, with a number of peaks spaced by $\sim 1\sigma$. More importantly, the fluid layering becomes more pronounced as β increases. This microscopic observation indicates that the fluid structures more uniformly into layers around amphiphilic Janus particles compared to a homogeneous one with the same size but 90° contact angle.

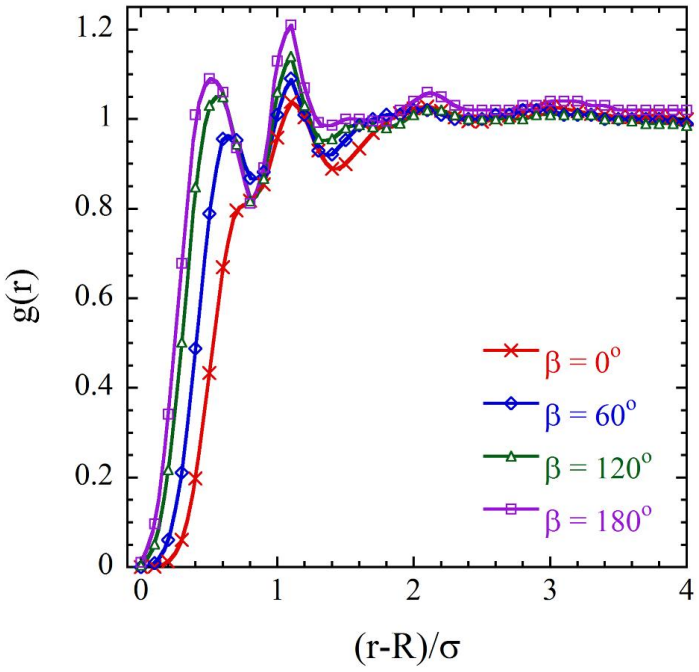

Figure 3.7 Radial distribution function for the fluid surrounding nanoparticles with R = 3.0σ and different amphiphilicity at a liquid interface.

As the amphiphilicity increases, the wetting of each hemisphere with its surrounding fluid is enhanced. Earlier molecular simulations for water near a solid wall suggest that water molecules adjacent to more hydrophobic walls are more randomly distributed and show a weaker ordering [103]. We observe a similar behavior for amphiphilic spheres, with a stronger ordering as each side is more preferably wetted by the surrounding fluid. We expect such increase in layering to induce a larger resistance against particle motion as the adsorption layer of fluid atoms around the particle will contain a higher concentration of fluid atoms. Consequently, nanoparticles with higher amphiphilicity experience a slower diffusion within the interface plane.

In addition, the fluctuation of the contact line around the Janus boundary and the exposure of solid atoms to unfavorable fluid species may also contribute to a reduction in diffusivity and thus slightly couple particle translation to its rotation. To evaluate this hypothesis, we repeated our simulations but with the added constraint of fixed upright orientation for Janus nanoparticles of $R = 3.0\sigma$. The result demonstrates that the decrease in the in-plane translational diffusion coefficients with amphiphilicity reduces, while the fluid structure is almost unaffected. For instance, the decrease in $D_t^{\parallel}$ between particles with $\beta = 0^\circ$ and 180° is reduced from 14% to ~8% upon fixing the orientation of the particles. Therefore, we conclude that the in-plane diffusion slows down with increased amphiphilicity due to both stronger fluid layering as well as finite fluctuations around the upright orientation.

For the rotational diffusion, the slower in-plane rotation of more amphiphilic nanoparticles can also be attributed to the increased resistance of the adsorbed fluid layer.

Therefore, particles of similar sizes but different surface properties experience different translational and rotational diffusion at a liquid interface.

3.3.4 Effect of Fluid Properties on Interfacial Diffusion

We demonstrated in previous section that the fluid layering around nanoparticles at the interface is enhanced for increasing amphiphilicity. As a consequence, the adsorbed fluid layer becomes denser, thus inducing a larger resistance against particle motion. However, the fluid structure near a solid surface generally depends on the bulk density, with denser fluids being more structured [103]. Therefore, it is important to evaluate the effect of fluid density on layering around nanoparticles of different surface wettability. To do this, nanoparticles of $R = 3.0\ \sigma$ and different amphiphilicities characterized by $\beta = 0–180^\circ$ are considered, while the density of surrounding fluids is altered from the original value of $\rho = 0.8/\sigma^3$. Figure 3.8(a) shows the radial distribution function around nanoparticles for the case of $\rho = 0.7/\sigma^3$. We observe a trend similar to that of the denser fluid studied so far but with the first peak being considerably lower. This indicates that a lower-density fluid is generally less structured around the nanoparticles as a smaller number of fluid atoms can form an adsorption layer adjacent to the solid surface. As the fluid density is increased to $0.9/\sigma^3$, the first peak grows higher and the fluid becomes more structured at close vicinity of the particle as shown in Figure 3.8(b). In addition, the peaks shift to the left and their spacing is reduced, suggesting more concentrated fluid atoms. For both fluid densities, we observe that the fluid ordering is enhanced as the amphiphilicity increases. This effect is more pronounced at lower densities and becomes less visible for higher-density fluids.

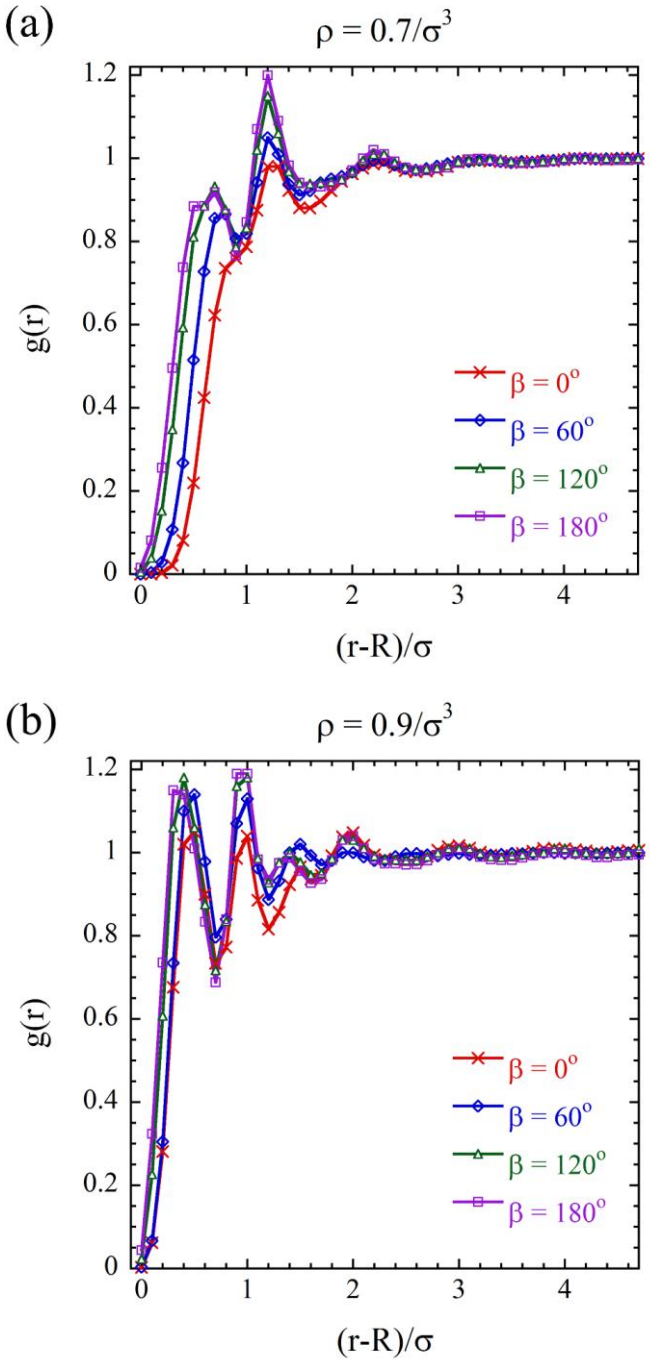

Figure 3.8 Radial distribution function for fluids with two different densities surrounding nanoparticles with R = 3.0σ at a liquid interface: (a) $\rho\sigma^3 = 0.7$, (b) $\rho\sigma^3 = 0.9$.

In addition, we evaluate the translational and rotational diffusion coefficients of nanoparticles at the interface between these fluids. The calculated values for $D_t^{\parallel}$ are

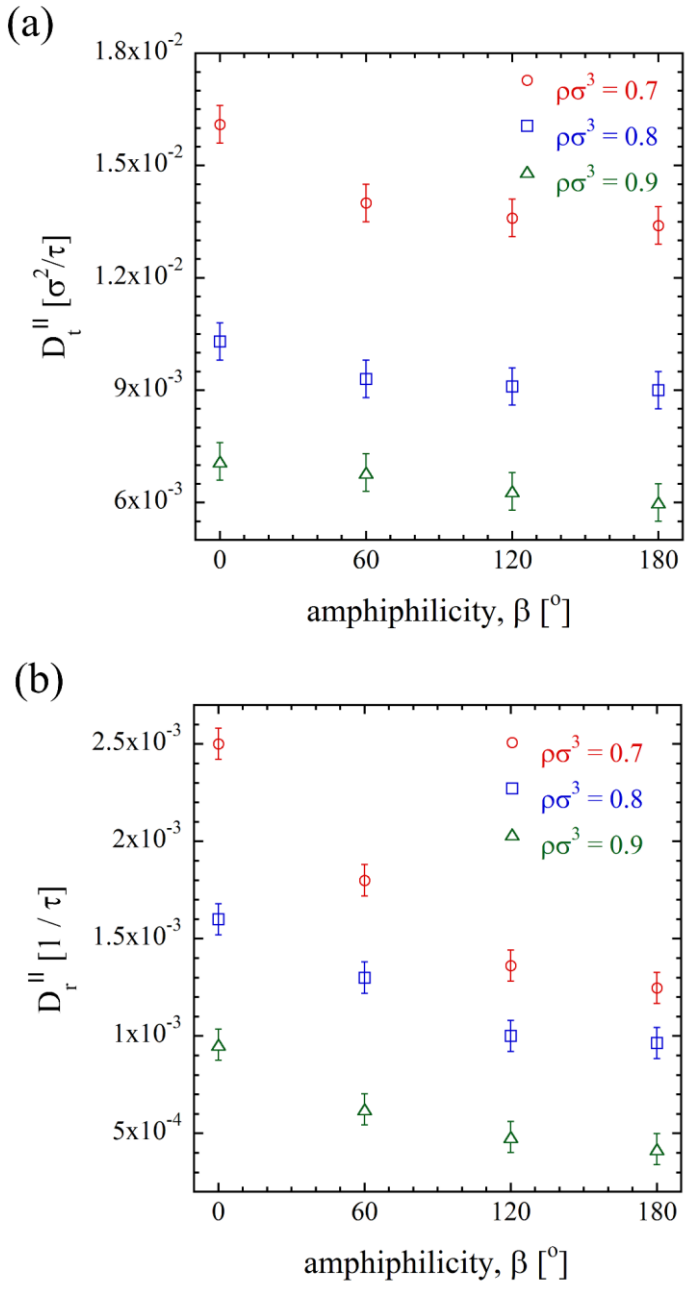

Figure 3.9 (a) Translational, (b) rotational diffusion coefficients for nanoparticles of size R = 3σ and different amphiphilicity diffusing at the interface between fluids with various density.

plotted in Figure 3.9(a). The results indicate that the diffusivity increases as the fluid density is reduced. For Lennard-Jones fluids with the assigned temperature of $T = 1.0\ \varepsilon/k_B$ and a density of $\rho\sigma^3 = 0.7, 0.8, 0.9$, the viscosity is measured as $\eta = 1.1, 2.0, 4.1\ m.\sigma^{-}$

$^{1}.\tau^{-1}$, respectively [97]. Therefore, the enhanced diffusivity can be attributed to the reduction in the effective viscosity and drag force acting on the particle.

Equally important is understanding the role of wettability on interfacial diffusion. Figure 3.9(a) suggests that for a Janus particle with $\beta = 60^{\circ}$ compared to a homogeneous particle ($\beta = 0^{\circ}$), the diffusivity reduces by *~13, 10, 4%* at the interface between fluids with $\rho\sigma^{3}$ = *0.7, 0.8, 0.9*, respectively. Therefore, Janus nanoparticles of moderate amphiphilicity will practically diffuse similar to their homogeneous counterparts at the interface between two denser fluids. As shown in Figure 3.8, denser fluids are generally more structured, so that the effect of nanoparticle surface wettability on fluid layering becomes less pronounced. On the other hand, the fluid layering around particles in lower density fluids is significantly affected by surface properties.

The fluid density and layering effects also influence the rotational thermal motion of nanoparticles at the interface. The in-plane rotational diffusivities for the above bulk densities are shown in Figure 3.9(b), suggesting a trend similar to the translational diffusion. Particle rotation is reduced in denser fluids since the higher viscosity results in lager resistance against particle rotation. In addition, since the denser fluid has a stronger structure, this results in a more concentrated adsorption layer, which may be interpreted as an increased effective nanoparticle size and thus a slower translational and rotational diffusion.

The other parameter that affects the interfacial dynamics of Janus particles is the surface tension between the two fluid phases. We control the immiscibility of the two Lennard-Jones fluids through the attraction coefficient A_{12}, which was set to *0.5* in all above cases. On the other hand, the attraction coefficient between two atoms of the same

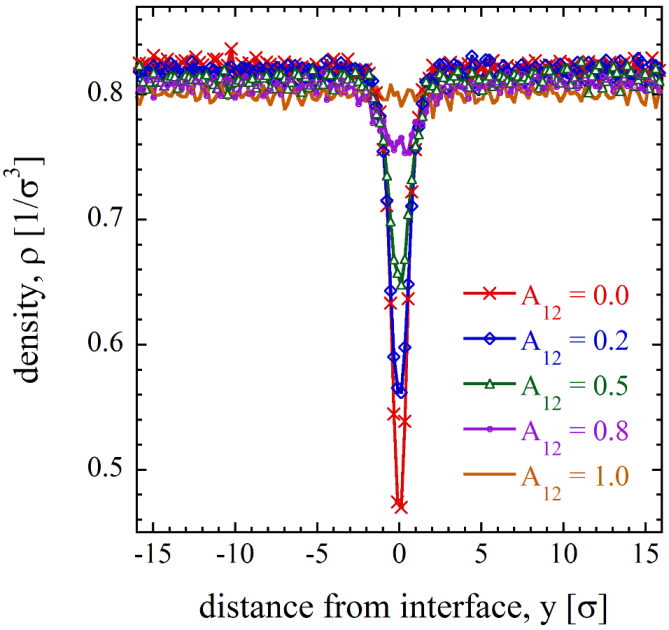

Figure 3.10 Density profiles for two immiscible fluids as a function of distance from the interface for different attraction coefficients A_{12} between the two fluids.

fluid were set to $A_{11} = A_{22} = 1.0$. Increasing A_{12} above 0.5 indicates a stronger attraction between the fluids yielding a lower interfacial tension. The change in interfacial tension will modify the density gap at the interface region and consequently the resistance against particle translation/rotation.

To evaluate this, we simulate the motion of particles of size $R = 3.0\ \sigma$ and amphiphilicities $0^o \leq \beta \leq 180^\circ$ at the interface between two fluids with density $\rho = 0.8/\sigma^3$, while varying the attraction coefficient between the two fluid species. In each case, the interfacial tension is estimated using Eq. (3.9). As the attraction coefficient is reduced towards zero, the fluids become more immiscible, leading to an increased surface tension.

As shown in Figure 3.10, the depletion region near the interface grows deeper as the attraction between the two species becomes weaker. For $A_{12} = 0$, the minimum density point is $\rho\sigma^3 \approx 0.47$. The increased repulsion between the two species clearly results in a smaller concentration of the fluid atoms near the interface.

The translational and rotational diffusion coefficients for nanoparticles of different amphiphilicities are shown in Figure 3.11, revealing a slight increase in both as the surface tension increases. However, a much smaller variation in diffusion coefficients is detected compared to the effect of bulk density. As we change the surface tension,the

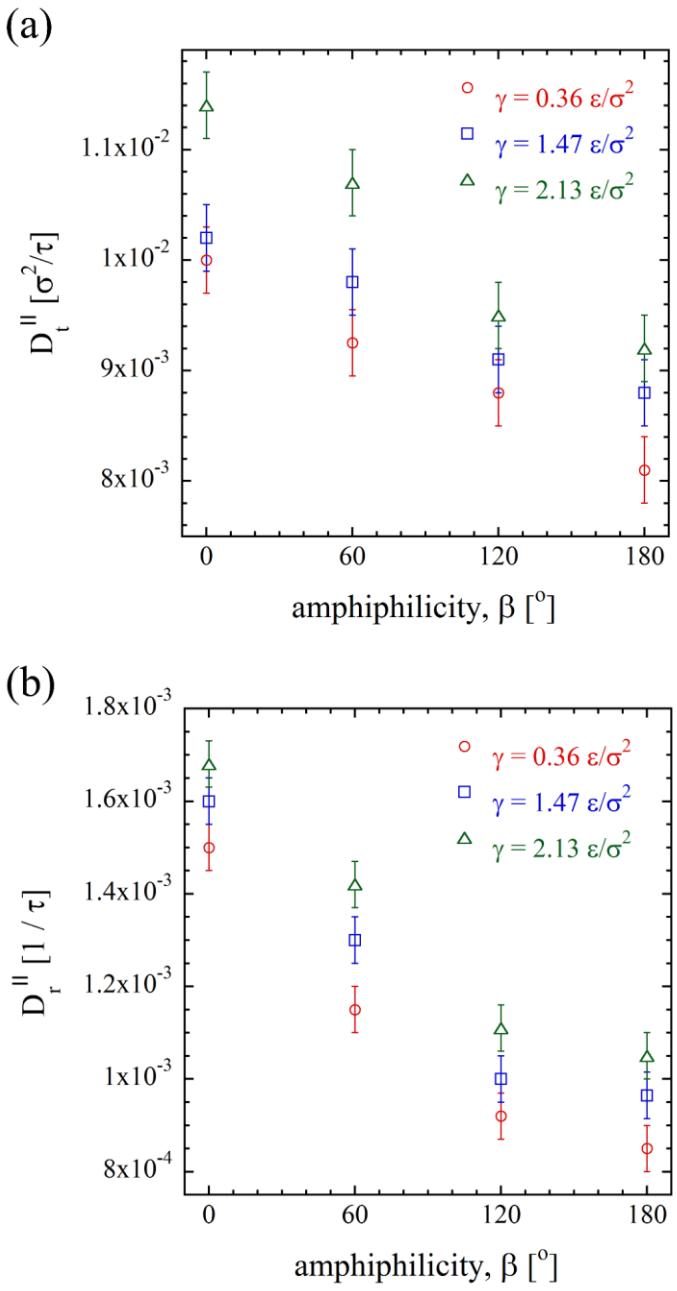

Figure 3.11 (a) Translational, (b) rotational diffusion coefficients for NPs of size R = 3σ and different amphiphilicity diffusing at liquid interfaces with various surface tensions.

diffusivities $D_t^{\parallel}$ and $D_r^{\parallel}$ deviate by ~11%, 9% on average. The change in diffusivity with surface tension can be attributed to deepening the density gap at the interface, which results in a slight reduction in effective viscosity and the drag force acting on the particle. The effect is much weaker than tuning the bulk fluid density though, since it only affects a small region with a width of $w \approx 2.5\sigma$ around nanoparticles. This effect diminishes even further for larger nanoparticles since the interfacial width becomes smaller relative to the particle size.

3.4 Summary: Interfacial Thermal Motion of Janus Particles

In this chapter, we studied the diffusion of Janus particles at fluid interfaces using molecular dynamics simulations. Janus particles were modeled as spherical clusters comprised of two sides with different affinity to fluid phases, with the attraction coefficient for each solid/liquid pair being related to the wettability. Interestingly, we found that the diffusion is not only a function of particle size, but also depends on its surface chemistry. It was shown that both the in-plane translational and rotational diffusivity reduce upon increasing the amphiphilicity. By investigating the radial distribution function, we found that the fluid is more structured around Janus articles compared to their homogeneous counterparts. A larger number of fluid atoms contribute to the adsorption layer accompanying the particle, thus increasing the resistance against motion due to an increased effective particle size.

The effects of nanoparticle size, fluid density, and surface tension on the interfacial diffusivity were also investigated. Both the in-plane translational and rotational diffusivities become slower with increasing particle size, but with decay rates being faster

than those in a bulk fluid. Investigating the diffusion in fluids with different density revealed that the reduction in diffusion coefficient of Janus nanoparticles upon increasing the amphiphilicity can only be considerable in case of lower-density fluids, while the effect diminishes with increasing density. Furthermore, particles adsorbed at an interface with higher surface tension exhibit slightly slower diffusion. These results provide fundamental insight into the dynamics of anisotropic nanoparticles at liquid interfaces.

Chapter 4

Interfacial Hydrodynamics of Janus Particles

In the previous chapter, we investigated the thermal motion of Janus particles at a stationary flat interface. However, the adsorption phenomena at liquid interfaces may involve hydrodynamic flows. For instance, long-term stability of Pickering emulsions is determined by the response of particles to bubble-bubble coalescence caused by moving liquid interfaces [104]. On the other hand, viscous flows are considered as a mechanism to direct/tune the assembly of particles at fluid interfaces [105]. Shear rate, particle size and shape, degree of amphiphilicity, particle volume fraction, and polydispersity are factors that influence flow-induced ordering, resulting in a rich physical behavior. We are interested in exploring these effects and evaluating how a cluster of Janus particles responds to hydrodynamic flows at the interface.

4.1 Objectives and Simulation Approach

In this chapter, we aim to extend our analysis on thermal motion of Janus particles at a stationary interface to the case where hydrodynamic flows can influence particle motion and orientation. A linear shear flow is considered at the interface as a standard type of flow for such studies. We start by exploring the rotational dynamics experienced by an

isolated particle at a sheared interface, and then evaluate the interactions and possible assembly in a cluster of such particles.

Fundamental Questions

The general goal of this part is to understand details of the response of isolated Janus particles adsorbed at liquid–fluid interfaces to imposed shear flows. We aim to answer the following fundamental questions: 1) Can the shear flow modify the equilibrium orientation of Janus particles?, 2) What are different dynamics that particles can experience subject to such flow?, 3) How does the rotational dynamics depend on particle size, shape, and surface chemistry?, 4) Will the particle eventually approach a steady orientation at a sheared interface?, 5) If so, can we control that orientation by manipulating the flow field?

To answer these questions, we follow a Molecular Dynamics approach similar to that in previous chapter, and impose linear shear flow to Janus nanoparticles adsorbed at the interface. MD simulations have been used in the literature to reveal the interfacial slip, local stream velocity, shear stress, and rate of entropy generation for shear flows at liquid–liquid interfaces [106-108].

We create Janus nanoparticles of different amphiphilicity in a similar manner as described in previous chapter. The particle is placed at the interface between the two fluids at the center of simulation box bounded by two solid walls, and the shear is modeled as a symmetric Couette flow. The orientation and interfacial transport of the particle is monitored as a function of time. It should be noted though that such analysis cannot be fully captured with theoretical methods due to presence of line tension and capillary wave effects [109], as well as complex directional particle-fluid interactions.

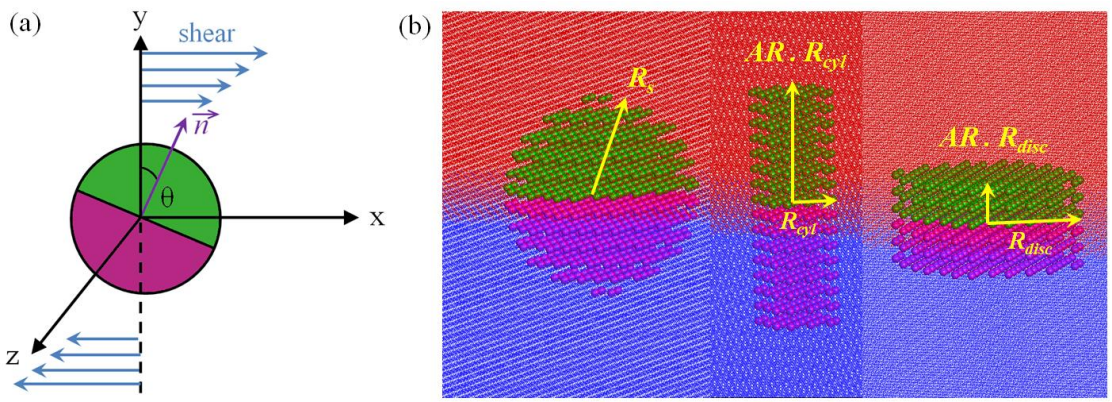

Figure 4.1 (a) Schematic of the orientation angle for Janus particles at the interface, (b) the initial configuration of Janus nanoparticles of different geometry (AR = aspect ratio) at a liquid interface.

The simulation box is similar to the one shown in Figure 3.1, while the symmetric shear is induced by moving the top and bottom walls with equal velocities u_{drive} in opposite directions. The imposed flow should be significant compared to Brownian dynamics of the particles, but well below the range leading to non-linear slip between nanoparticle and the fluids [110]. We characterize the orientation using the orientation angle θ, which forms the angle between normals to Janus boundary and the interface plane, as shown in Figure 4.1(a). The results of previous section indicate that in the absence of shear flow, Janus spheres take the upright orientation ($\theta = 0^o$) which corresponds to each side being immersed in its favorite fluid. However, the orientation angle may be tuned upon applying the shear as the shear stresses applied on particle surface will try to induce a clockwise rotation.

The analysis can be more complicated for non-spherical Janus particles as the contact radius and surface area normal to shear direction continuously change upon rotation. More elongated particles sitting upright at the interface are generally expected to tilt more at the interface. We consider the hydrodynamics of Janus spheres, cylinders, and

discs as shown in Figure 4.1(b). There should be an attainable range of orientations for each particle shape, size, and amphiphilicity by controlling the shear rate of the imposed flow. We will find this range and evaluate different dynamics experienced by Janus particles toward the steady orientation.

4.2 Shear-Induced Response of Single Particles

Here, we present our findings on translation and rotational dynamics of individual Janus particles at a sheared interface. We demonstrate the possibility of directing particles to different orientations by controlling their surface chemistry and the applied shear rate, and explain their steady behavior by measuring the net torque imposed by the two fluid species.

4.2.1 Translational Motion of Janus Particles at a Sheared Interface

We investigate the motion of Janus particles at the interface between fluids similar to those used in the previous chapter for modeling the interfacial diffusion. The two fluids are assumed to have equal density of $\rho = 0.8\ \sigma^{-3}$, viscosity of $\eta = 2.0\ m.\sigma^{-1}.\tau^{-1}$, and the interfacial tension calculated as $\gamma = 1.47\ \varepsilon.\sigma^{-2}$. The translational motion is quantified using the mean-squared displacement of the particle as a function of time. Similar to the case of a stationary interface, the particle shows negligible motion in the direction normal to the interface ($MSD_y \approx 0$), thus indicating that the shear flow does not lead to particle detachment. This trend was confirmed for all particle geometries within the whole investigated range of shear rate ($\dot{\gamma} < 0.05\,\tau^{-1}$). Calculating the average fluid velocity profile shows a symmetric distribution with respect to the interface plane with negligible

slip between the particle surface and its surrounding fluid species. Therefore, it is verified that the flow does not lead to instability of these particle-laden interfaces or transport of the amphiphilic particles, as expected based on the symmetric nature of the applied shear.

4.2.2 Tilting and Tumbling Dynamics under Shear Flow

In the absence of shear, each particle adsorbs at the interface according to the energetically favorable orientation dictated by preferred wetting condition. For Janus spheres, this corresponds to the upright configuration ($\theta = 0^o$ in Figure 4.1(a)) where each side is completely in contact with its favorite fluid phase [44-46]. Continuum predictions suggest a similar upright orientation for disc-shaped particles and cylinders of intermediate aspect ratio studied here [37]. Our molecular simulations on Janus nanoparticles at a stationary interface ($u_{drive} = 0$) also resulted in an analogous prediction as the particle was found to preserve the initial orientation of $\theta = 0^o$ over long simulation times.

Upon shearing the interface, the particle may start to deviate from the upright orientation due to the clockwise torque imposed by the symmetric shear flow. To evaluate this, we placed a Janus sphere with $R = 6\sigma$ and $\beta = 60^o$ at the interface and increased the shear rate from 0 to $\dot{\gamma} = 0.045\,\tau^{-1}$. The temporal evolution of the orientation angle subject to different hydrodynamic flows is depicted in Figure 4.2 over a period of $0 \leq t/\tau \leq 1000$. We observe that at a stationary interface, the orientation is $\theta = 0^o$ as expected based on the preferred wetting condition between apolar/oil and polar/water interfaces. Upon applying the shear flow, the particle starts to rotate out of the original upright configuration and the shear torque can partially expose each region to both fluid phases. There is a transient period over which the orientation angle smoothly

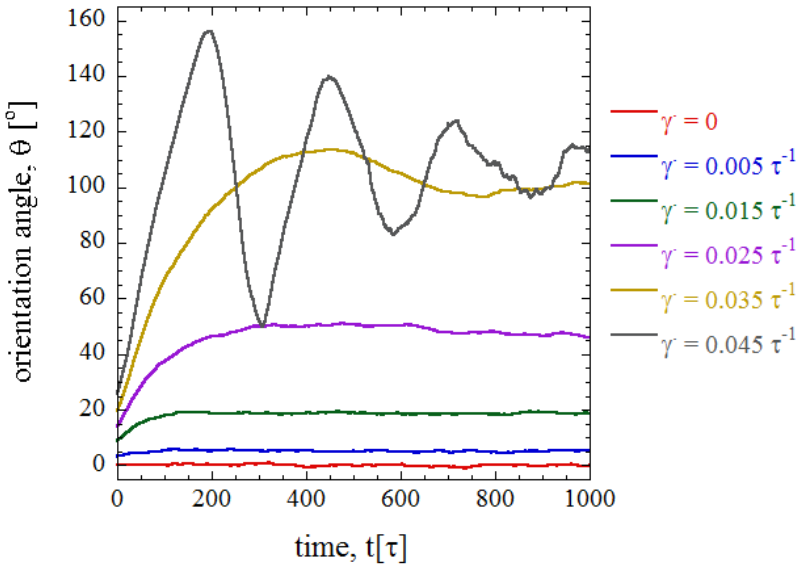

Figure 4.2 Temporal evolution of the orientation angle of a Janus sphere with β = 60º under various interfacial shear rates.

increases until reaching a steady orientation which is maintained over long simulation times.

If the shear rate is further increased, the particle undergoes an overshoot in orientation and eventually exhibits an oscillatory variation in θ. Placing a tracker point on the surface of the particle and following its trajectory over time suggests that the particle experiences a tumbling motion at such high shear rates. This was observed for the above sphere and is plotted in Figure 4.3 for two other geometries, namely a Janus disc and a cylinder, under the same shear rate of $\dot{\gamma} = 0.045\ \tau^{-1}$. The tumbling can be attributed to the significantly large ratio of the shear to capillary torque, which continuously rotates the particle until finding the optimum orientation. This will be discussed in more details in section 4.3.4.

For all geometries, we observed that Janus particles experience these two possible regimes: smooth tilt and tumbling. Depending on the geometry and surface chemistry, the dynamics can be different at a particular shear-rate. This is demonstrated in Figure 4.4 by phase diagrams for particles with three different amphiphilicities and over a range of

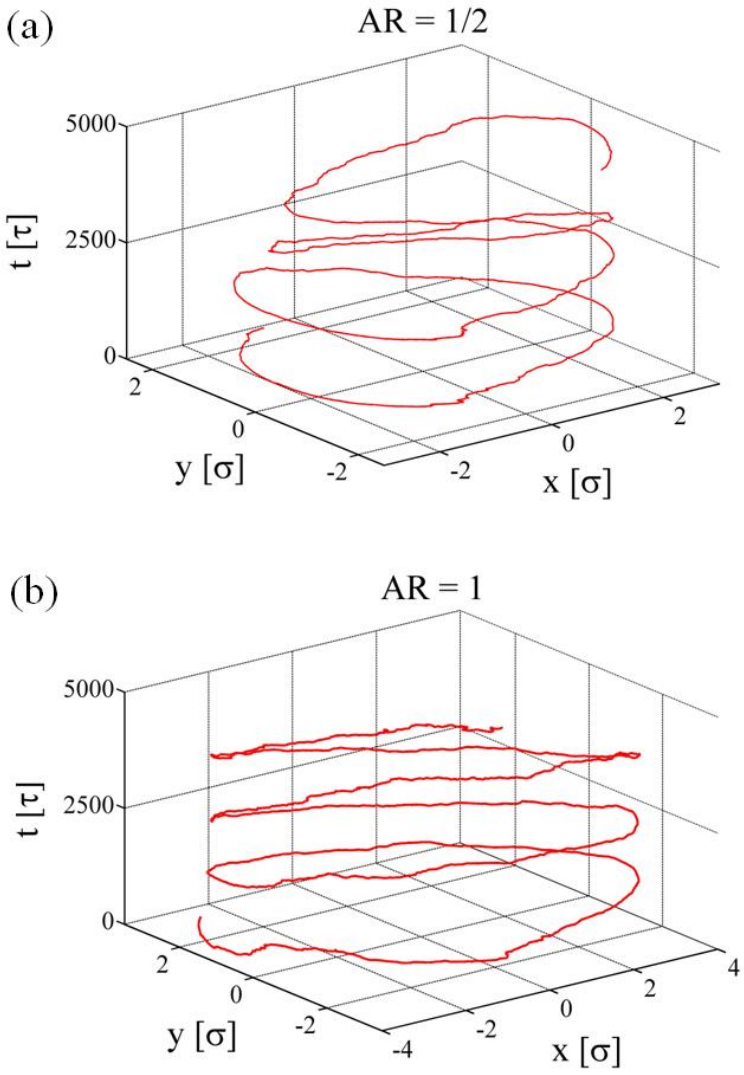

Figure 4.3 Trajectories in x-y plane vs. time for (a) Janus disc with *AR = 1/2*, (b) cylinder with AR = 1, and β = 60º at an interface sheared with $\dot{\boldsymbol{\gamma}} = \mathbf{0.045}\ \boldsymbol{\tau}^{-\mathbf{1}}$, showing the tumbling dynamics.

aspect ratio and shear rate. Note that *AR < 1* corresponds to discs, while *AR ≥ 1* represents cylindrical particles. We observe that the tumbling region shrinks upon increasing *β* due to enhanced preferred wetting of each side with its favorite fluid, leading to larger resistance against rotation above *θ = 90º*. Interestingly, the shape of this region is basically similar irrespective of the amphiphilicity, showing a minimum near *AR = 1*. More isotropic particles have a higher tendency to undergo tumbling as the geometry

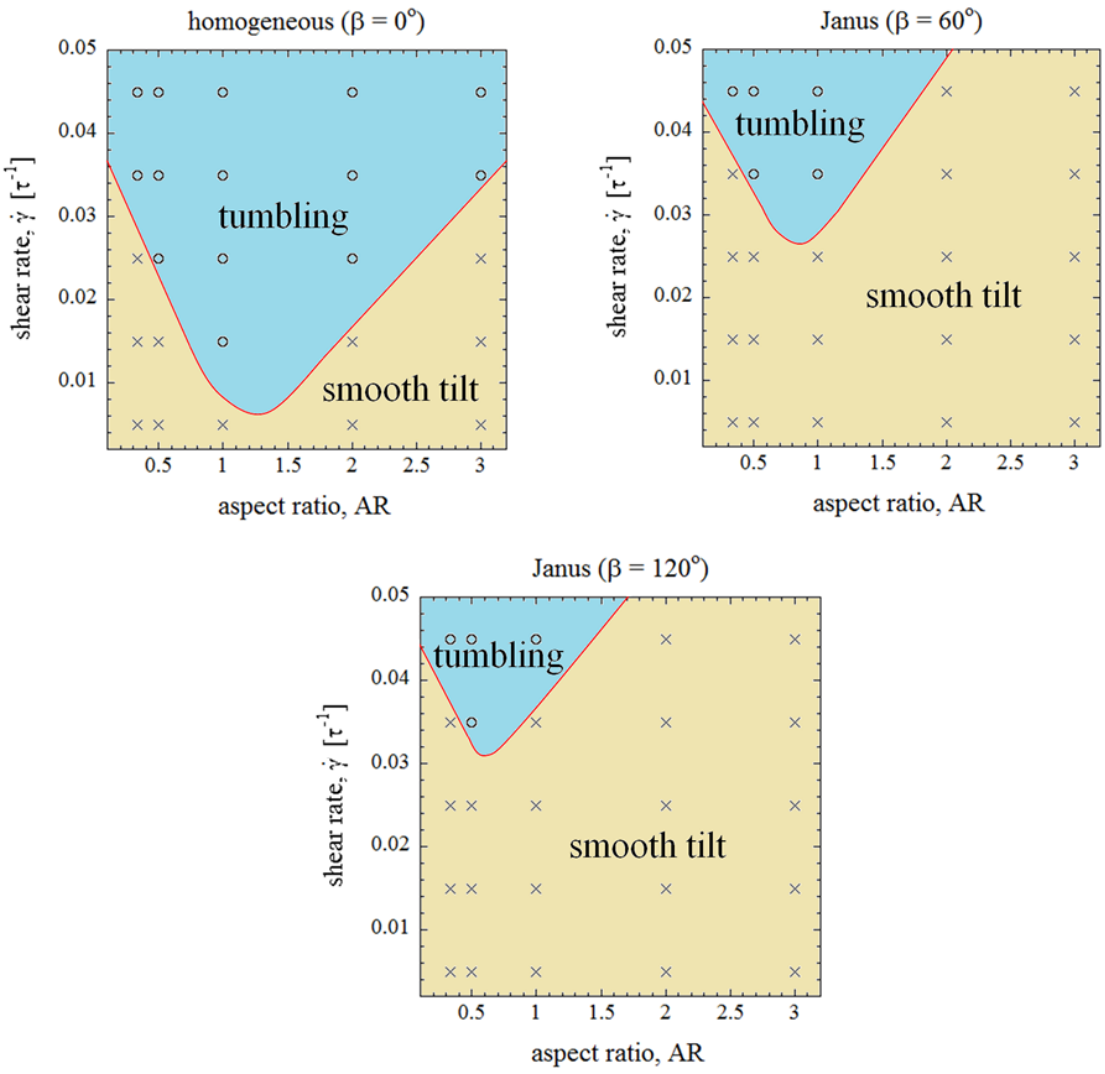

Figure 4.4 Phase diagrams showing the orientational dynamics regimes of cylindrical/disc-shaped particles as a function of the aspect ratio and the applied interfacial shear rate at different amphiphilicities.

does not impose a preferred orientation under the flow. Furthermore, the phase diagrams suggest that elongated Janus cylinders do not experience tumbling dynamics within the investigated range of shear rates, while homogeneous cylinders with $AR > 3$ can exhibit such behavior under large shear rates. This proves the larger stability of Janus particles under shear flow compared to their homogeneous counterparts, clearly due to the enhanced interfacial tension between solid-fluid regions.

Overall, this plot enables first-hand prediction of the rotational dynamics experienced by discs/cylinders with different aspect ratio and amphiphilicity subject to interfacial shear flows. It suggests the possibility of obtaining distinct dynamics for particles subject to imposed shear flows simply by tuning their surface chemistry.

4.2.3 Steady Orientation of the Particles at Sheared Interfaces

Irrespective of the type of dynamics, we note that any particle eventually reaches a steady-state orientation at a liquid interface under shear flow. Our simulations indicate that the steady response of particles to shear is extremely shape-dependent. The equilibrium orientation of a Janus sphere as well as discs/cylinders with the aspect ratio *AR = 1/3 – 3* is plotted in Figure 4.5 for the example case of the amphiphilicity characterized by $\beta = 60^o$. The interfacial shear rate is varied in the range $\dot{\gamma} = 0 - 0.05\,\tau^{-1}$, and the particle dynamics is tracked for sufficient time until the change in orientation becomes negligible. We note that elongated cylinders are significantly tilted

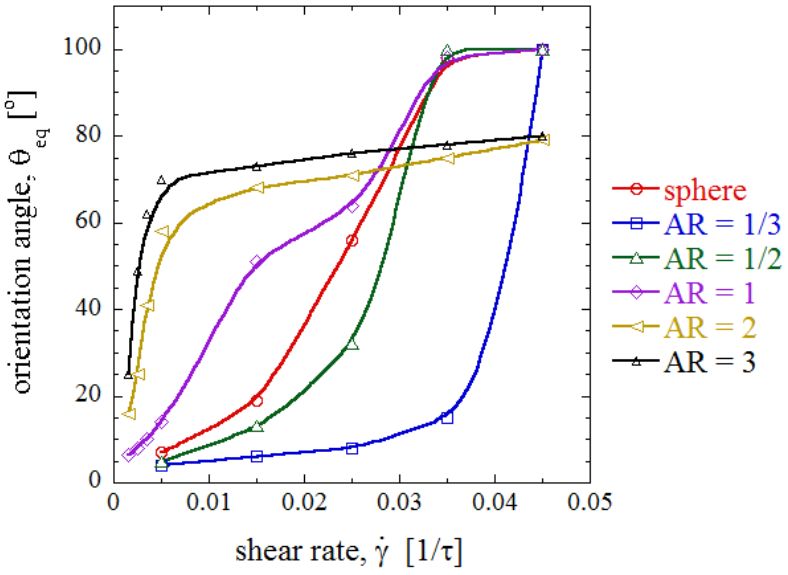

Figure 4.5 The steady orientation adopted by Janus particles with amphiphilicity β = 60° and different aspect ratio at the interface as a function of the applied shear rate.

even at shear rates as low as $\dot{\gamma} = 0.005\ \tau^{-1}$, while disc-shaped particles (*AR < 1*) require a much larger shear rate to yield visible rotation out of the initially-upright configuration. As explained earlier, this is attributed to the smaller shear-facing area and longer contact line of Janus discs in comparison with more elongated particles. As a consequence, the resistive capillary torque is more significant at the upright configuration, requiring a larger shear rate to rotate the particle. As an example, the shear rate required to induce *15°* rotation is *~10* times larger for a Janus disc with *AR = 1/3* compared to an elongated cylinder with similar area and amphiphilicity but an aspect ratio of *3*.

Furthermore, Janus cylinders represent two almost linear regimes: a considerable increase in the orientation angle with increasing shear rate, followed by a region of much reduced rate of change in tilting. The reduced slope is due to a reduction in rate of change of the shear-facing area as the cylinder approaches the horizontal configuration at the interface. On the other hand, Janus discs exhibit a wider region of negligible tilt, followed by a sudden shift in orientation. The most uniform control of orientation with the applied shear rate is achieved for spheres and the isotropic cylinder with *AR = 1*, due to their fixed frontal area and contact radius irrespective of the orientation. For any particle geometry, we can thus control the final configuration at the interface by regulating the hydrodynamic flow field.

More importantly, the orientation of any particle geometry under a given flow can be tuned solely by modifying its surface chemistry. Upon increasing the difference in wettability of the two regions (β), the capillary torque is enhanced and the orientation angle becomes smaller. This is shown in Figure 4.6 by surface plots of $\theta = \theta(\beta, \dot{\gamma})$ for two particle geometries. We clearly observe the enhanced tilting upon increasing the

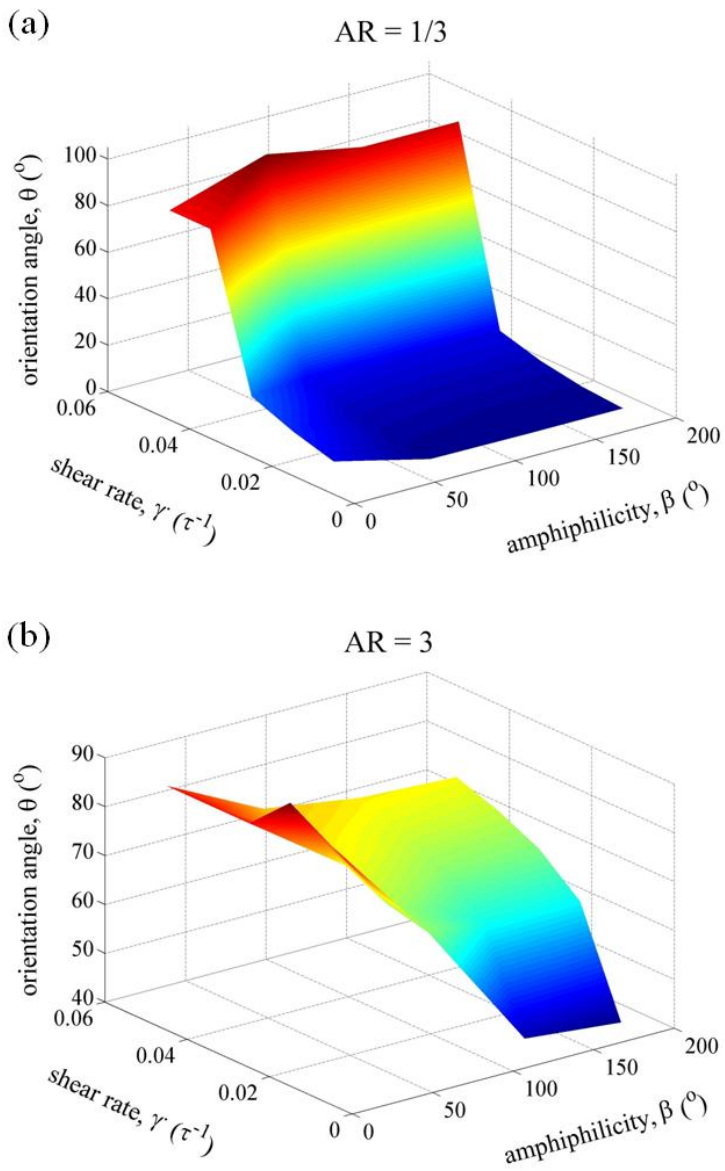

Figure 4.6 Surface plot of the steady-state orientation angle for Janus particles with (a) AR = 1/3, and (b) AR = 3, as a function of the amphiphilicity and interfacial shear rate.

shear rate, but the rate of change in orientation depends on the amphiphilicity. The effect of surface chemistry in tuning the orientation is more pronounced at larger aspect ratios. The driving mechanism for difference in dynamics and steady behavior of Janus particles of distinct shape/amphiphilicity is discussed in the following section.

4.2.4 Driving Mechanism for Observed Rotational Dynamics

We observed that depending on the shear rate as well as the shape and amphiphilicity, a particle may experience two types of dynamics at a liquid interface: (1) Smooth tilt: the orientation angle smoothly increases over a transient period, after which a steady orientation is maintained; (2) Tumbling: the particle tumbles but does not detach from the interface, until it eventually finds a stable configuration. In case of smooth tilting, the magnitude of rotation out of upright orientation would generally depend on the shear-induced torque. For elongated cylinders with $AR > 1$, the shear-facing area is larger than that of thin discs, such that a larger shear torque would result under similar flow conditions. Also, a smaller capillary torque resists against the rotation due to smaller length of the contact line. Therefore, Janus cylinders tilt more than discs of similar area at a sheared interface. On the other hand, as a Janus cylinder tilts more toward a horizontal orientation, the contact length increases while the shear-facing area drops. As a consequence, the capillary torque increases and the shear-induced torque decreases, inducing a smooth tilt as the net torque approaches zero. The trend is reversed in case of disc-shaped particles ($AR < 1$), such that the increasing T_{shear} and decaying T_{cap} favor further rotation of the particle under shear flow. Consequently, the particle rotates over $\theta \approx 90^o$ leading to significant distortion of the interface which can favor a tumbling motion.

In order to further clarify the role of capillary torque in controlling the orientation and the interface deformation induced by preferred wetting condition, we examine the radial and circumferential distribution of the fluid atoms around a sample particle. Due to simplicity in computation and visualization, we carry out this analysis on a spherical particle, but the physics also holds for other geometries. For a Janus sphere with a size of $R = 6\sigma$ and amphiphilicity $\beta = 120^o$, the distribution function $g(r,\theta)$ is calculated by

averaging that sufficient time and several realizations. Figure 4.7 shows contour plots of the distribution function $g_1(r,\theta)$ for the bottom fluid around the particle under three different interfacial shear rates. The steady-state orientation of the sphere under each flow is also demonstrated for visualizing the solid/fluid interfaces.

As the shear rate increases and the particle rotates more out of the upright ($\theta = 0^o$) configuration, the interface deformation becomes more pronounced. The distortion is such that each solid region remains mostly exposed to its favorable fluid phase as expected based on the continuum prediction [66]. Similarly, in case (c) where the particle rotates by $\approx 98^o$, a thin wetting layer of each fluid phase rotates with its favorable solid

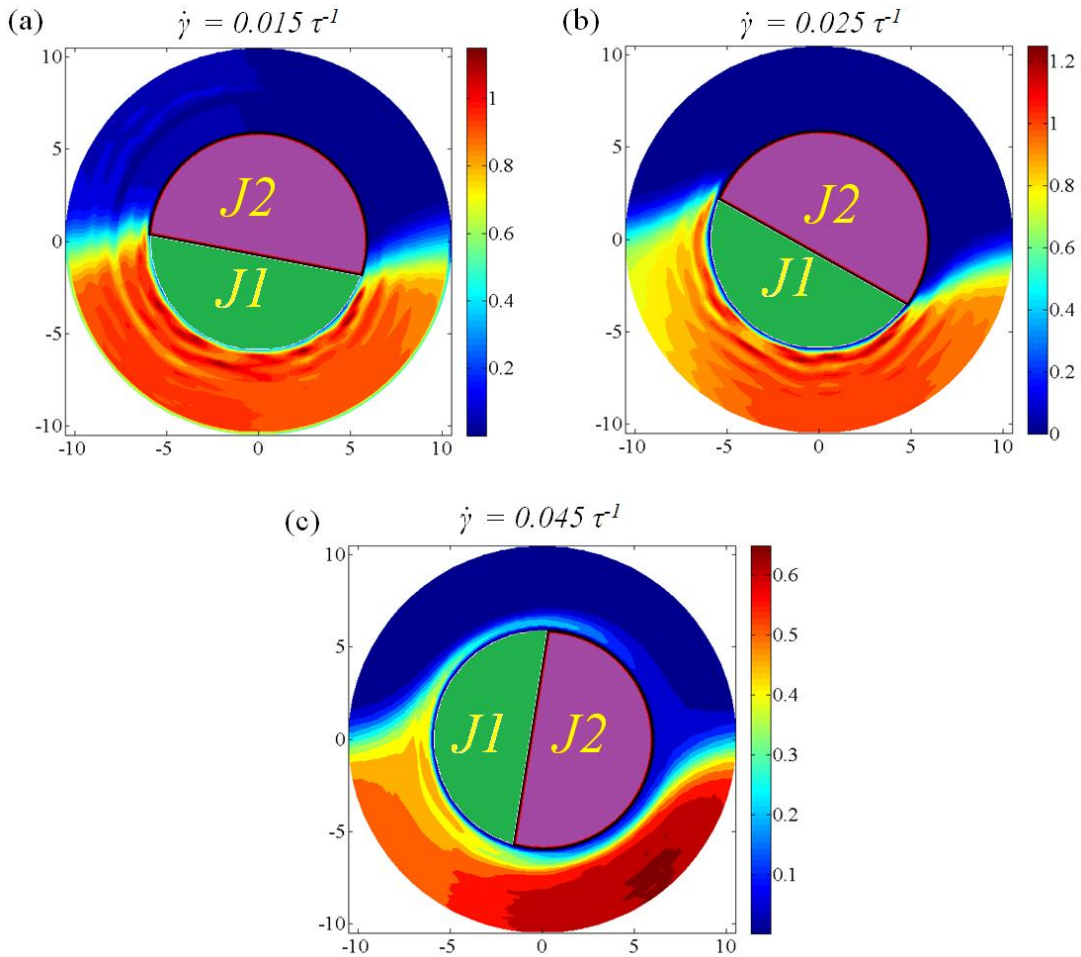

Figure 4.7 Contour plots of the distribution function for bottom fluid around a spherical particle with R = 6σ and β = 120º subject to different interfacial shear rates.

surface into the opposite side of the interface and extends up to the location of the Janus boundary. Since the distribution is obtained by averaging over a long period of time, it implies that this wetting layer is formed and maintained around the nanoparticle as is rotates at the interface. Such microscopic layering has also been observed upon translating a Janus particle from one bulk fluid to the other phase [86]. Overall, the increasing deformation of the interface upon deviating from the upright orientation confirms the resistive nature of the capillary torque against clockwise rotation induced by the shear flow. Therefore, the steady configuration adopted by the particle is expected to be governed by the balance between these two contributions.

To evaluate this, we measure the ensemble-average torque acting on the particle in x-y plane by tracking the particle in multiple realizations and building histograms of the net torque as the particle crosses specific orientations. The result is shown in Figure 4.8(a) over a limited range of orientations for three example cases corresponding to cylindrical particles with $AR = 1,2,3$ and $\beta = 60^o$ under a shear rate of $\dot{\gamma} = 0.015\ \tau^{-1}$. The temporal evolution of the orientation for these Janus cylinders is shown in Figure 4.8(b) showing a smooth tilting before reaching the steady configuration. We clearly observe that in all cases, the orientation at which the net torque becomes zero corresponds exactly to θ_{eq} achieved after the transient stage. Therefore, the equilibrium orientation is justified based on the balance between shear and capillary torques.

A similar methodology was followed for particles with tumbling interfacial dynamics. In such cases, as the particle covers a wider range of orientations during its evolution and can go beyond 180^o rotation, we use an alternative definition of θ depending on the location of normal vector $\vec{n}$ in x-y plane in order to distinguish between the clockwise

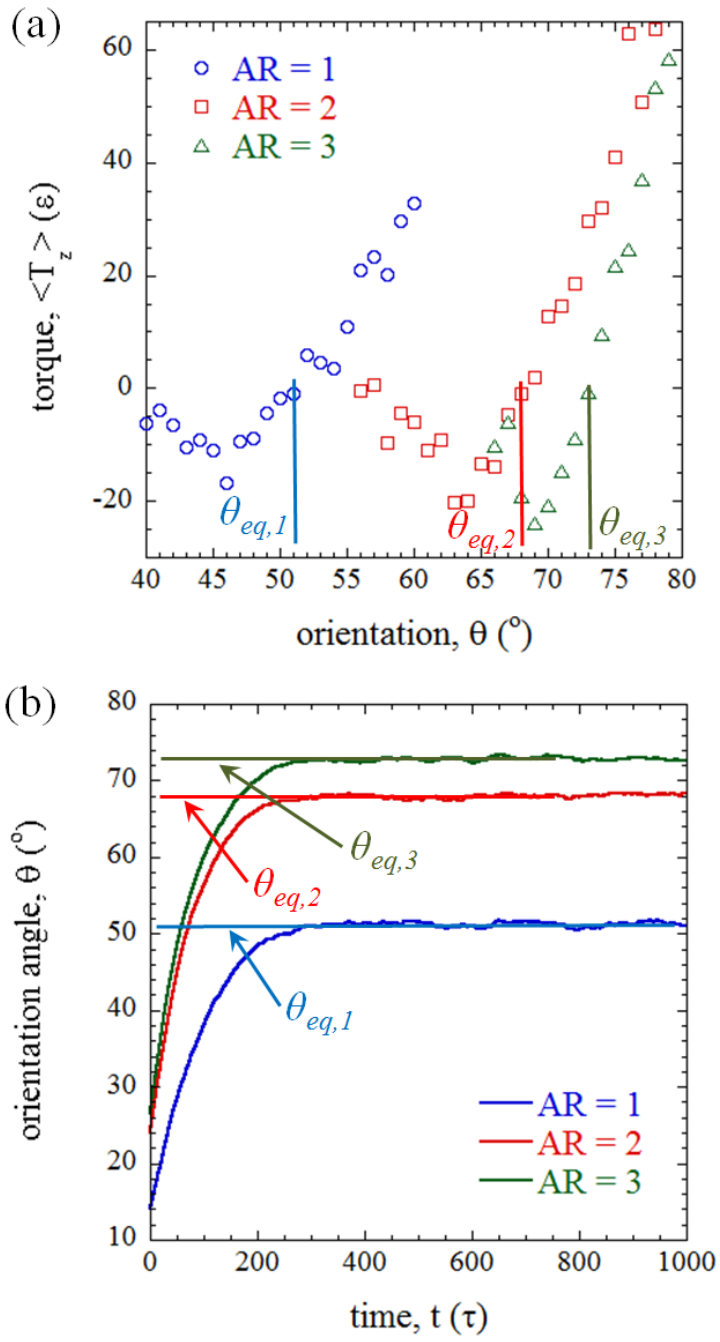

Figure 4.8 (a) The average net torque acting on cylindrical particles with β = 60º and AR = 1,2,3 under an interfacial shear rate of 0.015 τ^{-1}, (b) the evolution of the orientation angle for these particles corresponding to the tilting regime.

and counter-clockwise rotation. The ensemble-average torque $\langle T_z \rangle$ is shown in Figure 4.9(a) over the full range of $0^o \leq \theta \leq 360^o$ for a sample case corresponding to a Janus cylinder with $AR = 1$ and $\beta = 60^o$ tumbling at the interface under the maximum

investigated shear rate of $0.045\ \tau^{-1}$. The result suggests that the net torque becomes negligible at three intermediate orientations. More importantly, the magnitude of the torque and its variation with θ is much smaller than cases with non-tumbling dynamics

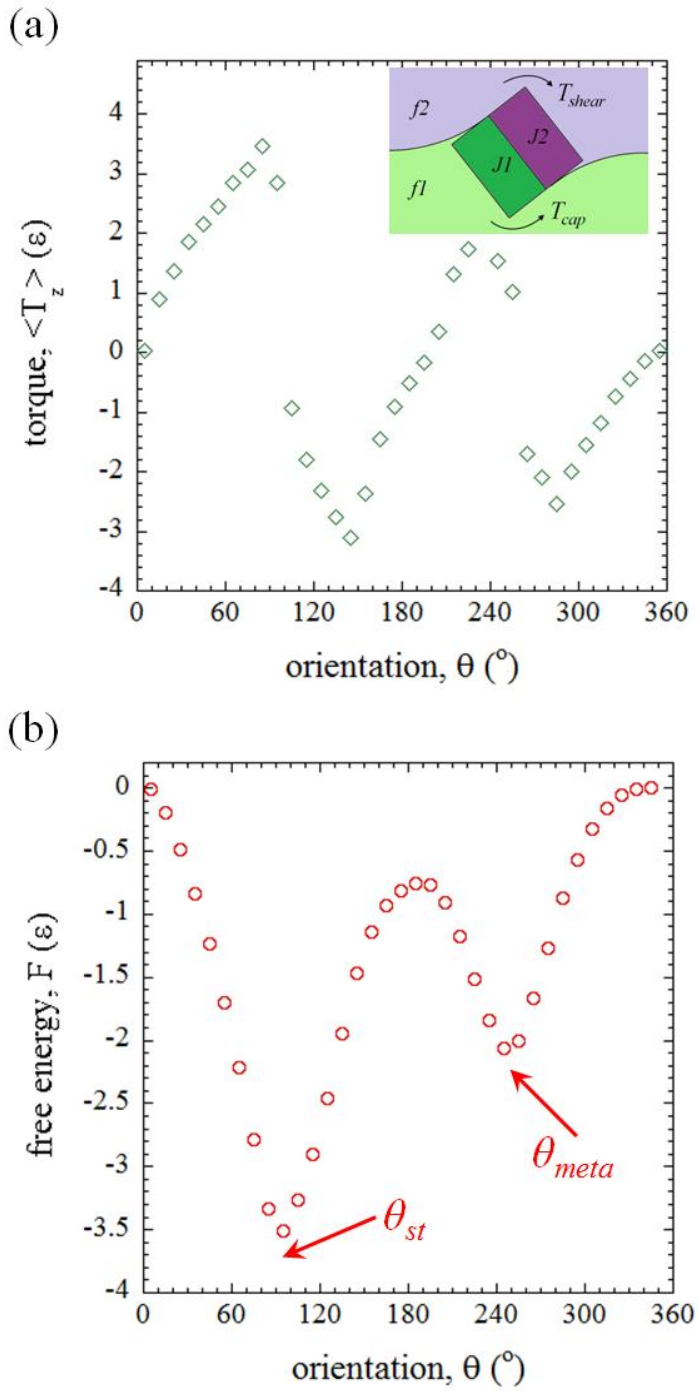

Figure 4.9 (a) The average net torque, (b) the free energy, for a Janus cylinder with AR = 1 and amphiphilicity β = 60° undergoing tumbling dynamics at an interface sheared at 0.045 τ^{-1}.

shown in Figure 4.8(a) (~7ε as compared to ~80ε). Having measured $\langle T_z \rangle$, we can then calculate the change in Helmholtz free energy F by integrating the average torque as the particle rotates from a reference point ($\theta_{ref} = 0^o$) using

$$\Delta F(\theta_i) = F(\theta_i) - F(\theta_{ref}) = -\int_{\theta_{ref}}^{\theta_i} \langle T_z \rangle_{\theta'} d\theta' \quad (4.1)$$

The resulting free energy profile is shown in Figure 4.9(b), revealing two energy minima corresponding to stable/metastable states at $\theta \approx 100^o, 250^o$, respectively. Note that both states correspond to zero mean torque thus trapping the particle at these orientations. Interestingly, the stable state ($\theta \approx 100^o$) coincides with the final orientation adopted by the particle after the tumbling motion is suppressed. Therefore, the steady-state configuration for this tumbling particle is also driven by a minimization of free energy. Our simulations predict an analogous trend for particles of other geometries and surface chemistry undergoing tumbling dynamics.

Furthermore, we note that the difference in free energy of all orientations is < 4ε, which is much smaller than those of particles undergoing a smooth tilt. This explains the driving force for the tumbling motion, which is associated with the small torque and free energy difference between various orientations. Such dynamics is more prevalent for Janus spheres and cylinders with $AR = 1$ (see Figure 4.4) since they provide the most isotropic geometries leading to smallest deviation in free energy of different orientations.

In summary, our molecular simulations on individual Janus particles suggest the possibility of tuning the orientation by controlling the shape, degree of amphiphilicity, and the applied shear rate. These results suggest the possibility of directing Janus particles to desired orientations at a liquid interface, which can be potentially helpful in design of novel functional materials. As the final step, we extend this analysis by

considering multiple Janus particles at a sheared interface, and predict their ordering/assembly using larger-scale simulations.

4.3 Shear-Induced Assembly of Multiple Particles

Having analyzed the dynamics experienced by individual particles of different shape and surface chemistry under an interfacial shear flow, we would like to investigate the effect of such flow on inter-particle forces and self-assembled structure when multiple Janus particles are present at an interface. Here, we aim to evaluate whether it is possible to predict the shape/properties of the resulting structure as a function of particle characteristics and the applied flow field. Modeling the dynamics of multiple particles at the interface requires a larger domain size and longer timescale. While microscopic techniques such as MD are suitable for capturing details of fluid structure and solid/fluid interactions at the interface, they are not well suited for simulating such domains as they become computationally expensive. Continuum solvers, on the other hand, are adept at handling macroscopic phenomena, but have difficulty capturing details of the physics occurring at the interface. Mesoscopic approaches such as the lattice-Boltzmann method (LBM) provide the best tool for such problems as they can incorporate many advantages of microscopic techniques while still efficiently simulating larger scale dynamics. This has made the LBM a useful method for simulating interfacial systems including the capillary forces between solid particles, formation/stability of particle-stabilized emulsions, and the response of such particle-laden interfaces to hydrodynamic flows [111-114]. Moreover, this method allows an easy implementation of complex boundary conditions, and is well suited for execution on parallel supercomputers due to its high

degree of locality [115]. Here, we use such lattice-Boltzmann scheme for simulating the hydrodynamics of a cluster of Janus particles at sheared interfaces.

Fundamental Questions

1) When multiple Janus particles are adsorbed at a liquid interface, how do they rotate and interact in response to a shear flow?, 2) Can we use the flow to direct a cluster of randomly-distributed particles to specific positions/orientations?, 3) If so, what types of self-assembled structures can be formed by the particles?, 4) How does the ordering depend on particle size, surface coverage, and the applied shear rate?, 5) How is the assembled structure modified if the flow field is subsequently removed?

4.3.1 Numerical Approach for Mesoscopic Simulations

The fundamental idea of the lattice-Boltzmann method is that the fluids can be imagined as consisting of a number of small particles moving with random motions and exchanging momentum and energy. The method consists of a regular lattice with particles residing on the nodes, where an ensemble average of particle occupation number is defined as a single-particle distribution function f. The discrete equation for the evolution of LBM is

$$f_\alpha(\boldsymbol{x} + \boldsymbol{e}_\alpha, t+1) = f_\alpha(\boldsymbol{x}, t) = \boldsymbol{\Omega}_\alpha(f(\boldsymbol{x}, t)) \tag{4.2}$$

where the subscript α indicates the distribution function corresponding to a particular discretized velocity direction, $\boldsymbol{e}_\alpha$. We will use D3Q19 scheme, in which the velocities are discretized in 3 dimensions with 19 velocity directions at each lattice site [116, 117]. $\boldsymbol{\Omega}_\alpha = \boldsymbol{\Omega}_\alpha(f(\boldsymbol{x}, t))$ is the collision operator which represents the rate of change of f_α resulting from collision. The Navier-Stokes equations can be recovered by LBM with

a proper choice of this collision operator. In principle, starting from an initial state, the configuration of particles at each time step evolves in two sequential sub-steps: (a) streaming, in which each particle moves to the nearest node in the direction of its velocity, and (b) collision, which occurs when particles arriving at a node interact and change their velocity directions according to scattering rules. The macroscopic thermodynamic variables can be expressed as the moments of the distribution function with different order with respect to velocity. Specifically, the density and momentum density of the fluid can be obtained as

$$\rho = \sum_\alpha f_\alpha \quad , \quad \rho \boldsymbol{u} = \sum_\alpha f_\alpha \boldsymbol{e}_\alpha \tag{4.3}$$

where the summation runs over all lattice velocity directions α. Moreover, the collision operator Ω_α is required to satisfy conservation of total mass and momentum at each lattice node

$$\sum_\alpha \boldsymbol{\Omega}_\alpha = 0 \quad , \quad \sum_\alpha \boldsymbol{\Omega}_\alpha \boldsymbol{e}_\alpha = 0 \tag{4.4}$$

The kinetic equation for distribution function can be written using Eq. (4.2) as

$$\frac{\partial f_\alpha(\boldsymbol{x},t)}{\partial t} + \boldsymbol{e}_\alpha . \boldsymbol{\nabla} f_\alpha(\boldsymbol{x},t) = \boldsymbol{\Omega}_\alpha \tag{4.5}$$

In the current problem, we are dealing with a system of two immiscible fluids with interacting particles. For this purpose, we use the multi-component LBM implementation of Lee and Liu [118], which belongs to the class of free energy-based multi-component lattice Boltzmann algorithms. Using a popular single relaxation-time form for the collision term and incorporating the intermolecular forces, the above kinetic equation for the transport of binary fluids can be written as [118]

$$\frac{\partial f_\alpha}{\partial t} + \boldsymbol{e}_\alpha . \boldsymbol{\nabla} f_\alpha = -\frac{1}{\lambda}\left(f_\alpha - f_\alpha^{eq}\right) + \frac{1}{c_s^2}(\boldsymbol{e}_\alpha - \boldsymbol{u}) . \boldsymbol{F}\Gamma_\alpha \tag{4.6}$$

where $\boldsymbol{u}$ is the volume-averaged velocity, c_s is the speed of sound, λ is the relaxation time, $\boldsymbol{F}$ is the intermolecular force, $\Gamma_\alpha(\boldsymbol{u}) = f_\alpha^{eq}/\rho$, and f_α^{eq} is the equilibrium distribution function defined by

$$f_\alpha^{eq} = t_\alpha \rho \left[1 + \frac{\boldsymbol{e}_\alpha.\boldsymbol{u}}{c_s^2} + \frac{(\boldsymbol{e}_\alpha.\boldsymbol{u})^2}{2c_s^4} - \frac{\boldsymbol{u}.\boldsymbol{u}}{2c_s^2}\right] \tag{4.7}$$

where t_α is a weight function corresponding to $\boldsymbol{e}_\alpha$, and ρ is the mixture density. Surface tension effects arise from the inclusion of the intermolecular force which is written as

$$\boldsymbol{F} = \nabla\rho c_s^2 - (\nabla p + \mu\nabla C) \tag{4.8}$$

where p is the dynamic pressure and μ is the chemical potential. The discrete Boltzmann equation (DBE) given in (4.6) which involves mass and momentum can be transformed into a DBE for pressure evolution and momentum [118] by defining a new distribution function $g_\alpha = f_\alpha c_s^2 + (p - \rho c_s^2)\Gamma_\alpha(0)$ with corresponding equilibrium distribution function $g_\alpha^{eq} = f_\alpha^{eq} c_s^2 + (p - \rho c_s^2)\Gamma_\alpha(0)$. The DBE in terms of g_α then becomes

$$\frac{\partial g_\alpha}{\partial t} + \boldsymbol{e}_\alpha.\boldsymbol{\nabla} g_\alpha = -\frac{1}{\lambda}\left(g_\alpha - g_\alpha^{eq}\right) + (\boldsymbol{e}_\alpha - \boldsymbol{u}).[\nabla\rho c_s^2(\Gamma_\alpha - \Gamma_\alpha(0)) + \mu\nabla C\Gamma_\alpha] \tag{4.9}$$

On the other hand, since we are dealing with a binary system of fluids, we need to keep track of the interface position. We define the composition C as the volume fraction of the heavier fluid (component 1), such that the local densities of the two species can be defined as $\tilde{\rho}_1 = C\rho_1$and $\tilde{\rho}_2 = (1 - C)\rho_2$, with ρ_1, ρ_2 being the bulk density of the two fluids. The mixture density at each lattice site is thus a linear function of the composition: $\rho = \tilde{\rho}_1 + \tilde{\rho}_2 = C\rho_1 + (1 - C)\rho_2$. In order to track C during the simulation, another distribution function is introduced: $h_\alpha = (C/\rho)f_\alpha$ with $h_\alpha^{eq} = (C/\rho)f_\alpha^{eq}$. The corresponding DBE for h_α can be written as

$$\frac{\partial h_\alpha}{\partial t} + \boldsymbol{e}_\alpha.\boldsymbol{\nabla} h_\alpha = -\frac{1}{\lambda}\left(h_\alpha - h_\alpha^{eq}\right) + M\nabla^2\mu\Gamma_\alpha + (\boldsymbol{e}_\alpha - \boldsymbol{u}).\left[\nabla C - \frac{C}{\rho c_s^2}\nabla p - \mu\nabla C\right]\Gamma_\alpha \tag{4.10}$$

It can be shown [118] that Eqs. (4.9, 4.10) recover the pressure evolution and momentum equations for each fluid as well as the advective Cahn–Hilliard equation for a binary system of immiscible fluids which describes the evolution of the composition, C, of the system as it progresses towards its equilibrium state.

The lattice-Boltzmann equations (LBEs) can be obtained by integrating the DBEs (4.9, 4.10) along characteristic directions *e.g.* using a trapezoidal approximation over a time step δt. The numerical approach thus basically consists of solving those two LBEs over time. The macroscopic variables $C, \rho\boldsymbol{u}, p$ can then be computed using moments of the distribution functions g_α, h_α at each lattice node and at any time-step.

The boundary conditions required to solve the LBEs are as follows: Firstly, the discrete distribution functions on solid boundaries have to be taken care of to reflect the macroscopic BCs of the fluid. Bounce-back conditions are typically used to implement no-slip on the boundary. By the so-called bounce-back we mean that when a fluid particle (discrete distribution function f_α) reaches a solid boundary node, the particle will scatter back to the fluid along with its incoming direction. This algorithm must be supplemented for the case of moving walls (*e.g.* solid particles) so that the fluid velocity matches the wall velocity. The scheme can be written as $f_{\bar{\alpha}} = f_\alpha + 2\rho/c_s^2 t_\alpha(\boldsymbol{u}_b.\boldsymbol{e}_{\bar{\alpha}})$, where $\bar{\alpha}$ is the bounce-back direction (opposite of α) and $\boldsymbol{u}_b$ is the boundary velocity which can be computed from the particle position and velocity. The other distribution functions g_α, h_α after bounce-back are obtained in a similar way. Secondly, two boundary conditions are required to evolve the composition C. To ensure no mass flux normal to a solid boundary due to a chemical potential gradient, we impose $\boldsymbol{n}.\nabla\mu|_S = 0$, where $\boldsymbol{n}$ is the normal unit vector to the surface. The second boundary condition is established by minimizing the

free energy, which can be derived [118] as $\boldsymbol{n}.\nabla C|_S = \phi_c/\kappa\,(C_s - C_s^2)$, where ϕ_c and κ are constants chosen to recover the fluid viscosity and desired contact angle at equilibrium.

To address particle dynamics, the forces from the fluid on the particle must first be calculated. The particles are placed on the lattice leading to the boundary surfaces cutting some of the links between lattice nodes as shown in Figure 4.10(a). The fluid particles moving along these links interact with the solid surface at boundary nodes. The interactions between the fluid and the particles are introduced by marking all lattice sites that are inside the particle as solid nodes for the fluid, at which bounce-back boundary conditions are applied [119-121]. As a result of the boundary-node interactions, forces and torques are exerted on the solid particles, which are obtained based on the local momentum exchange between the fluid and the particle followed by summing the force/torque over all boundary nodes associated with any particle. Subsequently, the particle position and velocity are updated according to Newton's second law. To avoid the overlap of particles, a lubrication and/or spring force is added to particles near contact.

Our numerical method which combines the multi-component algorithm with particle dynamics has been recently validated for a single and a pair of homogeneous particles placed at a fluid interface [122]. It was verified that a single particle reaches the correct equilibrium position when placed at the interface of a drop without gravity, and a particle pair also recovers the dynamics recorded by experiments as they interact due to capillarity. Herein, we apply this method to multiple Janus particles interacting at a liquid interface in presence of a shear flow. We induce the interfacial shear using a Couette flow

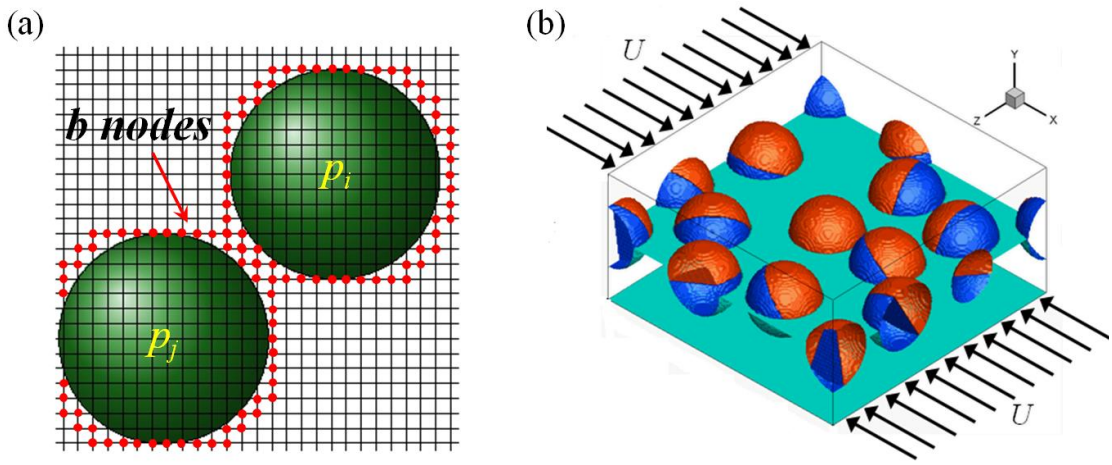

Figure 4.10 (a) Two suspended particles in the lattice domain interacting with the fluid through boundary nodes, (b) 3D view of the lattice domain with multiple Janus spheres under shear.

setup similar to that of the molecular simulations, while the remaining sides of the system are subject to ordinary periodic boundary conditions. The response of a cluster of randomly-oriented Janus particles to shear flow (Figure 4.10(b)) is monitored over the time-scale relevant to the formation of a steady-state configuration. We will address the influence of the flow on inter-particle forces and the formation of structures from Janus spheres. This can reveal the possibility of creating novel self-assembled structures that may not be achieved using Janus particles at stationary interfaces.

4.3.2 Hydrodynamics of a Particle Pair under Interfacial Shear

The simplest case to consider is a two-dimensional problem consisting of a pair of Janus spheres placed in x-y plane initially with upright orientations and a center-to-center separation d_{cc}, as in Figure 4.11. We model 1 μm diameter polyethylene particles with a density of $\rho_p = 925\ kg/m^3$ at a decane-water interface. The particle surface is assumed to be modified such that apolar and polar regions with wettabilities $\theta_a = 120°, \theta_p = 60°$ are obtained. The water and oil densities are $\rho_w = 997\ kg/m^3, \rho_o = 735\ kg/m^3$,

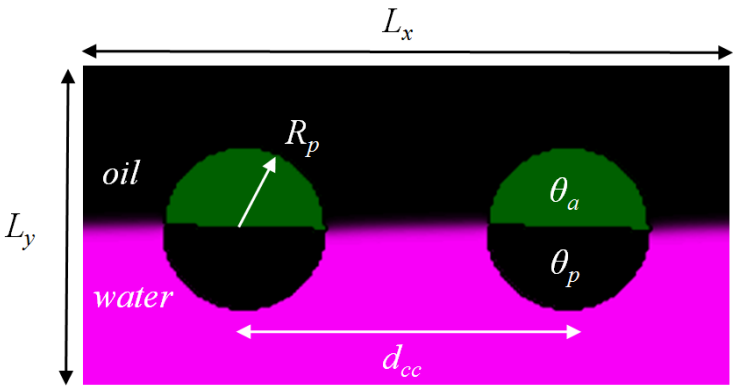

Figure 4.11 Initial configuration of a pair of Janus spheres at a sheared liquid interface.

respectively and the viscosities are reported as $\mu_w = 8.94 \times 10^{-4}\ Pa.s, \mu_o = 9.20 \times 10^{-4}\ Pa.s$. The interfacial tension between the two fluid phases has been measured as $\sigma = 50\ mN/m$. To specify the lattice parameters, we choose $\rho_w = 1, R_p = 25, \sigma = 0.1$. We then match dimensionless numbers to determine the remaining parameters. The dimensionless groups characterizing this problem are: liquid-liquid density ratio ρ_w/ρ_o, viscosity ratio μ_w/μ_o, particle-liquid density ratio ρ_p/ρ_w, and the Ohnesorge number $Oh = \mu_w/\sqrt{\rho_w \sigma R_p}$. Note that the size of the simulation box is $L_x \times L_y \times L_z = 200 \times 100 \times 200$ nodes (which corresponds to $4 \times 2 \times 4\ \mu m$ in physical units), and periodic boundary conditions are applied along *x*, *z* directions. The domain is bounded by solid walls at $y = \pm L_y/2$, and the shear rate can be expressed as $\dot{\gamma} = U/(L_y/2)$ with U being the wall velocity along *x* direction.

The in-plane rotation of the particle θ_z is obtained by integrating the angular velocity ω_z over time. This is shown for the two particles with an initial separation of $d_{cc} = 100$ lattice units in Figure 4.12 at shear rates in the range of $\dot{\gamma} = 0 - 0.002\,\tau^{-1}$, which correspond to $\dot{\gamma} < 1.5 \times 10^7\ s^{-1}$ in physical units for the prescribed system. Larger shear rates could not be achieved as they would exceed the low Mach number limit at which

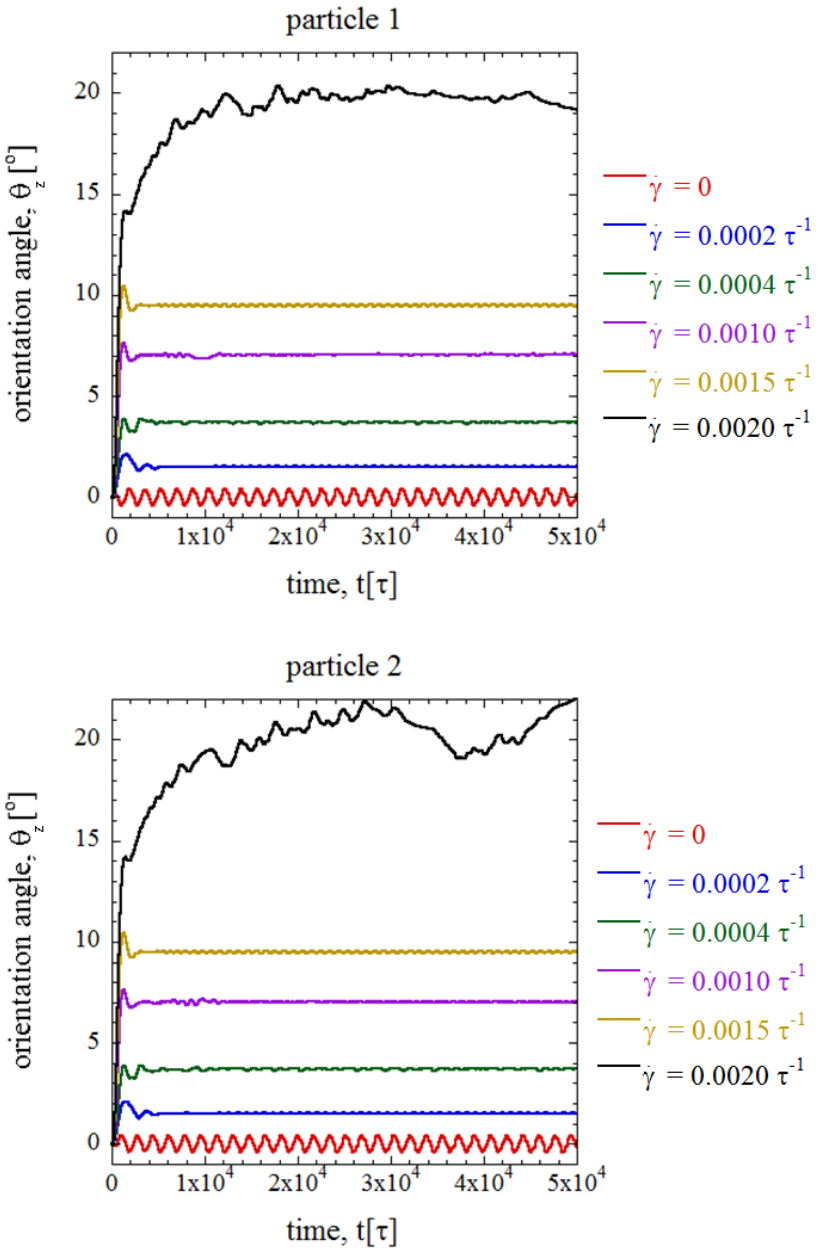

Figure 4.12 Temporal evolution of the orientation angle for a pair of Janus particles initially with upright orientations 100 units apart at an interface subject to different shear rates.

the Lattice-Boltzmann equation is derived. At the stationary interface ($\dot{\gamma} = 0$), the orientation angle is *0°* on average with slight fluctuations, as expected from continuum predictions. At a sheared interface, the particles tilt and quickly approach a steady orientation which is found to be similar for both particles. Note that at the maximum

investigated shear rate, the transient period that takes them to approach the steady orientation is ~20 times longer than that of all lower shear rates.

In order to visualize the interface shape and the interactions between the particles, snapshots of the steady configuration of the system in x-y plane is demonstrated in Figure 4.13 for some sample shear rates. We can see that at the lowest shear rate, the particles barely rotate out of the energetically-favorable upright orientation and the interface deformation is negligible, such that there is no visible capillary-induced interaction and the particles maintain their initial separation. As the shear rate increases, the interface starts to deform more noticeably. Since each particle is subject to an external (clockwise) shear torque, the interface takes a dipolar shape. The overlap of capillary dipoles with similar sign results in repulsion between the particles, which is apparent for $\dot{\gamma} \geq 0.0010\ \tau^{-1}$. The equilibrium inter-particle separation is found to be equal to $L_x/2 = 100$, indicating that the spacing is governed by the periodic boundary condition along x. This was confirmed by placing the particles at different initial spacings in the simulation box

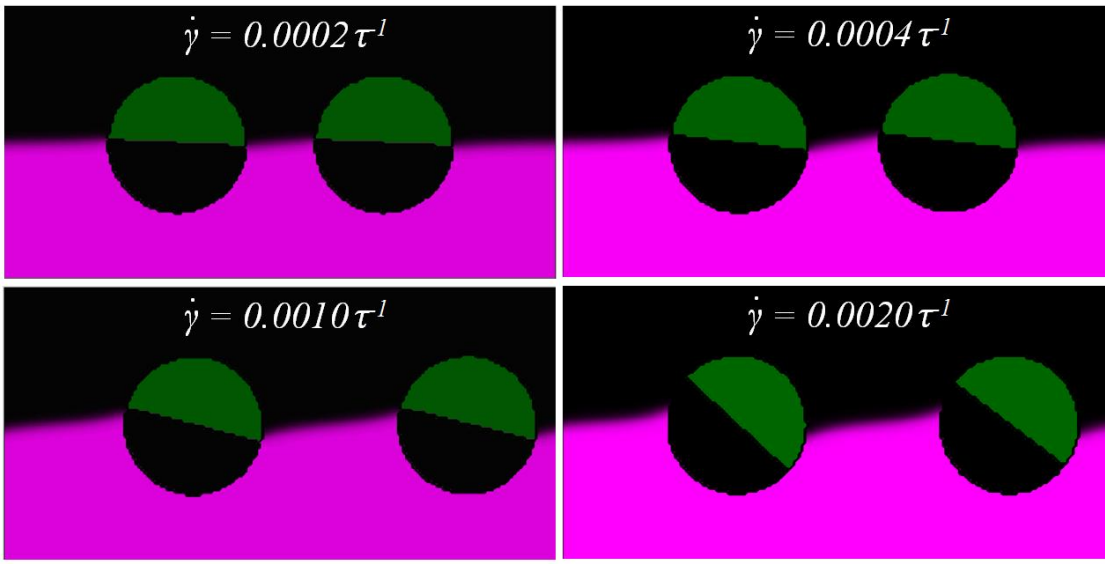

Figure 4.13 Snapshots of the steady-state configuration of a system of two Janus spheres at a liquid interface subject to different shear rates.

and recovering the same steady-state separation. Therefore, an infinite array of Janus spheres with a specific number density in *x-y* plane would induce capillary repulsion under sufficient shear rate until reaching an equal-spaced steady configuration. This can be used as the basis for directing the assembly of a 2D cluster of such particles using interfacial shear flows.

4.3.3 Hydrodynamics and Assembly of Particle Clusters

It was shown in the previous section that Janus particles directed to specific orientations using an interfacial shear flow can interact due to overlap of capillary dipoles and maintain a constant separation depending on their number density. We hypothesized that this might be useful for directing the assembly of a particle cluster at the interface as they are expected to rearrange in order to minimize the total surface energy when neighboring capillary dipoles overlap. Here, a cluster of Janus spheres is created by placing a fixed number of particles with equal size and surface properties at a periodic liquid interface with a grid size of $L_x \times L_z = 200 \times 200$ nodes. We place N Janus particles $1\ \mu m$ in diameter with wettabilities $\theta_a = 120°, \theta_p = 60°$ at random initial positions and orientations at the interface, and monitor their response upon applying a linear shear flow. The surface coverage is defined as the ratio of contact area covered by the particles to the total interface area: $\phi = N\pi R_p^2/(L_x \times L_z)$.

The simulations indicate that a shear rate of $\dot{\gamma} = 0.002\,\tau^{-1}$ is appropriate to induce sufficient particle rotation leading to strong capillary dipoles. At lower shear rates, the orientation is close to upright such that the interface deformation is not significant and considerable interaction cannot be detected between the particles. Figure 4.14 shows the

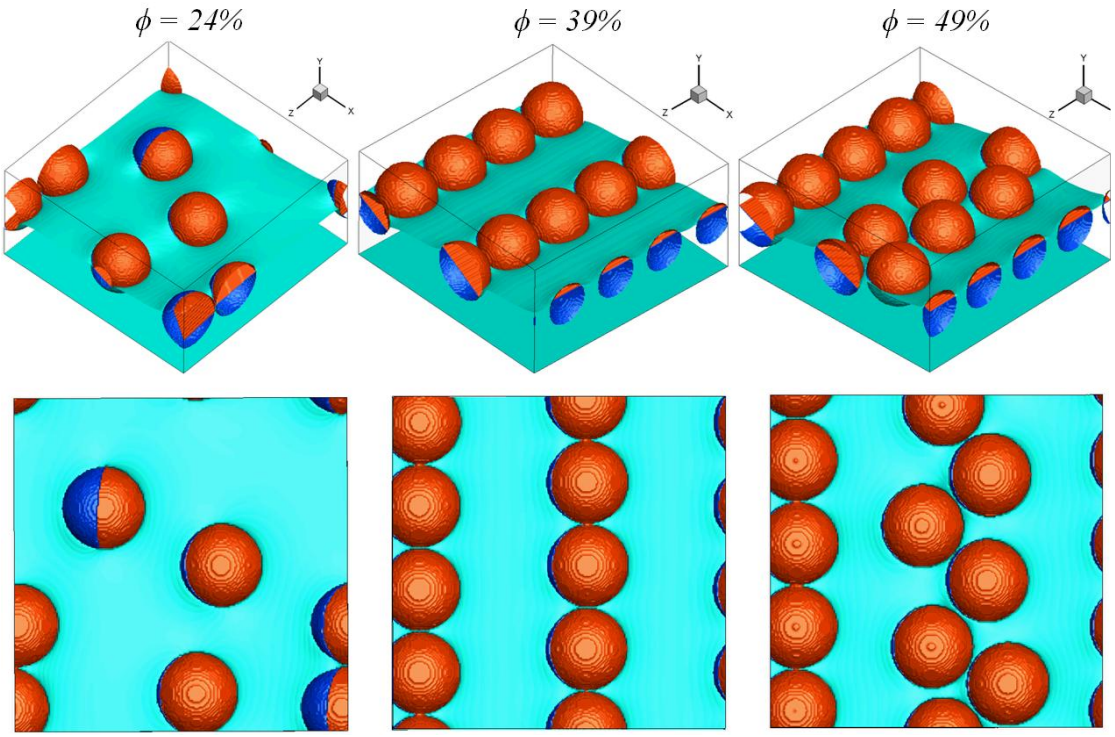

Figure 4.14 Snapshots of the steady-state configuration of a monolayer of Janus spheres with R = 25, β = 60º and different surface coverage ϕ placed initially at random positions and orientations at a periodic interface subject to a shear rate of $\dot{\gamma} = 0.002\ \tau^{-1}$: isometric view (top row) and top-view of the x-z interface plane (bottom row).

steady configuration of the particles at the interface at three sample surface coverage from isometric and top views. In all cases, the particles starting from random orientations undergo 3D rotation approaching similar orientation angles governed by the balance between shear and capillary-induced torques. Moreover, the particles also translate due to the overlap of capillary dipoles attempting to achieve the lowest surface energy state.

At the lowest investigated surface coverage (ϕ = *24%*), there is not much ordering since there is not enough Janus particles and thus sufficient overlapping dipoles to induce an assembled structure. A particle pair is formed probably due to their relatively close initial positions, but the other particles remain basically isolated. Upon increasing the surface coverage, we can see that the particles assemble into two parallel chains along the normal to shear direction. The spacing between these chains is L_x */2 = 100,* which is the

maximum distance over which the particles can repel in this periodic box. As demonstrated in the previous section for a particle pair, imposing a shear flow results in similar orientation angles yielding the overlap of dipoles with similar signs, which induces repulsive capillary forces between the particles. As a result, they tend to approach along the normal to shear direction leading to formation of chains. At higher surface coverage *e.g.* ϕ = *49%*, all the particles cannot fit in the parallel chains such that distorted/staggered arrays are formed as the excess particles try to squeeze in between neighboring dipoles to minimize the surface energy. Note that the general ordering pattern still holds as the particles align normal to shear flow and maintain a separation due to overlap of similar-signed dipoles.

Temporal evolution of the orientation angle of particles for the above case of ϕ = *39%* is shown in Figure 4.15, and we can verify that the equilibrium orientation adopted by all particles is quite close. Note that at higher surface coverage resulting in staggered

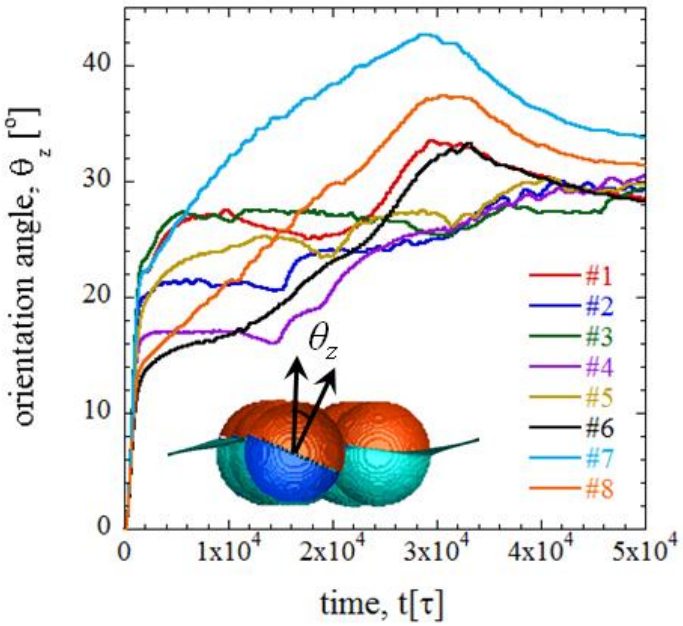

Figure 4.15 Temporal evolution of the orientation angle for a monolayer of Janus particles with a surface coverage of 39% at a liquid interface sheared with $\dot{\gamma} = 0.002\ \tau^{-1}$.

arrays, there might be slight deviation in orientation angles due to the difference in positioning of the particles with respect to neighboring dipoles. The orientation of the particles forming the self-assembled structure can be controlled by tuning the applied shear or particle's surface chemistry. The tilting can generally be increased by increasing the shear rate or reducing the amphiphilicity as proven before for single Janus particles using MD simulations.

To detect the dynamics of particle rearrangement, we traced the particles within the interface plane starting from an initial random distribution. This is shown for the sample case of $\phi = 39\%$ coverage in Figure 4.16(a). The arrows indicate the direction of particle motion over time, and dashed lines represent the locations of two parallel chains formed at equilibrium. We observe that particles #4 and #6 undergo considerable translation along shear direction to align with other particles forming the chains. The positions of all particles remain unchanged after nearly half of the simulation time, indicating an equilibrium configuration minimizing the surface energy.

Figure 4.16(b) shows the velocity of particle #1 along shear direction x as a function of the normal distance of particle's center of mass from the interface at different instants during the simulation. The velocity profile for the linear Couette flow is also plotted for comparison. We can see that the particle shows some deviation from the linear profile, which is attributed to its interactions with multiple other particles present at the interface. The particle is found to accelerate/decelerate at different elevations as the interface shape is modified upon overlap with neighboring dipoles. A similar behavior was observed for other particles in the cluster.

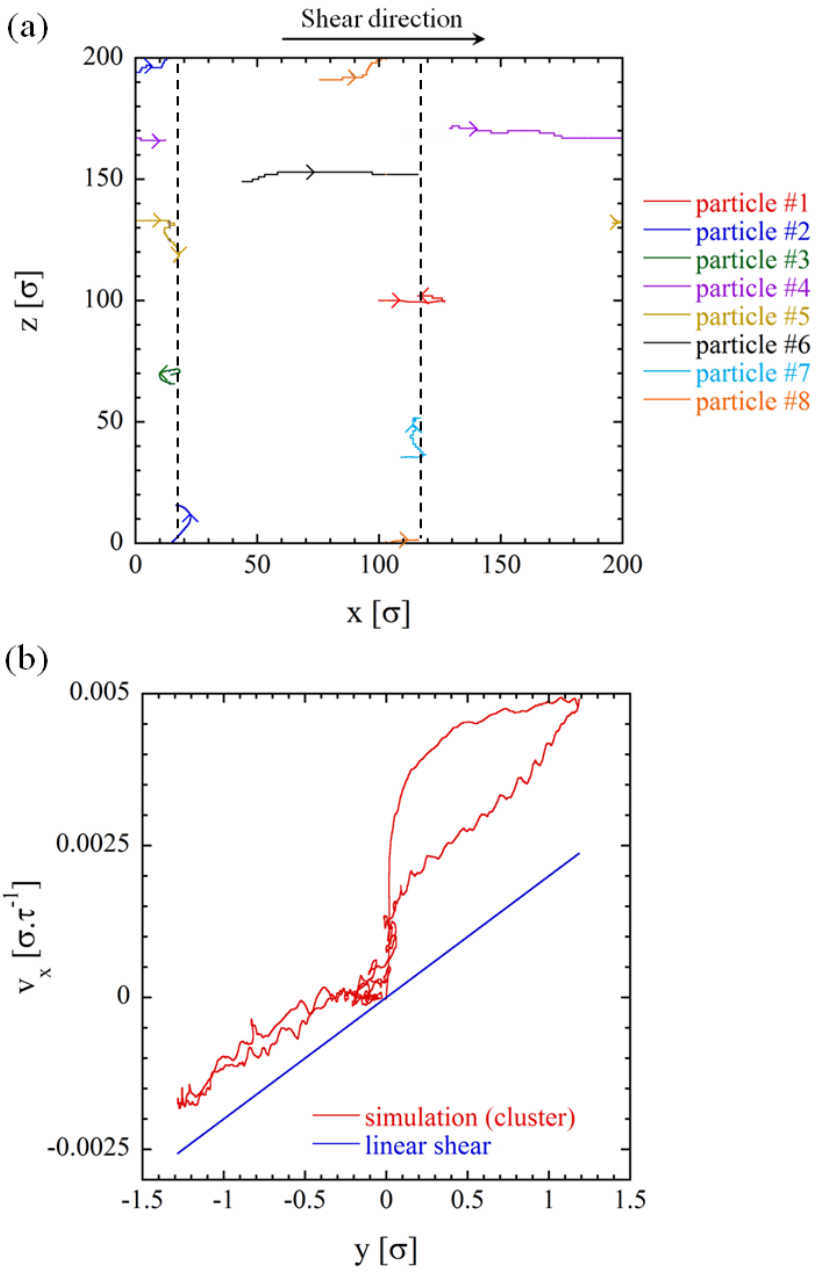

Figure 4.16 (a) Trajectories of particles in a cluster with 39% surface coverage at an interface sheared with $\dot{\gamma} = 0.002\ \tau^{-1}$ until reaching equilibrium, (b) velocity component along shear direction for a sample particle in the cluster as a function of its normal distance from the interface plane.

In order to quantify the ordering induced by superposition of capillary dipoles subject to shear flow, we define an order parameter based on the degree of particle alignment in *z*-direction. For any particle *i*, all its nearest neighbors *j* are found; then, the unit vector

connecting these particles $\boldsymbol{u}_{ij}$ is built and its deviation from the expected direction of ordering $\boldsymbol{u}_d = \hat{k}$ is calculated. The order parameter for particle *i* with all nearest neighbors *j* is defined as

$$S_i = \frac{1}{j}\sum_j |\boldsymbol{u}_{ij}.\boldsymbol{u}_d| = \langle |\boldsymbol{u}_{ij}.\boldsymbol{u}_d| \rangle \tag{4.11}$$

The overall order parameter of the system is then obtained by averaging over all particles

$$S = \frac{1}{N}\sum_{i=1}^{N} S_i = \frac{1}{N}\sum_{i=1}^{N}\langle |\boldsymbol{u}_{ij}.\boldsymbol{u}_d| \rangle = \frac{1}{N}\sum_{i=1}^{N}\langle |\cos(\theta_{ij})| \rangle \tag{4.12}$$

where *N* is the number of particles in the domain, θ_{ij} is the angle formed between the vector connecting two neighboring particles *i,j* and the order direction $\hat{k}$, and the brackets indicate averaging over all nearest neighbors *j* around particle *i*. A similar approach has been used in the literature for quantifying the preferred assembly of particles in a specific direction *e.g.* for orientation of rod blocks forming aggregates in a mixture of rod-coil block copolymers and rigid homopolymers [123].

The steady-state snapshots of the system were analyzed to determine the degree of ordering following this definition. The calculated order parameter is shown in Figure 4.17 as a function of the surface coverage. We can see that the case with ϕ = *39%* which corresponds to the ideal situation leading to two perfectly aligned arrays gives the maximum order parameter of *S = 1*. As we increase the surface coverage beyond this point, the excess particles distort the arrays and eventually lead to a staggered structure thus yielding a reduction in *S*. Note that increasing ϕ even more results in the particles barely having room to rearrange, such that the effective ordering would depend on the initial positioning of the particles. At ϕ < *39%*, the parallel chains cannot be formed such that a some particles remain isolated. The order parameter quickly drops in such sparse

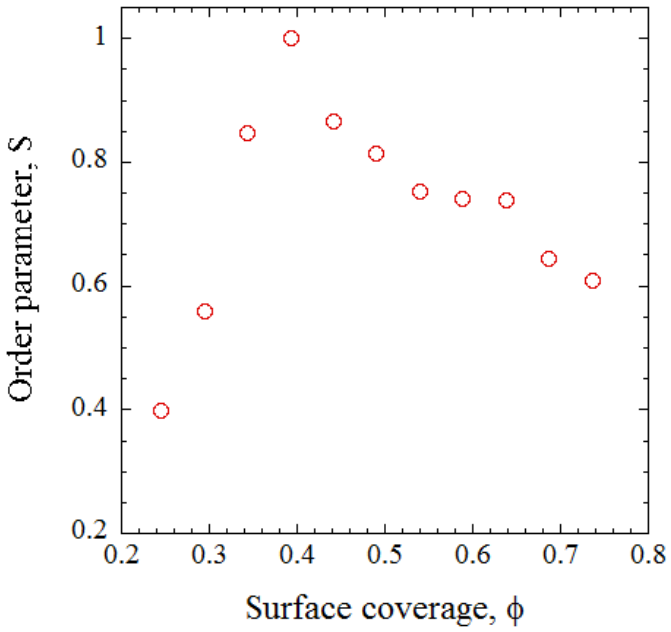

Figure 4.17 The order parameter for the steady-state structure formed by a monolayer of Janus particles with different surface coverage at a liquid interface sheared with $\dot{\gamma} = 0.002\ \tau^{-1}$.

coverage and would be generally influenced by their ability to form pairs of dipoles. Overall, we can conclude that the ideal case with ϕ = *39%* yields the best ordering of particles into parallel chains, while any deviation from this surface coverage results in reduced order as either the excess particles distort the arrays or particles remain isolated without a specific directional preference. An intermediate window of $0.34 < \phi < 0.50$ is found to give effective ordering with $S > 0.8$.

4.3.4 Additional Considerations on Directed Assembly

The previous section revealed the possibility of assembling a randomly positioned/oriented cluster of Janus particles at a liquid interface into an ordered structure upon applying proper shear flow. The first question that may arise is whether the observed ordering depends on the initial position and/or orientation of the particles. In

order to verify this, two sets of trials were devised at each surface coverage. In the first set, the particles start from the same random positions as before but their orientation is changed either to upright or a different random sequence. In the second set, the particles are placed at different random positions at the interface by using several random seed initializations. It was found that at intermediate surface coverage corresponding to the ordered region in Figure 4.17 ($0.34 < \phi < 0.50$), although the dynamics and the relaxation time before reaching the self-assembled structure varies, the final configuration is similar irrespective of the initial position/orientation of the particles. However, the final configuration outside this range varies depending on the initial spacing between the particles.

The second important question is whether the assembly observed in the periodic box can truly represent the behavior of a particle cluster on an actual planar interface. To verify this, a domain-size independency test is performed by creating a larger interface as the lengths of the box along the interface plane are doubled from $L_x = L_z = 100$ to 200. The number of particles in each case is multiplied by 4 in order to recover the same surface coverage, and their dynamics is monitored until reaching the steady configuration. The initial and final structure at a sample surface coverage of $\phi = 39\%$ in this larger domain is shown in Figure 4.18. We can clearly see that the particles form four parallel chains each containing 8 particles in the periodic box. Moreover, tracking the rotational dynamics of the particles reveals approaching similar orientation angles as those measured in the smaller domain. A similar behavior was found at other ϕ within the ordered window of surface coverage. Therefore, the assembly is found to be independent

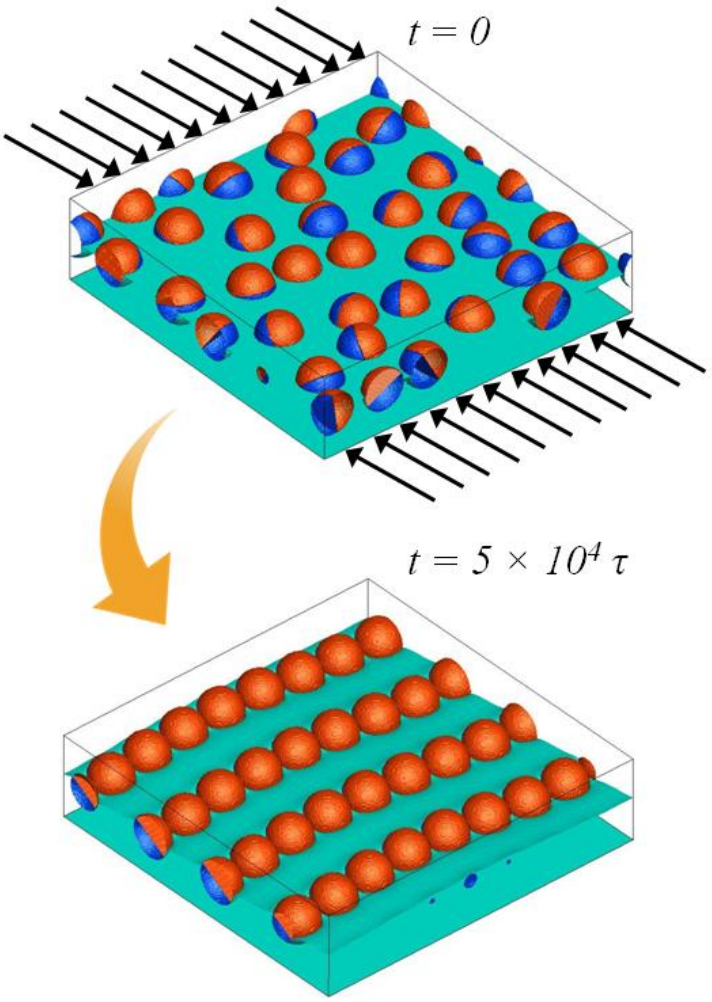

Figure 4.18 Snapshots of a system of Janus spheres with 39% surface coverage at a periodic interface with increased domain size subject to a shear rate of $\dot{\gamma} = 0.002\,\tau^{-1}$ at two different time-steps.

of the domain size and we can conclude that the particles would behave similarly at an actual liquid interface with equivalent surface coverage.

The third question is whether the particles can maintain the ordered structure when the shear flow is switched off. It is known that the greatest disadvantage of external fields to direct the assembly is that once they are removed, the crystals generally melt back into disorder [105]. In the proposed approach where the assembly is induced by combining the liquid interface as a template with a hydrodynamic flow, the capillary dipoles will disappear once the flow is removed. The question is whether the chains will then

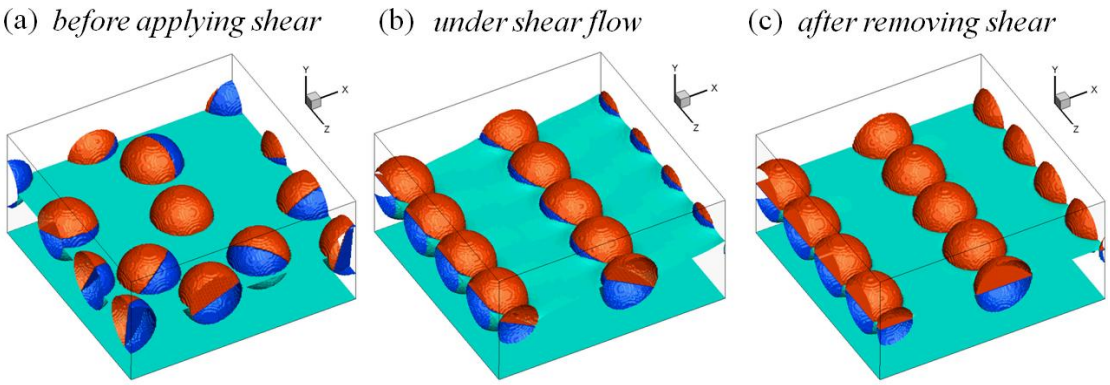

Figure 4.19 Snapshots of a system of Janus spheres with 39% surface coverage subject to an interfacial shear rate of $\dot{\gamma} = 0.002\ \tau^{-1}$: (a) initial random configuration, (b) the ordered structure upon applying the shear flow, (c) the steady-state structure after removing the flow.

disintegrate recovering the initial disordered structure. To answer this question, the flow field is removed after reaching the steady-state configuration ($t = 5 \times 10^4\ \tau$) and the dynamics is monitored for an extended period. Snapshots of the system at different stages are shown in Figure 4.19 for the sample case of *39%* surface coverage. The particles initially placed with random positions and orientations order into parallel chains upon applying the shear flow. When the field is turned off, all particles rotate around *z*-axis towards the upright orientation (as expected), but interestingly, they chains are preserved and are only slightly displaced together along *–x* (note the change in orientation from $\theta_{eq} \approx 29^o$ to upright and the slight shift to the left compared to the configuration under shear). When the particles go back to upright, the interface also becomes flat as there is no heterogeneity along the contact line anymore. As a result, a flat liquid interface is achieved at which Janus particles form a highly-ordered structure. There is no means of further interaction between the particles as we only consider capillary-induced forces, thus yielding no further change in structure over time. This interesting finding can make the proposed assembly method practical when other types of interaction *e.g.* electrostatic repulsion are negligible.

Lastly, we investigated how the assembly is affected in presence of particles with different sizes. To evaluate this, we modeled a bidisperse distribution consisting of 1 μm and 0.5 μm diameter particles with equal number density at the interface. The particles are initially placed with random positions and orientations, while a shear rate of $\dot{\gamma} = 0.002\,\tau^{-1}$ is applied as in the monodisperse case. The steady-state configuration of particles at the interface is shown in Figure 4.20 at three sample surface coverage. At ϕ = *25%*, there is no clear assembly and the particles mostly remain isolated due to lack of sufficient number of dipoles. The equilibrium orientations of the two particle types are found to be different: θ_{eq} = *18º, 29º* for the small and large particles. The ratio of the shear to capillary torque grows with increasing particle size, yielding an enhanced tilt. This, in turn, indicates the presence of weaker capillary dipoles around smaller particles, resulting in shorter-range interactions and reduced tendency to interact and assemble under a fixed shear rate. At a surface coverage of *37%*, there are enough dipoles that can superpose and yield a self-assembled structure. We can clearly see that the particles tend to form chains along the normal to shear direction although the chains are slightly distorted since they result from the overlap of dipoles with different strengths.

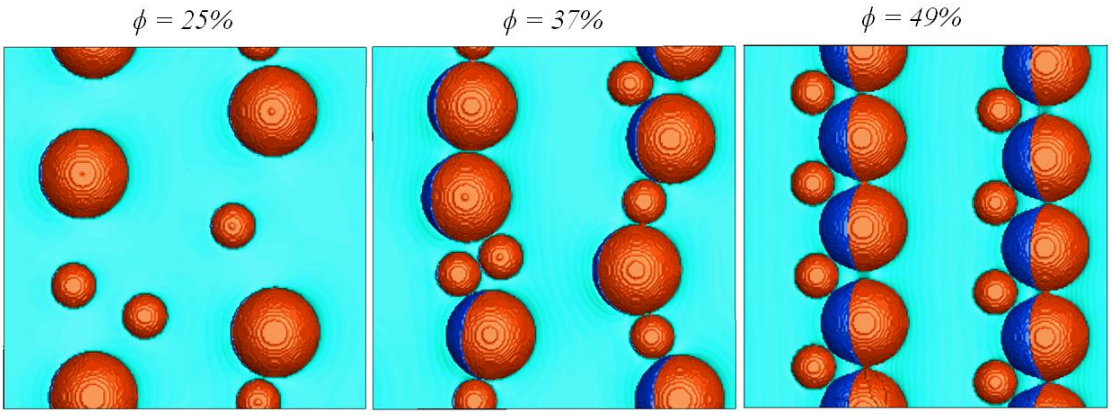

Figure 4.20 Top-view snapshots of the steady-state configuration of a bidisperse monolayer of Janus spheres and different surface coverage ϕ subject to a shear rate of $\dot{\gamma} = 0.002\,\tau^{-1}$.

As the surface coverage is further increased to *49%*, the large particles form parallel chains and force the small ones to fit in between their dipoles. As a result, a symmetric ordered structure is obtained, but the large particles are significantly more tilted compared to the monodisperse case with equal number density as a result of the overlap with smaller dipoles. If we further increase the surface coverage beyond this point, our simulations indicate that all the particles cannot fit in the chains and lead to their distortion and reduced ordering. This is similar to the principles governing the assembly for a monodisperse layer of Janus spheres. Overall, we detect an intermediate window of surface coverage at which effective ordering can be achieved; this range is almost independent of the particle size and is based on the particle density sufficient to induce strong capillary interactions, while not too large to prevent particle rearrangement.

4.4 Summary: Interfacial Hydrodynamics under Shear Flow

In this chapter, the hydrodynamics of Janus particles under interfacial shear flows was studied from two different aspects: (1) how does a single Janus particle respond to interfacial shear? (2) can we use the flow to direct the assembly of multiple particles at the interface? Based on the lengthscale and timescale required to detect the dynamics/assembly, atomistic/mesoscopic approaches were adopted for these two problems, respectively.

Molecular Dynamics simulation of isolated particles revealed that depending on particle's shape and amphiphilicity as well as the applied shear rate, two different rotational dynamics can occur: smooth tilt and tumbling. These regimes were justified based on free energy change between different states relative to thermal energy.

Moreover, it was shown that irrespective of the dynamics regime, a steady orientation is eventually achieved due to the balance between the shear-induced and capillary torques. Maps of attainable orientations were constructed to enable predicting the final configuration as a function of particle shape, surface chemistry, and flow parameters.

Lattice-Boltzmann simulation of the collective behavior of a cluster of Janus particles at a liquid interface revealed the possibility of assembling them into ordered structures under appropriate conditions. At an intermediate window of surface coverage under shear rates resulting in strong capillary dipoles, the overlap of interface deformations yields repulsive forces which induce the formation of particle chains along the normal to shear direction. Increasing the surface coverage can result in reduced spacing between these chains or formation of distorted/staggered chains, while lower coverage yield isolated particles. The ordered structure is preserved after removing the flow field as the particles only rotate to upright orientations without a tendency to disintegrate. As a result, this approach which combines three directed assembly methods namely the Janus character, the liquid interface, and the hydrodynamic flow, can enable directing a randomly-oriented set of Janus particles into an ordered structure with controllable properties.

Chapter 5

Conclusions and Outlook

This research revealed some important unknown aspects of the interfacial orientation, dynamics, and assembly of amphiphilic Janus particles. We first carried out a quasi-static analysis on the equilibrium orientation and capillary-induced forces between Janus particles of different geometry and surface chemistry. It was demonstrated that Janus spheres with tilted orientations give rise to dipolar capillary interactions, where the particles adjust their relative orientation to create a capillary bridge resulting in their attraction until contact. We showed how breaking the symmetry in distribution of the two regions may enhance the degree of surface activity. For a more intricate design with two spherical caps patterned symmetrically on the particle, it was found that the preferred orientation strongly depends on the wettability of two surface regions, as well as the size of the patches relative to the whole particle. We demonstrated the conditions at which the particles flip from a parallel-patch to normal-patch orientation, leading to quadrupolar capillary interactions between neighboring particles. For Janus ellipsoids, the added shape anisotropy further complicates the interface shape leading to capillary hexapoles. We found that neighboring ellipsoids align side-by-side at equilibrium, and the capillary force and torque in contact can be enhanced upon increasing the amphiphilicity.

In the second part, we investigated the thermal motion of a single Janus particle at a fluid interface and provided a quantitative analysis on its translational and rotational diffusion. It was shown that the interfacial diffusion is not only a function of particle size, but also depends on its surface chemistry. Both the in-plane translational and rotational diffusion become slower upon increasing the amphiphilicity due to the formation of a denser fluid layer around the particle, thus increasing the resistance against motion due to an increased effective particle size. We also elaborated on the effects of particle size, fluid density, and surface tension on the interfacial diffusivity. It was shown that the diffusivity becomes slower with increasing particle size, but the decay rate is faster than that in a bulk fluid predicted by the Stokes-Einstein theory. Moreover, we showed that the effect of amphiphilicity on diffusion coefficients diminishes with increasing fluid density, while increased surface tension can only slightly reduce the diffusivity.

In the third part of this research, we discussed how dynamics of such particles are influenced in presence of a shear flow at the interface. The response of an isolated Janus particle to interfacial shear revealed that depending on its shape and amphiphilicity as well as the applied shear rate, two unique rotational dynamics can occur: smooth tilt and tumbling. These regimes were justified based on free energy change between different states in comparison with thermal fluctuations energy. Moreover, we found that the particles eventually approach a steady orientation due to the balance between the shear-induced and capillary torques. Maps of attainable orientations were constructed enabling the prediction of the final configuration of Janus particles subject to a range of shear rates. We then performed a mesoscopic analysis to investigate the collective behavior of a cluster of such particles at sheared interfaces. It was shown that at an intermediate range

of surface coverage using shear rates resulting in strong capillary dipoles, the particles can be assembled into ordered structures. The overlap of interface deformations yields the formation of particle chains along the normal to shear direction. The interesting feature of this directed assembly method is that the ordered structure is preserved after removing the flow field as the particles only rotate to upright orientations without a tendency to disintegrate the chains. Therefore, this approach can be successful in practical situations particularly when other types of interaction are negligible.

Our analysis clearly shows that the configuration of individual Janus particles influences the interface profile and thus the lateral interactions between multiple particles, which, in turn, can affect the structure and properties of particle monolayers. Ultimately, this will have a significant impact on their efficacy as solid surfactants. Therefore, it is crucial to obtain a better understanding of the dynamics of the adsorption process of these particles to interfaces. Moreover, their shape anisotropy provides an additional degree of freedom enabling the control over their surface activity. There is still the lack of a reliable theory incorporating the combined effect of chemical and geometrical anisotropy on the interface shape around such particles. On the other hand, considering recent advances in fabrication of Janus particles with various geometry, further research is required to quantify and compare the surface activity of particles with more complex shapes *e.g.* multi-block and hollow particles. Detail analysis of their interaction, alignment, and stability is required to determine their effectiveness as particulate surfactants. Another important factor to consider is the effect of interface curvature on their interfacial behavior, which deserves a more in-depth investigation in the future.

Analyzing the interfacial diffusion of Janus particles warrants further research incorporating the effects of particle geometry and pair diffusion properties. Coarse-grained simulation methods including Dissipative Particle Dynamics (DPD) can be helpful in achieving information over larger lengthscales. On the other hand, the response of particles to different variations of hydrodynamic flows *e.g.* asymmetric shear or elongational flow needs to be evaluated in order to predict possible scenarios in various actual settings. A more thorough analysis is required on the mechanism governing the tumbling motion of Janus particles and how one can suppress such dynamics.

Moreover, the community would greatly benefit from studies concerning the collective behavior of Janus particles at fluid interfaces. Namely, the rheological properties of Janus particle monolayers, which likely depend on the lateral interactions between particles and the microstructure of monolayers, are expected to have a significant impact on the effectiveness of Janus particles as stabilizing agents. Although an interfacial shear flow was shown to tune the structure of particle clusters and order them into specific chains, its ability to control the interfacial tension and rheological properties is still unclear. Furthermore, more complex geometries including rods/ellipsoids can yield a variety of self-assembled structures due to changes in the interface shape and relative strength of multipole terms. It should be emphasized that while significant advances have been made in understanding the interfacial behavior of Janus particles using theory and experiment, more computational approaches to simulate their dynamics can be invaluable for their efficient use in particle-laden systems.

References

1. Adams, D.J., et al., *Influence of particle surface roughness on the behaviour of Janus particles at interfaces.* Colloids and Surfaces A-Physicochemical and Engineering Aspects, 2008. **317**(1-3): p. 360-365.
2. Sanchez, C., et al., *"Chimie douce": A land of opportunities for the designed construction of functional inorganic and hybrid organic-inorganic nanomaterials.* Comptes Rendus Chimie, 2010. **13**(1-2): p. 3-39.
3. Glotzer, S.C. and M.J. Solomon, *Anisotropy of building blocks and their assembly into complex structures.* Nature Materials, 2007. **6**(8): p. 557-562.
4. Loget, G. and A. Kuhn, *Bulk synthesis of Janus objects and asymmetric patchy particles.* Journal of Materials Chemistry, 2012. **22**(31): p. 15457-15474.
5. Hu, J., et al., *Fabrication, properties and applications of Janus particles.* Chemical Society Reviews, 2012. **41**(11): p. 4356-4378.
6. Lattuada, M. and T.A. Hatton, *Synthesis, properties and applications of Janus nanoparticles.* Nano Today, 2011. **6**(3): p. 286-308.
7. Pawar, A.B. and I. Kretzschmar, *Fabrication, Assembly, and Application of Patchy Particles.* Macromolecular Rapid Communications, 2010. **31**(2): p. 150-168.
8. Walther, A. and A.H.E. Mueller, *Janus particles.* Soft Matter, 2008. **4**(4): p. 663-668.
9. Lee, K.J., J. Yoon, and J. Lahann, *Recent advances with anisotropic particles.* Current Opinion in Colloid & Interface Science, 2011. **16**(3): p. 195-202.
10. Perro, A., et al., *Design and synthesis of Janus micro- and nanoparticles.* Journal of Materials Chemistry, 2005. **15**(35-36): p. 3745-3760.
11. Du, J. and R.K. O'Reilly, *Anisotropic particles with patchy, multicompartment and Janus architectures: preparation and application.* Chemical Society Reviews, 2011. **40**(5): p. 2402-2416.
12. De Gennes, P.G., *Soft Matter Nobel Lecture.* Angewandte Chemie International Edition in English, 1992. **31**(7): p. 842-845.
13. Walther, A. and A.H.E. Mueller, *Janus Particles: Synthesis, Self-Assembly, Physical Properties, and Applications.* Chemical Reviews, 2013. **113**(7): p. 5194-5261.
14. Bhaskar, S., et al., *Engineering, Characterization and Directional Self-Assembly of Anisotropically Modified Nanocolloids.* Small, 2011. **7**(6): p. 812-819.
15. Ding, H.-m. and Y.-q. Ma, *Interactions between Janus particles and membranes.* Nanoscale, 2012. **4**(4): p. 1116-1122.
16. Gkeka, P., L. Sarkisov, and P. Angelikopoulos, *Homogeneous Hydrophobic-Hydrophilic Surface Patterns Enhance Permeation of Nanoparticles through Lipid Membranes.* Journal of Physical Chemistry Letters, 2013. **4**(11): p. 1907-1912.
17. Wang, F., et al., *Dual Surface-Functionalized Janus Nanocomposites of Polystyrene/Fe3O4@SiO2 for Simultaneous Tumor Cell Targeting and Stimulus-Induced Drug Release.* Advanced Materials, 2013. **25**(25): p. 3485-3489.

18. Bucaro, M.A., et al., *Tunable Liquid Optics: Electrowetting-Controlled Liquid Mirrors Based on Self-Assembled Janus Tiles.* Langmuir, 2009. **25**(6): p. 3876-3879.
19. Faria, J., M.P. Ruiz, and D.E. Resasco, *Phase-selective catalysis in emulsions stabilized by Janus silica-nanoparticles.* Advanced Synthesis & Catalysis, 2011. **352**: p. 2359-2364.
20. Erhardt, R., et al., *Janus micelles.* Macromolecules, 2001. **34**(4): p. 1069-1075.
21. Walther, A., A. Goeldel, and A.H.E. Mueller, *Controlled crosslinking of polybutadiene containing block terpolymer bulk structures: A facile way towards complex and functional nanostructures.* Polymer, 2008. **49**(15): p. 3217-3227.
22. Walther, A., et al., *Self-Assembly of Janus Cylinders into Hierarchical Superstructures.* Journal of the American Chemical Society, 2009. **131**(13): p. 4720-4728.
23. Walther, A., et al., *Janus discs.* Journal of the American Chemical Society, 2007. **129**(19): p. 6187-6198.
24. Walther, A., M. Drechsler, and A.H.E. Mueller, *Structures of amphiphilic Janus discs in aqueous media.* Soft Matter, 2009. **5**(2): p. 385-390.
25. Lattuada, M. and T.A. Hatton, *Preparation and controlled self-assembly of janus magnetic nanoparticles.* Journal of the American Chemical Society, 2007. **129**(42): p. 12878-12889.
26. Pradhan, S., L.-P. Xu, and S. Chen, *Janus nanoparticles by interfacial engineering.* Advanced Functional Materials, 2007. **17**(14): p. 2385-2392.
27. Nie, L., et al., *One-pot synthesis of amphiphilic polymeric Janus particles and their self-assembly into supermicelles with a narrow size distribution.* Angewandte Chemie-International Edition, 2007. **46**(33): p. 6321-6324.
28. Isojima, T., et al., *Reversible clustering of pH- and temperature-responsive Janus magnetic nanoparticles.* Acs Nano, 2008. **2**(9): p. 1799-1806.
29. Binks, B.P. and P.D.I. Fletcher, *Particles adsorbed at the oil-water interface: A theoretical comparison between spheres of uniform wettability and "Janus" particles.* Langmuir, 2001. **17**(16): p. 4708-4710.
30. Hirose, Y., S. Komura, and Y. Nonomura, *Adsorption of Janus particles to curved interfaces.* Journal of Chemical Physics, 2007. **127**(5).
31. Nonomura, Y., S. Komura, and K. Tsujii, *Adsorption of disk-shaped Janus beads at liquid-liquid interfaces.* Langmuir, 2004. **20**(26): p. 11821-11823.
32. Glaser, N., et al., *Janus particles at liquid-liquid interfaces.* Langmuir, 2006. **22**(12): p. 5227-5229.
33. Zheng, Z., et al., *Janus Nanomembranes: A Generic Platform for Chemistry in Two Dimensions.* Angewandte Chemie-International Edition, 2010. **49**(45): p. 8493-8497.
34. Kim, S.-H., S.Y. Lee, and S.-M. Yang, *Janus Microspheres for a Highly Flexible and Impregnable Water-Repelling Interface.* Angewandte Chemie-International Edition, 2010. **49**(14): p. 2535-2538.
35. Walther, A., K. Matussek, and A.H.E. Mueller, *Engineering nanostructured polymer blends with controlled nanoparticle location using Janus particles.* Acs Nano, 2008. **2**(6): p. 1167-1178.

36. Walther, A., M. Hoffmann, and A.H.E. Mueller, *Emulsion polymerization using Janus particles as stabilizers.* Angewandte Chemie-International Edition, 2008. **47**(4): p. 711-714.
37. Park, B.J. and D. Lee, *Equilibrium Orientation of Nonspherical Janus Particles at Fluid-Fluid Interfaces.* Acs Nano, 2012. **6**(1): p. 782-790.
38. Park, B.J., T. Brugarolas, and D. Lee, *Janus particles at an oil-water interface.* Soft Matter, 2011. **7**(14): p. 6413-6417.
39. Park, B.J. and D. Lee, *Configuration of nonspherical amphiphilic particles at a fluid-fluid interface.* Soft Matter, 2012. **8**(29): p. 7690-7698.
40. Drexler, S., et al., *Amphiphilic Nanohybrid Catalysts for Reactions at the Water/Oil Interface in Subsurface Reservoirs.* Energy & Fuels, 2012. **26**(4): p. 2231-2241.
41. Shchukina, E.M. and D.G. Shchukin, *Layer-by-layer coated emulsion microparticles as storage and delivery tool.* Current Opinion in Colloid & Interface Science, 2012. **17**(5): p. 281-289.
42. Tu, F., B.J. Park, and D. Lee, *Thermodynamically Stable Emulsions Using Janus Dumbbells as Colloid Surfactants.* Langmuir, 2013. **29**(41): p. 12679-12687.
43. Yan, L.-T., et al., *Self-Assembly of Janus Nanoparticles in Diblock Copolymers.* Acs Nano, 2010. **4**(2): p. 913-920.
44. Casagrande, C., et al., *Janus beads: Realization and behaviour at water/oil interfaces.* Europhysics Letters, 1989. **9**(3): p. 251-255.
45. Casagrande, C. and M. Veyssie, *Janus beads: Realization and 1st observation of interfacial properties.* Comptes Rendus De L Academie Des Sciences Serie Ii, 1988. **306**(20): p. 1423-1425.
46. Ondarcuhu, T., et al., *Specific properties of amphiphilic particles at fluid interfaces.* Journal De Physique, 1990. **51**(14): p. 1527-1536.
47. Li, X., J.D. Gunton, and A. Chakrabarti, *A simple model of directional interactions for proteins.* J. Chem. Phys., 2009. **131**(11): p. DOI: 10.1063/1.3227041.
48. Giacometti, A., et al., *Effects of patch size and number within a simple model of patchy colloids.* J. Chem. Phys., 2010. **132**(17): p. DOI: 10.1063/1.3415490.
49. Romano, F. and F. Sciortino, *Two dimensional assembly of triblock Janus particles into crystal phases in the two bond per patch limit.* Soft Matter, 2011. **7**(12): p. 5799-5804.
50. Zhang, L., et al., *Magnetic colloidosomes fabricated by Fe3O4-SiO2 hetero-nanorods.* Soft Matter, 2011. **7**(16): p. 7375-7381.
51. Botto, L., et al., *Capillary interactions between anisotropic particles.* Soft Matter, 2012. **8**(39): p. 9957-9971.
52. Grzybowski, B.A., et al., *Modeling of menisci and capillary forces from the millimeter to the micrometer size range.* Journal of Physical Chemistry B, 2001. **105**(2): p. 404-412.
53. Brakke, K.A., *The surface evolver and the stability of liquid surfaces.* Philosophical Transactions of the Royal Society of London Series a-Mathematical Physical and Engineering Sciences, 1996. **354**(1715): p. 2143-2157.
54. Lewandowski, E.P., et al., *Orientation and Self-Assembly of Cylindrical Particles by Anisotropic Capillary Interactions.* Langmuir, 2010. **26**(19): p. 15142-15154.

55. Hurd, A.J., *The electrostatic interaction between interfacial colloidal particles.* Journal of Physics a-Mathematical and General, 1985. **18**(16): p. 1055-1060.
56. Pieranski, P., *Two-dimensional interfacial colloidal crystals.* Physical Review Letters, 1980. **45**: p. 569-572.
57. Stamou, D., C. Duschl, and D. Johannsmann, *Long-range attraction between colloidal spheres at the air-water interface: The consequence of an irregular meniscus.* Phys. Rev. E, 2000. **62**(4): p. 5263-5272.
58. Romano, F., E. Sanz, and F. Sciortino, *Crystallization of tetrahedral patchy particles in silico.* Journal of Chemical Physics, 2011. **134**(17).
59. Saika-Voivod, I., F. Romano, and F. Sciortino, *Nucleation barriers in tetrahedral liquids spanning glassy and crystallizing regimes.* J. Chem. Phys., 2011. **135**(12): p. DOI: 10.1063/1.3638046.
60. Bianchi, E., et al., *Theoretical and numerical study of the phase diagram of patchy colloids: Ordered and disordered patch arrangements.* J. Chem. Phys., 2008. **128**(14): p. DOI: 10.1063/1.2888997.
61. Bianchi, E., et al., *Phase diagram of patchy colloids: Towards empty liquids.* Phys. Rev. Lett., 2006. **97**(16): p. DOI: 10.1103/PhysRevLett.97.168301.
62. Rezvantalab, H. and S. Shojaei-Zadeh, *Designing patchy particles for optimum interfacial activity.* Physical Chemistry Chemical Physics, 2014. **16**(18): p. 8283-8293.
63. Lehle, H., E. Noruzifar, and M. Oettel, *Ellipsoidal particles at fluid interfaces.* Eur. Phys. J. E, 2008. **26**(1-2): p. 151-160.
64. Kralchevsky, P.A. and K. Nagayama, *Capillary interactions between particles bound to interfaces, liquid films and biomembranes.* Adv. Colloid Interface Sci., 2000. **85**(2-3): p. 145-192.
65. Grzybowski, B.A., et al., *Modeling of menisci and capillary forces from the millimeter to the micrometer size range.* J. Phys. Chem. B, 2001. **105**(2): p. 404-412.
66. Rezvantalab, H. and S. Shojaei-Zadeh, *Capillary interactions between spherical Janus particles at liquid-fluid interfaces.* Soft Matter, 2013. **9**(13): p. 3640-3650.
67. Kim, J.-W., R.J. Larsen, and D.A. Weitz, *Synthesis of nonspherical colloidal particles with anisotropic properties.* J. Am. Chem. Soc., 2006. **128**(44): p. 14374-14377.
68. Lee, D. and D.A. Weitz, *Nonspherical Colloidosomes with Multiple Compartments from Double Emulsions.* Small, 2009. **5**(17): p. 1932-1935.
69. Zhang, Z., et al., *Synthesis and Directed Self-Assembly of Patterned Anisometric Polymeric Particles.* J. Am. Chem. Soc., 2011. **133**(3): p. 392-395.
70. Keville, K.M., E.I. Franses, and J.M. Caruthers, *Preparation and characterization of monodisperse polymer microspheroids.* Journal of Colloid and Interface Science, 1991. **144**(1): p. 103-126.
71. Ho, C.C., et al., *Preparation of monodisperse ellipsoidal polystyrene particles.* Colloid and Polymer Science, 1993. **271**(5): p. 469-479.
72. Forster, J.D., et al., *Assembly of Optical-Scale Dumbbells into Dense Photonic Crystals.* Acs Nano, 2011. **5**(8): p. 6695-6700.
73. Chen, Q., et al., *Supracolloidal Reaction Kinetics of Janus Spheres.* Science, 2011. **331**(6014): p. 199-202.

74. Botto, L., et al., *Capillary bond between rod-like particles and the micromechanics of particle-laden interfaces.* Soft Matter, 2012. **8**(18): p. 4971-4979.
75. Loudet, J.C., et al., *Capillary interactions between anisotropic colloidal particles.* Physical Review Letters, 2005. **94**(1).
76. Rezvantalab, H. and S. Shojaei-Zadeh, *Role of Geometry and Amphiphilicity on Capillary-Induced Interactions between Anisotropic Janus Particles.* Langmuir, 2013. **29**(48): p. 14962-14970.
77. Ho, C.C., et al., *Preparation of monodisperse ellipsoidal polystyrene particles.* Colloid Polym. Sci., 1993. **271**(5): p. 469-479.
78. Keville, K.M., E.I. Franses, and J.M. Caruthers, *Preparation and characterization of monodisperse polymer microspheroids.* J. Colloid Interface Sci., 1991. **144**(1): p. 103-126.
79. Park, B.J. and E.M. Furst, *Micromechanics of colloidal aggregates at the oil-water interface.* Soft Matter, 2011. **7**(17): p. 7683-7688.
80. Pantina, J.P. and E.M. Furst, *Elasticity and critical bending moment of model colloidal aggregates.* Phys. Rev. Lett., 2005. **94**(13): p. 138301.
81. Isa, L., et al., *Adsorption of core-shell nanoparticles at liquid-liquid interfaces.* Soft Matter, 2011. **7**(17): p. 7663-7675.
82. Lin, Y., et al., *Ultrathin cross-linked nanoparticle membranes.* Journal of the American Chemical Society, 2003. **125**(42): p. 12690-12691.
83. Lin, Y., et al., *Nanoparticle assembly and transport at liquid-liquid interfaces.* Science, 2003. **299**(5604): p. 226-229.
84. Cheung, D.L. and S.A.F. Bon, *Stability of Janus nanoparticles at fluid interfaces.* Soft Matter, 2009. **5**(20): p. 3969-3976.
85. Luu, X.C., J. Yu, and A. Striolo, *Ellipsoidal Janus Nanoparticles Adsorbed at the Water-Oil Interface: Some Evidence of Emergent Behavior.* Journal of Physical Chemistry B, 2013. **117**(44): p. 13922-13929.
86. Razavi, S., J. Koplik, and I. Kretzschmar, *The effect of capillary bridging on the Janus particle stability at the interface of two immiscible liquids.* Soft Matter, 2013. **9**(18): p. 4585-4589.
87. Fan, H., D.E. Resasco, and A. Striolo, *Amphiphilic Silica Nanoparticles at the Decane-Water Interface: Insights from Atomistic Simulations.* Langmuir, 2011. **27**(9): p. 5264-5274.
88. Drazer, G., et al., *Adsorption phenomena in the transport of a colloidal particle through a nanochannel containing a partially wetting fluid.* Physical Review Letters, 2002. **89**(24): p. 244501.
89. Allen, M. and D. Tildesley, *Computer simulation of liquids*. 1987, New York: Oxford University Press.
90. Frenkel, D. and B. Smit, *Understanding Molecular Simulation: From Algorithms to Applications*. 2001: Academic Press. 664.
91. Drazer, G., et al., *Wetting and particle adsorption in nanoflows.* Phys. Fluids, 2005. **17**(1): p. 017102.
92. Einstein, A., *On the theory of the brownian movement.* Ann.Phys. (Leipzig), 1906. **19**: p. 371-381.

93. Meyer, M., M. Mareschal, and M. Hayoun, *Computer modeling of a liquid-liquid interface.* J. Chem. Phys., 1988. **89**(2): p. 1067-1073.
94. Lehle, H. and M. Oettel, *Stability and interactions of nanocolloids at fluid interfaces: effects of capillary waves and line tensions.* J. Phys. Condens. Matter, 2008. **20**(40): p. 404224.
95. Luo, M., Y. Song, and L.L. Dai, *Heterogeneous or competitive self-assembly of surfactants and nanoparticles at liquid-liquid interfaces.* Molecular Simulation, 2009. **35**(10-11): p. 773-784.
96. Haile, J.M., *Molecular Dynamics Simulation: Elementary Methods*. 1997, New York: Wiley.
97. Heyes, D.M., *Transport coefficients of Lennard-Jones fluids: A molecular dynamics and effective-hard-sphere treatment.* Phys. Rev. B: Condens. Matter, 1988. **37**(10): p. 5677-5696.
98. Drazer, G., et al., *Adsorption phenomena in the transport of a colloidal particle through a nanochannel containing a partially wetting fluid.* Phys. Rev. Lett., 2002. **89**(24): p. 244501.
99. Cieplak, M., J. Koplik, and J.R. Banavar, *Boundary conditions at a fluid-solid interface.* Phys. Rev. Lett., 2001. **86**(5): p. 803-806.
100. Pieranski, P., *Two-dimensional interfacial colloidal crystals.* Phys. Rev. Lett., 1980. **45**: p. 569-572.
101. Cheung, D.L., *Molecular simulation of nanoparticle diffusion at fluid interfaces.* Chem. Phys. Lett., 2010. **495**(1-3): p. 55-59.
102. Peskir, G., *On the diffusion coefficient: The Einstein relation and beyond.* Stochastic Models, 2003. **19**(3): p. 383-405.
103. Nagayama, G. and P. Cheng, *Effects of interface wettability on microscale flow by molecular dynamics simulation.* Int. J. Heat Mass Transfer, 2004. **47**(3): p. 501-513.
104. Bloor, D. and e. Wyn-Jones, *The structure, dynamics, and equilibrium properties of colloidal systems*. 1990, Novato, CA, U.S.A: Kluwer Academic Publishers.
105. Grzelczak, M., et al., *Directed Self-Assembly of Nanoparticles.* Acs Nano, 2010. **4**(7): p. 3591-3605.
106. Galliero, G., *Lennard-Jones fluid-fluid interfaces under shear.* Physical Review E, 2010. **81**(5).
107. Padilla, P., S. Toxvaerd, and J. Stecki, *Shear flow at liquid–liquid interfaces.* Journal of Chemical Physics, 1995. **103**(2): p. 716-724.
108. Li, Y., J. Xu, and D. Li, *Molecular dynamics simulation of nanoscale liquid flows.* Microfluidics and Nanofluidics, 2010. **9**(6): p. 1011-1031.
109. Cheung, D.L., *Molecular dynamics study of nanoparticle stability at liquid interfaces: Effect of nanoparticle-solvent interaction and capillary waves.* Journal of Chemical Physics, 2011. **135**(5).
110. Priezjev, N.V., *Rate-dependent slip boundary conditions for simple fluids.* Physical Review E, 2007. **75**(5).
111. Shinto, H., *Computer simulation of Wetting, capillary forces, and particle-stabilized emulsions: From molecular-scale to mesoscale modeling.* Advanced Powder Technology, 2012. **23**(5): p. 538-547.

112. Shinto, H., D. Komiyama, and K. Higashitani, *Lateral capillary forces between solid bodies on liquid surface: A lattice Boltzmann study.* Langmuir, 2006. **22**(5): p. 2058-2064.
113. Shinto, H., D. Komiyama, and K. Higashitani, *Lattice Boltzmann study of capillary forces between cylindrical particles.* Advanced Powder Technology, 2007. **18**(6): p. 643-662.
114. Frijters, S., F. Gunther, and J. Harting, *Effects of nanoparticles and surfactant on droplets in shear flow.* Soft Matter, 2012. **8**(24): p. 6542-6556.
115. Succi, S., *The lattice Boltzmann equation for fluid dynamics and beyond*. 2001, Oxford: Oxford University Press.
116. Chen, L., et al., *A critical review of the pseudopotential multiphase lattice Boltzmann model: Methods and applications.* International Journal of Heat and Mass Transfer, 2014. **76**: p. 210-236.
117. Jansen, H.P., et al., *Lattice Boltzmann modeling of directional wetting: Comparing simulations to experiments.* Physical Review E, 2013. **88**(1).
118. Lee, T. and L. Liu, *Lattice Boltzmann simulations of micron-scale drop impact on dry surfaces.* Journal of Computational Physics, 2010. **229**(20): p. 8045-8062.
119. Ladd, A.J.C., *Numerical simulations of particulate suspensions via a discretized Boltzmann equation. Part 1. Theoretical foundation.* Journal of Fluid Mechanics, 1994. **271**: p. 285-309.
120. Ladd, A.J.C., *Numerical simulations of particulate suspensions via a discretized Boltzmann equation. Part 2. Numerical results.* Journal of Fluid Mechanics, 1994. **271**: p. 311-339.
121. Ladd, A.J.C. and R. Verberg, *Lattice-Boltzmann simulations of particle-fluid suspensions.* Journal of Statistical Physics, 2001. **104**(5-6): p. 1191-1251.
122. Connington, K.W., T. Lee, and J.F. Morris, *Interaction of fluid interfaces with immersed solid particles using the lattice Boltzmann method for liquid-gas-particle systems.* Journal of Computational Physics, 2015. **283**: p. 453-477.
123. Li, Y., et al., *Hierarchical Nanostructures Self-Assembled from a Mixture System Containing Rod-Coil Block Copolymers and Rigid Homopolymers.* Scientific Reports, 2015. **5**.